Development of a Linearized Unsteady Euler Analysis for Turbomachinery Blade Rows

Joseph M. Verdon, Matthew D. Montgomery, and Kenneth A. Kousen
United Technologies Research Center
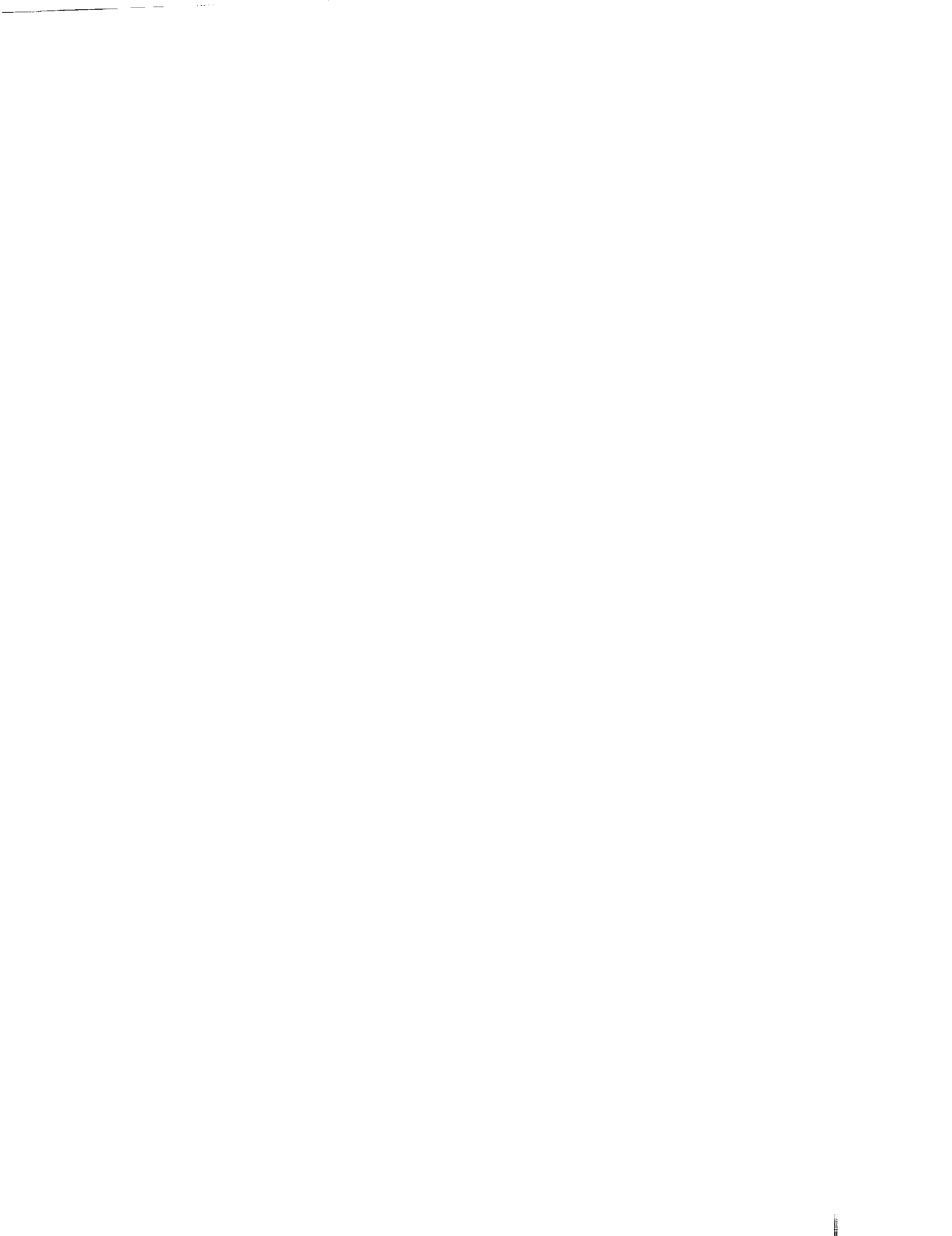*East Hartford, Connecticut*

National Aeronautics and
Space Administration

Office of Management

Scientific and Technical
Information Program

1995

Development of a Linearized Unsteady Euler Analysis
for Turbomachinery Blade Rows

Contents

Development of a Linearized Unsteady Euler Analysis for Turbomachinery Blade Rows

Summary

Progress toward the development of a linearized, unsteady, aerodynamic analysis for axial-flow turbomachinery blading is outlined in this report. The linearization is based on the Euler equations of fluid motion and is motivated by the need for an efficient aerodynamic analysis that can be used in predicting the aeroelastic and aeroacoustic responses of blade rows. The field equations and surface conditions required for nonlinear and linearized, inviscid, unsteady, aerodynamic analyses of three-dimensional flows through single, stationary or rotating, blade rows operating within cylindrical ducts are derived. Also, a description of the approximate far-field conditions that are currently available for completing these unsteady aerodynamic formulations is given.

An existing numerical algorithm for determining time-accurate solutions of the nonlinear unsteady flow problem is described, and a numerical model, derived from this nonlinear flow solver, is formulated for the first-harmonic, linear, unsteady problem. In previous work at NASA Lewis, two-dimensional versions of the nonlinear aerodynamic and numerical models have been implemented into a time-accurate, unsteady flow code, known as NPHASE. Under the present effort, the linearized aerodynamic and numerical models have been implemented into a corresponding first-harmonic, unsteady, flow code, called LINFLUX. At present the NPHASE and LINFLUX codes apply to two-dimensional flows, but extensions to three-dimensional flows are planned as future work.

The three-dimensional aerodynamic and numerical formulations and the two-dimensional LINFLUX analysis are described in this report. Numerical results for two-dimensional unsteady cascade flows, excited by prescribed blade motions and prescribed aerodynamic disturbances at inlet and exit, are also provided to illustrate the capabilities of the LINFLUX analysis. The present capabilities for predicting unsteady subsonic flows produced by blade vibrations and acoustic excitations are quite good, but additional work will be required so that accurate predictions of unsteady transonic flows and unsteady flows excited by entropic and vortical gusts can be determined. Additional work will also be required to improve the computational efficiency of the LINFLUX analysis.

1

1. Introduction

The development of theoretical analyses to predict unsteady flows in axial-flow turboma-
chines has been motivated primarily by the need to predict the aeroelastic (flutter and forced
vibration) and aeroacoustic (sound generation, transmission and reflection) behaviors of the
blading. For the most part, the blades of an isolated two-dimensional cascade have been
considered, viscous effects have been neglected and the unsteady fluctuations have been as-
sumed to be sufficiently small so that a linearized treatment of the unsteady flow is justified.
To determine the aeroelastic and aeroacoustic characteristics of the blading, the resulting
analyses must be useful for predicting the unsteady loads that act on the blades and the
unsteady pressure fields that exist upstream and downstream of the blade row and arise from
various sources of unsteady excitation. These sources include prescribed structural (blade)
motions and the external aerodynamic excitations associated with fluctuations in total tem-
perature and total pressure at inlet and fluctuations in static pressure at inlet and exit. In
particular, for blade flutter applications it is only necessary to predict the unsteady blade
loads that arise due to prescribed blade motions, whereas for forced vibration and aeroa-
coustic applications the unsteady blade loads and unsteady pressure fields, respectively, due
to incident entropic, vortical and acoustic disturbances are also required.

Until recently, the inviscid unsteady aerodynamic analyses that have been available for
turbomachinery aeroelastic and aeroacoustic design applications have been based on classical
linearized theory (see [Whi87] for an informative review). Here the steady and harmonic un-
steady departures of the flow variables from their uniform free-stream values are regarded as
small and of the same order of magnitude, leading to uncoupled, linear, constant-coefficient,
boundary-value problems for the steady and the complex amplitudes of the unsteady dis-
turbances. Thus, unsteady solutions based on the classical linearization apply essentially to
cascades of unloaded flat-plate blades that operate in an entirely subsonic or an entirely su-
personic environment. Very efficient semi-analytic solution procedures have been developed
for two-dimensional attached subsonic and supersonic flows and applied with some success
in turbomachinery aeroelastic and aeroacoustic design calculations. It should also be men-
tioned that extensive efforts (as reviewed by Namba [Nam87]) have been made to develop
three-dimensional unsteady aerodynamic analyses, based on the classical linearization.

Because of the limitations in physical modeling associated with the classical linearization,
more general two-dimensional inviscid linearizations have been developed. These include the
effects of important design features such as real blade geometry, mean blade loading, and
operation at transonic Mach numbers. Here, unsteady disturbances are regarded as small-
amplitude harmonic fluctuations relative to a fully nonuniform, potential, steady flow. The
steady flow is determined as a solution of a nonlinear inviscid equation set, and the unsteady
flow is governed by linear equations with variable coefficients that depend on the underlying
steady flow. This type of analytical model is often referred to as a linearized potential model,
although the potential flow restriction only applies to the steady background flow. It has
received considerable attention in recent years, and solution algorithms for the nonlinear
steady and the linearized unsteady problem have reached the stage where they are being
applied in turbomachinery aeroelastic and aeroacoustic design studies. We refer the reader to
the review articles by Verdon [Ver92, Ver93] for a description of the model and its application
to turbomachine cascades.

Linearized potential methods are based on the assumption of an isentropic and irrotational mean or steady background flow. Although these assumptions lead to significant computational efficiencies, they also limit the range of application of the resulting analyses. In particular, a more general linearization is required to predict three-dimensional unsteady flows in which the effects of mean swirl are important, and two- and three-dimensional flows in which strong shocks occur. For such flows, the nonlinear Euler equations are required to model the nonisentropic and rotational mean flow, and linearized versions of these equations are required to model the unsteady perturbation.

Recently, much attention had been given to the development of two-[HC93a, HC93b, KK93] and three-dimensional [HL92, HCL93] linearized Euler analyses. In these analyses, as in the earlier linearizations relative to potential mean flows, the linear unsteady equations are developed in the frequency domain and analytic far-field solutions are matched to numerical near-field solutions to limit the computational domain to a single blade-passage region of finite extent in the axial direction. Unlike the classical and potential-based linearizations, the linearized Euler equations are solved on a grid that deforms with the blade motion so that troublesome extrapolation terms in the blade surface conditions can be replaced by more tractable source terms in the field equations [HC93a]. Also, shock and wake effects are "captured" within a conservative finite-volume discretization, rather than "fitted" by imposing shock and wake jump conditions. Finally, because of the large number of unknowns in the discretized equation set, the first-harmonic linear equations are solved using pseudo-time as an iteration technique rather than by direct matrix inversion.

Under the present effort work has been initiated to develop a three-dimensional linearized unsteady aerodynamic analysis for turbomachinery blade rows that accounts for the effects of real blade geometry, mean blade loading, mean swirl and strong shocks. It is based on the Euler equations of fluid motion and the high-resolution, wave-split, implicit time marching, numerical scheme developed by Whitfield, Janus and Simpson [WJS88]. Here, the time-dependent Euler equations are written in strong conservation form in terms of curvilinear, computational coordinates and solved using an implicit time-marching procedure. A three-point, backward difference approximation, which is second-order accurate, is used to approximate time derivatives, and a cell-centered, upwind, finite-volume discretization is used to approximate spatial behavior. In the spatial discretization, fluxes at the cell interfaces are evaluated using a flux-splitting technique in which the eigenvalues of the flux Jacobian matrices control the direction of spatial differencing. The nonlinear discretized equations are solved at each instant of time using a Newton iteration procedure, that involves an approximate factorization of the residual equation. Gauss-Seidel sub-iterations are applied to reduce the approximate-factorization errors.

The wave or flux splitting used in [WJS88] allows flow discontinuities to be captured in one computational cell, if the grid is well aligned with the discontinuity. In addition, since the splitting scheme is based on a local eigenvalue decomposition of the Euler equations, the mean flow can be interrogated to determine the shock locations. A change in sign of the eigenvalues associated with acoustic waves indicates a change from supersonic to subsonic flow, and therefore the existence of a shock. This feature could facilitate shock fitting in the future via the imposition of shock jump conditions at mean shock locations.

Based upon the foregoing numerical scheme, Huff, Swafford and Reddy [HSR91] have constructed an implicit, multi-block, finite-volume analysis and computer code, called NPHASE,

3

for time-accurate resolutions of nonlinear, two-dimensional, unsteady flows through vibrating cascades. NPHASE is a robust analysis with a demonstrated capability to predict transonic flows with sharply defined shocks. It has also been modified by Sreenivas, Whitfield, and Huff [SWH93] to provide a linearized unsteady analysis in the time-domain. Under the present effort, a linearized, frequency-domain, unsteady aerodynamic model has been formulated, and a two-dimensional version of this model has been implemented into a computer code called LINFLUX. The LINFLUX code has been constructed by making the appropriate modifications to the NPHASE analysis.

In this report we will describe the nonlinear and linearized, three-dimensional, unsteady, aerodynamic and numerical formulations that form the foundation for the present effort. We will also present numerical results, based on the two-dimensional versions of these models that have been implemented into the LINFLUX code. In § 2 of this report the three-dimensional, unsteady, fluid-dynamic problem is described and various mathematical conventions, i.e., nomenclature, reference frames, independent variables, etc., are established. Starting from the integral conservation laws and the thermodynamic relations for a perfect gas, the field equations and surface conditions that govern nonlinear inviscid flow through a single rotating blade row operating within a cylindrical duct are presented in § 3. The small unsteady-disturbance approximation is introduced in § 4, leading to a nonlinear boundary value problem for a zeroth-order flow, that is steady in the rotor frame of reference, and a linear, variable-coefficient, boundary-value problem, in which the variable coefficients depend upon the steady background flow, for the first-order unsteady perturbation. The approximate far-field conditions available to complete the nonlinear and linearized unsteady aerodynamic formulations are described in some detail in § 5. The lack of suitable far-field conditions for three-dimensional flows is probably the most important impediment to the development of useful three-dimensional, unsteady aerodynamic analyses. Numerical models, based on the work of [WJS88] and [HSR91], for solving the nonlinear and the linearized, frequency-domain, unsteady aerodynamic equations are described in § 6. The application of the LINFLUX code to two-dimensional, unsteady cascade flows excited by prescribed blade motions and prescribed aerodynamic disturbances at inlet and exit is presented in § 7.

The numerical results presented in § 7 pertain to two-dimensional unsteady flows through the so-called Tenth Standard Cascade Configuration [FS83, FV93]. In particular, we consider unsteady subsonic and transonic flows driven by prescribed bending and torsional blade vibrations and, for purposes of comparison, present results determined using the linearized Euler analysis LINFLUX, the time-accurate, nonlinear, Euler analysis NPHASE [HSR91], and the linearized potential analysis LINFLO [Ver92, Ver93]. We also consider unsteady subsonic flows excited by acoustic disturbances at inlet and exit and by entropic and vortical disturbances at inlet, and present results, determined using the LINFLUX and LINFLO codes. The unsteady aerodynamic predictions given in § 7 indicate that the present LINFLUX analysis provides accurate aerodynamic response predictions for unsteady subsonic flows driven by prescribed blade motions or by acoustic excitations at inlet and exit. However, improvements in shock modeling will be required to allow accurate resolutions of unsteady transonic flows, and improvements in the numerical representation of blade-surface boundary conditions will be needed to accurately resolve unsteady flows excited by entropic and vortical disturbances. The computational efficiencies of the LINFLUX unsteady transonic and gust response calculations must also be improved.

4

2. Unsteady Flow through a Rotating Blade Row

2.1 Physical Problem

We consider time-dependent adiabatic flow, with negligible body forces, of an inviscid, non-heat conducting, perfect gas through a single rotating blade row such as the one shown in Figure 1. In particular, we will be concerned with a blade row operating within a cylindrical duct of radius $r = r_D(\xi)$ and mounted on cylindrical hub of radius $r = r_H(\xi)$, where ξ measures axial distance and r measures distance radially outward from the ξ-axis. The blade row consists of N distinct blades which rotate about this axis at angular velocity Ω. In the absence of unsteady fluid dynamic forces, the blades are assumed to be identical in shape, identical in orientation and equally spaced around the rotor. The mean or steady state position of the nth blade, in the rotor frame of reference, is described by an equation of the form

$$F(r,\theta,\xi) = \theta + \frac{2\pi n}{N} + f(r,\xi) = 0 , \quad n = 0,1,2,\dots , N-1 , \tag{2.1}$$

where θ measures angular distance in the direction opposite to the direction of the rotation and n is a blade number index which decreases in the direction of rotation.

For aeroelastic and aeroacoustic applications we are interested in a restricted class of unsteady flows; i.e., those in which the unsteady fluctuations can be regarded as perturbations, not necessarily small, of a background flow, that is steady in the rotor frame of reference. Thus, we will consider primarily situations in which the blades rotate at constant angular velocity and in which the background flows far upstream (say $\xi < \xi_-$) and far downstream ($\xi > \xi_+$) from the rotor are at most a small perturbation from a steady, axisymmetric, swirling flow. This perturbation stems from the interaction between the fluid and the blading and is steady in the rotor frame of reference.

The time-dependent or unsteady fluctuations in the flow, as seen by an observer attached to the blade row, arise from one or more of the following sources: prescribed vibratory blade motions, and prescribed upstream total temperature, total pressure and static pressure disturbances and downstream static pressure disturbances, that carry energy toward the blade row. For the most part, we will restrict our consideration to temporally and circumferentially periodic, unsteady excitations that are of small-amplitude.

For example, we will consider prescribed blade motions of the form

$$\mathcal{R}(r,\theta + 2\pi n/N, \xi, t) = Re\{\mathbf{R}(r,\theta,\xi)\exp[i(\omega t + n\sigma)]\}, \quad \mathbf{x} \text{ on } B, \quad n = 0,1,2,\dots , N-1, \tag{2.2}$$

where the vector $\mathcal{R}$ is the displacement of a point on a moving blade surface relative to its mean position in the rotating frame; $\mathbf{R}$, ($|\mathbf{R}| \sim \mathcal{O}(\epsilon)$), is a complex displacement-amplitude vector; ω is the temporal frequency of the blade motion relative to an observer in the rotor frame; σ is the phase angle between the motions of adjacent blades; $Re\{\ \}$ denotes the real part of $\{\ \}$, and B denotes the zeroth ($n = 0$) or reference blade surface.

The unsteady flows in the far upstream and far downstream regions are in part, prescribed as a fluid dynamic excitation and, in part, depend upon the interaction between the fluid and the blading. Typically, an unsteady aerodynamic excitation is represented

5

as a linear combination of fundamental disturbances that are harmonic in time and in the circumferential direction. For example, a fundamental pressure excitation would be of the form

$$\tilde{p}_{I,\mp\infty}(\mathbf{x},t) = Re\{p_{I,\mp\infty}(r)\exp[i(\omega t + m\theta) + \chi_m \xi]\}, \quad \xi \lessgtr \xi_\mp \qquad (2.3)$$

Here $p_{I,\mp\infty}(\mathbf{x},t)$ is an incident pressure disturbance, i.e., a pressure disturbance that travels towards the blade row from far upstream ($\xi < \xi_-$) or far downstream ($\xi > \xi_+$), ω is the temporal frequency of the disturbance, and m is the number of complete disturbance cycles that occur over one revolution, i.e., in the interval $0 \le \theta < 2\pi$. The quantities ω and m are prescribed, and $p_{I,\mp\infty}(r)$ and χ_m are determined from the equations that describe the fluid motion in the far field. Note that the interblade phase angle, σ, of an incident disturbance is $2\pi m/N$.

For aeroelastic and aeroacoustic investigations, the applications of primary interest here, the goal is to predict the unsteady fluid dynamic loads that act on the blades and the unsteady pressure fluctuations that carry energy away from the blade row, respectively, for various prescriptions of the foregoing excitations.

Two-Dimensional Approximation

In the present study we will provide fluid dynamic and numerical formulations for solving the physical problem just described. In addition, these formulations will be implemented into a two-dimensional unsteady Euler code, with the development of a three-dimensional code planned as future work. The two-dimensional unsteady flow problem is derived by considering the flow in a thin cylindrical annulus having inner and outer radii, $r = r_0 - \Delta r_0$ and $r = r_0 + \Delta r_0$, respectively; assuming that the radial components of the blade displacement and the fluid velocity are negligible, i.e., $\mathcal{R} \cdot \mathbf{e}_r \approx 0$ and $\tilde{\mathbf{V}} \cdot \mathbf{e}_r \approx 0$; and setting $\mathbf{V}_W = \mathbf{\Omega} \times \mathbf{r}_0 = \Omega r_0 \mathbf{e}_\theta$, where $\mathbf{V}_W$ is the absolute velocity of the blade row in the circumferential direction, and is constant, if $\dot{\Omega} = 0$.

If we unwrap the cylindrical annulus, set $\eta = r\theta$, $\mathbf{e}_\eta = \mathbf{e}_\theta$, $\tilde{V}_\eta = \tilde{V}_\theta$, etc., and regard ξ and η as Cartesian coordinates in the axial and tangential directions, respectively, we are effectively considering the flow through a rectilinear, two-dimensional cascade consisting of an infinite number of equally-spaced blades (see Figure 2). The mean or steady-state positions of the blade chord lines coincide with the line segments $\eta = \xi \tan\Theta + nG, 0 \le \xi \le \cos\Theta, n = 0, \pm 1, \pm 2, \ldots$, where n is the blade number index, Θ is the cascade stagger angle, and $\mathbf{G} = G\mathbf{e}_\eta$ is the cascade gap vector which is directed along the η-axis with magnitude, G, equal to the blade spacing.

The vibratory blade motions, i.e.,

$$\mathcal{R}(\mathbf{x} + n\mathbf{G}, t) = Re\{\mathbf{R}(\mathbf{x})\exp[i(\omega t + n\sigma)]\}, \quad \mathbf{x} \in B, n = 0, \pm 1, \pm 2 \ldots \qquad (2.4)$$

are prescribed functions of position $\mathbf{x}$ and time t, and, for a two-dimensional flow, small unsteady disturbances far from the blade row can be represented as the sum of independent entropic, vortical and acoustic modes of fluid motion. The entropic, $\tilde{s}_{-\infty}(\mathbf{x},t)$, vortical, $\tilde{\zeta}_{-\infty}(\mathbf{x},t)$, and acoustic, $\tilde{p}_{I,\mp\infty}(\mathbf{x},t)$, excitations are prescribed functions of $\mathbf{x}$ and t, that satisfy the fluid dynamic field equations and describe disturbances that carry energy toward

6

the blade row. For example, the fundamental external aerodynamic excitations can be described by equations of the form

$$\tilde{s}_{-\infty}(\mathbf{x}, t) = \mathrm{Re}\{s_{-\infty} \exp[i(\boldsymbol{\kappa}_{-\infty} \cdot \mathbf{x} + \omega t)]\} \ , \qquad (2.5)$$

$$\tilde{\zeta}_{-\infty}(\mathbf{x}, t) = \mathrm{Re}\{\zeta_{-\infty} \exp[i(\boldsymbol{\kappa}_{-\infty} \cdot \mathbf{x} + \omega t)]\} \ , \qquad (2.6)$$

and

$$\tilde{p}_{I,\mp\infty}(\mathbf{x}, t) = \mathrm{Re}\{p_{I,\mp\infty} \exp[i(\boldsymbol{\kappa}_{\mp\infty} \cdot \mathbf{x} + \omega t)]\} \ . \quad \xi \lessgtr \xi_{\mp} \qquad (2.7)$$

Here $s_{-\infty}$, $\zeta_{-\infty}$ and $p_{I,\mp\infty}$ are the complex amplitudes of incident entropic, vortical and pressure fluctuations, respectively, and $\boldsymbol{\kappa}_{\mp\infty}$ are the wave number vectors for these disturbances. The interblade phase angle, σ, of an incident disturbance is given by $\boldsymbol{\kappa}_{\mp\infty} \cdot \mathbf{G}$. Also, the temporal frequency and wave number of an incident entropic or vortical disturbance are related by $\omega = -\boldsymbol{\kappa}_{-\infty} \cdot \mathbf{V}_{-\infty}$, where $\mathbf{V}_{-\infty}$ is the uniform relative inlet velocity, but a more complicated relationship exists between ω and $\boldsymbol{\kappa}_{\mp\infty}$ for an incident pressure disturbance [Ver89b].

2.2 Mathematical Conventions

In this report all physical variables are dimensionless. Lengths have been scaled with respect to a reference length L^*, time with respect to the ratio L^*/V^*, where V^* is a reference flow speed, velocity with respect to V^*, density with respect to a reference density ρ^*, pressure, with respect to $\rho^*(V^*)^2$, specific internal energy and enthalpy with respect to $(V^*)^2$. Here, the superscript $*$ refers to a dimensional reference value of a flow variable. The reference length is based upon blade chord, and the reference values of the fluid dynamic variables are based upon the far upstream mean-flow conditions. Also, in the present report, vector and tensor quantities are written in bold-face type.

In anticipation of the small unsteady-disturbance approximation, which will be introduced in §4, the symbol $\sim$ will be used below to denote a fully nonlinear time-dependent fluid property, and, with the exception of the density, upper and lower case Roman letters will be used to represent the various nonlinear flow variables and their small-disturbance counterparts, respectively. Thus, for example, $\tilde{P}$ and P will refer to the nonlinear time-dependent fluid pressure and the pressure in a background flow, that is steady in the rotating frame of reference, respectively, and $\tilde{p}$ and p will refer to the time-dependent, small-disturbance, unsteady pressure and its complex amplitude. The corresponding symbols for the fluid density are $\tilde{\rho}, \bar{\rho}, \tilde{\rho}$ and ρ, respectively. The subscripts $-\infty$ and $+\infty$ will be used to denote values of the flow variables far upstream and far downstream from the blade row.

In addition to these notations for the fluid dynamic variables, upper case script letters (e.g., $\mathcal{S}$) represent instantaneous surface (blade, wake and shock) locations, whereas corresponding upper case block (S) letters refer to steady-state surface positions. The vector, $\mathcal{R}(\mathbf{x}, t), \mathbf{x} \in S$ or $\mathcal{R}_S$, measures the displacement of a point on a moving surface relative to its mean or steady-state position.

Reference Frames

For the most part, we will be conducting our analyses in a coordinate frame that rotates with the blade row, i.e., at angular velocity Ω, but we will also have occasion to work in a

space-fixed or inertial reference frame. Thus, we introduce the temporal coordinate t, the rotating cylindrical spatial coordinates r, θ, ξ, and the space-fixed cylindrical coordinates r, θ^A, ξ, where $\theta^A = \theta - \Omega t$. The coordinates ξ and r measure distance along and normal, respectively, to the axis of rotation and the angular coordinates, θ and θ^A measure angular distances in the direction opposite to the direction of rotation. We will also use rotating (x_1, x_2, x_3) and space-fixed (x_1^A, x_2^A, x_3^A) Cartesian coordinates in which the x_1- or x_1^A-axis coincides with the axis of rotation, i.e., $\Omega = \Omega e_\xi = \Omega e_{x_1}$. The Cartesian (x_1, x_2, x_3) and cylindrical (r, θ, ξ) coordinates of a point are related by

$$x_1 = \xi \quad , \quad x_2 = r\sin\theta \quad \text{and} \quad x_3 = -r\cos\theta \tag{2.8}$$

or

$$\xi = x_1 \quad , \quad \theta = \tan^{-1}(-x_2/x_3) \quad \text{and} \quad r = \left[(x_2)^2 + (x_3)^2\right]^{1/2} \tag{2.9}$$

We will require equations that describe the fluid motion in both the space-fixed or inertial reference frame and the rotating reference frame. Gradient operations, e.g., $\nabla f, \nabla \cdot \mathbf{F}$ and $\nabla \times \mathbf{F}$, where f and $\mathbf{F}$ are arbitrary scalar and vector functions, respectively, are invariant under a transformation from one rotating reference frame to another, as is the total time derivative df/dt of a scalar quantity. Local time derivatives of scalar and vector quantities and total time-derivatives of vector quantities are not invariant under such a transformation, but are related by

$$\left.\frac{\partial f}{\partial t}\right|_{\mathbf{x}^A} = \left.\frac{\partial f}{\partial t}\right|_{\mathbf{x}} - (\Omega \times \mathbf{r} \cdot \nabla)f \ ,$$

$$\left.\frac{\partial \mathbf{F}}{\partial t}\right|_{\mathbf{x}^A} = \left.\frac{\partial \mathbf{F}}{\partial t}\right|_{\mathbf{x}} - (\Omega \times \mathbf{r} \cdot \nabla)\mathbf{F} + \Omega \times \mathbf{F} \ , \tag{2.10}$$

and

$$\left.\frac{d\mathbf{F}}{dt}\right|_A = \frac{d\mathbf{F}}{dt} + \Omega \times \mathbf{F}$$

Here, for example, $d\mathbf{F}/dt|_A$ and $d\mathbf{F}/dt$ are the time derivatives as seen by observers in the space-fixed or inertial and the rotating reference frames, respectively. If the position vectors, $\mathbf{x}^A = \mathbf{x} + \Omega \times \mathbf{r}t$ and $\mathbf{x}$ track the motion of the fluid particle, then $d\mathbf{F}/dt|_A$ and $d\mathbf{F}/dt$ are material or convective derivatives of $\mathbf{F}$. In this case, we will use the symbol D/Dt in place of d/dt to emphasize that the total time derivative is a material derivative.

The fluid velocities, accelerations and vorticities as seen by observers in the spaced-fixed and rotating frames are related by

$$\tilde{\mathbf{V}}^A = \left.\frac{D\mathbf{x}^A}{Dt}\right|_A = \left(\frac{D}{Dt} + \Omega\times\right)\mathbf{x} = \tilde{\mathbf{V}} + \Omega \times \mathbf{r} \ , \tag{2.11}$$

$$\tilde{\mathbf{A}}^A = \left.\frac{D\tilde{\mathbf{V}}^A}{Dt}\right|_A = \left(\frac{D}{Dt} + \Omega\times\right)(\tilde{\mathbf{V}} + \Omega \times \mathbf{r}) = \tilde{\mathbf{A}} + 2\Omega \times \tilde{\mathbf{V}} + \dot{\Omega} \times \mathbf{r} + \Omega \times (\Omega \times \mathbf{r}) \ , \tag{2.12}$$

and

$$\zeta^A = \nabla \times \tilde{\mathbf{V}}^A = \nabla \times (\tilde{\mathbf{V}} + \Omega \times \mathbf{r}) = \nabla \times \tilde{\mathbf{V}} + 2\Omega = \zeta + 2\Omega \ . \tag{2.13}$$

8

Here $\overset{\ast}{\mathbf{V}}{}^{A}$, $\overset{\ast}{\mathbf{A}}{}^{A}$ and $\overset{\ast}{\zeta}{}^{A}$ are the velocity, acceleration, and vorticity, respectively, as seen by an observer in the inertial frame; $\overset{\ast}{\mathbf{V}}$, $\overset{\ast}{\mathbf{A}}$ and $\overset{\ast}{\zeta}$ are the velocity, acceleration, and vorticity seen by an observer fixed in the rotating frame; $\overset{\cdot}{\Omega}$ is the angular acceleration of this rotating frame; and r is the radial position vector. Quantities measured with respect to the inertial frame will be referred to as absolute flow quantities; those measured in the rotating frame, as relative flow quantities. The terms $2\Omega \times \overset{\ast}{\mathbf{V}}$, $\Omega \times (\Omega \times \mathbf{r})$, and $\overset{\cdot}{\Omega} \times \mathbf{r}$ in equation (2.12) represent Coriolis, centripetal and Euler accelerations, respectively. Note that, if $\nabla \times \mathbf{V}_A = 0$, the flow is irrotational in the space-fixed system, but it is rotational with $\overset{\ast}{\zeta} = -2\Omega$ relative to an observer in the rotating frame.

Spatial Independent Variables

To describe flows in which the fluid domain varies with time; e.g., unsteady flows over vibrating solid bodies, it is useful to consider two sets of independent variables, say $(\mathbf{x}, t)$ and $(\bar{\mathbf{x}}, t)$, where the position vectors $\mathbf{x}$ and $\bar{\mathbf{x}}$ refer to locations within the rotating frame of reference. The vector $\mathbf{x}(\bar{\mathbf{x}}, t)$ refers to the instantaneous location of a moving field point, say $\mathcal{P}$, at time t, whereas $\bar{\mathbf{x}}$ refers to the reference position of $\mathcal{P}$. Thus, we can write

$$\mathbf{x} = \mathbf{x}(\bar{\mathbf{x}}, t) = \bar{\mathbf{x}} + \mathcal{R}(\bar{\mathbf{x}}, t) \, , \tag{2.14}$$

where $\mathcal{R}(\bar{\mathbf{x}}, t)$ is the displacement of the point $\mathcal{P}$ from its reference position.

This representation is motivated by the need to conveniently account for solid body motions in unsteady flows. In particular, the vectors $\mathbf{x}_{\mathcal{S}}(\bar{\mathbf{x}}_S, t)$ and $\bar{\mathbf{x}}_S$ denote position vectors to a point on a moving surface $\mathcal{S}$ and to the location of this point on the reference surface S, respectively, and $\mathcal{R}_{\mathcal{S}} = \mathbf{x}_{\mathcal{S}} - \bar{\mathbf{x}}_S$ is the displacement of a point on the moving surface $\mathcal{S}$ relative to its stationary or reference position on S. It is assumed that $\mathcal{R}(\bar{\mathbf{x}}, t)$, is continuous, single valued, and that (2.14) can be inverted to give the reference coordinates $\bar{\mathbf{x}}$, of a moving field point in terms of its current position, $\mathbf{x}$, and the time t; i.e., the functions $\bar{\mathbf{x}} = \bar{\mathbf{x}}(\mathbf{x}, t)$ are also continuous and single-valued.

The behavior of fluid properties may be followed along the path of the moving point, $\mathcal{P}$, or at fixed spatial locations. For example, the fluid density, $\bar{\rho}$, may be expressed as a function of $\bar{\mathbf{x}}$ and t, where $\bar{\mathbf{x}}$ is the reference location of $\mathcal{P}$, or as a function of $\mathbf{x}$ and t, where $\mathbf{x}$ is the position of $\mathcal{P}$ at time t. Associated with these two descriptions are two derivatives with respect to time; $\partial(\ )/\partial t|_{\bar{\mathbf{x}}}$, the derivative with respect to time keeping $\bar{\mathbf{x}}$ constant, and $\partial(\ )/\partial t|_{\mathbf{x}}$, the derivative with respect to time keeping $\mathbf{x}$ constant. The former is the rate of change in a quantity as observed when following the motion of a moving point; the latter, the rate of change as observed at a fixed point $\mathbf{x}$ in space. These derivatives are related by

$$\left. \frac{\partial(\ )}{\partial t} \right|_{\bar{\mathbf{x}}} = \left. \frac{\partial(\ )}{\partial t} \right|_{\mathbf{x}} + (\dot{\mathcal{R}} \cdot \nabla_{\mathbf{x}})(\ ) \tag{2.15}$$

9

3. The Nonlinear, Time-Dependent, Aerodynamic Equations

The description of the foregoing physical assumptions and mathematical conventions brings us to a convenient starting point for presenting the equations that govern the unsteady flow through the blade row. These are determined from the conservation laws for mass, momentum and energy, and the thermodynamic relations for a perfect gas. We will write the governing equations, first, in terms of dependent and independent variables measured with respect to an inertial reference frame, and then, in terms of variables measured with respect to a reference frame rotating with the blade row at angular velocity Ω.

3.1 Conservation Laws and Thermodynamic Relations

We consider an arbitrary moving control volume, $\mathcal{V}(t)$, which is bounded by a moving control surface $\mathcal{S}(\mathbf{x}^A, t) = 0$. The conservation laws for the fluid within $\mathcal{V}$ at time t can be written as

$$\frac{d}{dt} \int_{\mathcal{V}} \breve{\rho} d\mathcal{V} \Big|_A + \int_{\mathcal{S}} \breve{\rho} (\tilde{\mathbf{V}}^A - \dot{\mathcal{R}}^A) \cdot \mathbf{n} d\mathcal{S} = 0 \,, \tag{3.1}$$

$$\frac{d}{dt} \int_{\mathcal{V}} \breve{\rho} \tilde{\mathbf{V}}^A d\mathcal{V} \Big|_A + \int_{\mathcal{S}} \breve{\rho} [\tilde{\mathbf{V}}^A \otimes (\tilde{\mathbf{V}}^A - \dot{\mathcal{R}}^A)] \cdot \mathbf{n} d\mathcal{S} = -\int_{\mathcal{S}} \breve{P} \mathbf{n} \cdot d\mathcal{S} \,, \tag{3.2}$$

and

$$\frac{d}{dt} \int_{\mathcal{V}} \breve{\rho} \tilde{E}_T^A d\mathcal{V} \Big|_A + \int_{\mathcal{S}} \breve{\rho} \tilde{E}_T^A (\tilde{\mathbf{V}}^A - \dot{\mathcal{R}}^A) \cdot \mathbf{n} d\mathcal{S} = -\int_{\mathcal{S}} \breve{P} \tilde{\mathbf{V}}^A \cdot \mathbf{n} d\mathcal{S} \,. \tag{3.3}$$

Here $d/dt|_A$ is the time derivative taken relative to an observer fixed in the inertial reference frame, and $\breve{\rho}$, $\tilde{\mathbf{V}}^A$, $\breve{P}$ and $\tilde{E}_T^A = \tilde{E} + (\tilde{V}^A)^2/2$ are the fluid density, absolute velocity, pressure and absolute specific total internal energy, respectively; $\dot{\mathcal{R}}^A$ is the absolute velocity of a field point lying on the control surface $\mathcal{S}$; $\tilde{\mathbf{V}}^A - \dot{\mathcal{R}}^A$ is the fluid velocity relative to the moving control surface; $\mathbf{n}$ is the unit outward normal vector to the control surface; and $\otimes$ denotes the tensor or dyadic product of two vectors.

The first and second terms on the left-hand-sides of the integral mass (3.1), momentum (3.2) and energy (3.3) conservation laws represent the time rate of increase of a conserved quantity, (i.e., mass, momentum or total internal energy) within the control volume and the efflux of that quantity through the control surface, respectively. The surface integrals on the right-hand-sides of (3.2) and (3.3) represent the external force acting on the fluid within the control volume $\mathcal{V}$, and the rate at which this force does work on the fluid within $\mathcal{V}$, respectively. In the absence of viscosity, discontinuities in the flow variables can occur. The integral forms of the conservation laws are therefore required to describe the flow over the entire domain of interest. These forms provide corresponding differential equations in regions where the flow variables are continuously differentiable and "jump" conditions at surfaces across which the flow variables are discontinuous, i.e., at vortex-sheets, and at shocks.

Rotating Frame Variables

We can express the conservation laws in terms of variables that are measured in the rotating reference frame by making use of (2.10) and substituting the dependent variable

10

relations:

$$\check{\mathbf{V}}^A = \check{\mathbf{V}} + \boldsymbol{\Omega} \times \mathbf{r}$$

and

$$\tilde{E}_T^A = \tilde{E} + (\check{V}^A)^2/2 = \tilde{E}_T + \check{\mathbf{V}} \cdot \boldsymbol{\Omega} \times \mathbf{r} + (\boldsymbol{\Omega} \times \mathbf{r})^2/2 \qquad (3.4)$$

into equations (3.1) – (3.3). Here $\check{\mathbf{V}}$ is the relative fluid velocity and $\tilde{E}_T = \tilde{E} + \check{V}^2/2$ is the relative total specific internal energy. After carrying out the algebra we find that

$$\frac{d}{dt} \int_{\mathcal{V}} \check{\tilde{\rho}} d\mathcal{V} + \int_{\mathcal{S}} \check{\tilde{\rho}}(\check{\mathbf{V}} - \dot{\mathcal{R}}) \cdot \mathbf{n} d\mathcal{S} = 0 \; , \qquad (3.5)$$

$$\frac{d}{dt} \int_{\mathcal{V}} \check{\tilde{\rho}}\check{\mathbf{V}} d\mathcal{V} + \int_{\mathcal{S}} [\check{\tilde{\rho}}\check{\mathbf{V}} \otimes (\check{\mathbf{V}} - \dot{\mathcal{R}}) + \tilde{P}\mathbf{I}] \cdot \mathbf{n} d\mathcal{S} = -\boldsymbol{\Omega} \times \int_{\mathcal{V}} \check{\tilde{\rho}}\check{\mathbf{V}} d\mathcal{V} - \left(\frac{d}{dt} + \boldsymbol{\Omega} \times\right) \int_{\mathcal{V}} \check{\tilde{\rho}}(\boldsymbol{\Omega} \times \mathbf{r}) d\mathcal{V}$$

$$- \int_{\mathcal{S}} \check{\tilde{\rho}}[(\boldsymbol{\Omega} \times \mathbf{r}) \otimes (\mathbf{V} - \dot{\mathcal{R}})] \cdot \mathbf{n} d\mathcal{S},$$

and

$$(3.6)$$

$$\frac{d}{dt} \int_{\mathcal{V}} \check{\tilde{\rho}}\tilde{E}_T d\mathcal{V} + \int_{\mathcal{S}} \left[\check{\tilde{\rho}}\tilde{E}_T(\check{\mathbf{V}} - \dot{\mathcal{R}}) + \tilde{P}\check{\mathbf{V}}\right] \cdot \mathbf{n} d\mathcal{S} = -\frac{d}{dt} \int_{\mathcal{V}} \check{\tilde{\rho}}[\check{\mathbf{V}} \cdot \boldsymbol{\Omega} \times \mathbf{r} + (\boldsymbol{\Omega} \times \mathbf{r})^2/2] d\mathcal{V}$$

$$- \int_{\mathcal{S}} \{\check{\tilde{\rho}}[\check{\mathbf{V}} \cdot \boldsymbol{\Omega} \times \mathbf{r} + (\boldsymbol{\Omega} \times \mathbf{r})^2/2](\mathbf{V} - \dot{\mathcal{R}}) + \tilde{P}\boldsymbol{\Omega} \times \mathbf{r}\} \cdot \mathbf{n} d\mathcal{S},$$

$$(3.7)$$

where d/dt is the time derivative measured by an observer in the rotating frame and $\mathcal{R}$ is the relative velocity of a point on the moving control surface $\mathcal{S}(\mathbf{x}, t)$. Note that the left-hand-sides of (3.5) – (3.7) are identical in form to (3.1) – (3.3). The source terms on the right-hand-sides of (3.6) – (3.7) account for the rotation of the blade-row fixed reference frame.

The integral conservation laws can be written in various alternative forms. For example, we can interchange the order of time differentiation and volume integration for the volume integrals appearing in (3.5), (3.6) and (3.7) by employing a modified version of the Reynolds transport theorem (see [Ari62] p. 85 or ([Mou84] p. 51), i.e.,

$$\frac{d}{dt} \int_{\mathcal{V}} (\quad) d\mathcal{V} = \int_{\mathcal{V}} \left(\left.\frac{\partial(\quad)}{\partial t}\right|_{\mathbf{x}} + \boldsymbol{\nabla}_{\mathbf{x}} \cdot [\dot{\mathcal{R}} \otimes (\quad)]\right) d\mathcal{V} \; , \qquad (3.8)$$

where $\dot{\mathcal{R}} \otimes (\quad)$ reduces to $\dot{\mathcal{R}}(\quad)$ if the quantity within the parantheses is a scalar. We can also apply Green's theorem, i.e.,

$$\int_{\mathcal{S}} \mathbf{n} \cdot (\quad) d\mathcal{S} = \int_{\mathcal{V}} \boldsymbol{\nabla}_{\mathbf{x}} \cdot (\quad) d\mathcal{V} \qquad (3.9)$$

to convert surface integrals in (3.5)–(3.7) to volume integrals.

11

In addition to the conservation equations, some relations from classical thermodynamics are needed to complete the specification of the unsteady fluid dynamic problem and to enhance our understanding of unsteady flow processes. In particular, we require the equation of state for a thermally perfect gas,

$$\tilde{P} = \gamma^{-1}(\gamma - 1)\tilde{\rho}\tilde{T} , \qquad (3.10)$$

and the relation between the specific internal energy and the temperature for a calorically perfect gas,

$$\tilde{E} = \gamma^{-1}\tilde{T} = (\gamma - 1)^{-1}\tilde{P}/\tilde{\rho} . \qquad (3.11)$$

Here $\tilde{T}$ is the temperature and γ is the specific heat ratio (constant pressure to constant volume) of the fluid . It follows from (3.10) and (3.11) that the pressure can be expressed in terms of the dependent variables $\tilde{\rho}$, $\tilde{V}^A$ and $\tilde{E}_T^A$ or $\tilde{\rho}$, V and $\tilde{E}_T$ as follows:

$$\tilde{P} = (\gamma - 1)\tilde{\rho}[\tilde{E}_T^A - (\tilde{V}^A)^2/2] = (\gamma - 1)\tilde{\rho}(\tilde{E}_T - \tilde{V}^2/2) \qquad (3.12)$$

Equation (3.12) can be substituted into the conservation laws (3.1) through (3.3) or (3.5) through (3.7), to provide independent equations (two scalar and one vector) for the unknown variables $\tilde{\rho}$, $\tilde{V}^{(A)}$ and $\tilde{E}_T^{(A)}$ or $\tilde{\rho}$, $\tilde{V}$, and $\tilde{E}_T$.

The enthalpy, $\tilde{H}$, of a fluid particle is defined by

$$\tilde{H} = \tilde{E} + \tilde{P}/\tilde{\rho} , \qquad (3.13)$$

and it follows from (3.10), and (3.11)

$$\tilde{H} = \tilde{T} = \gamma^{-1}(\gamma - 1)\tilde{P}/\tilde{\rho} \qquad (3.14)$$

Although enthalpy and temperature are different fluid dynamic properties, the relationship $\tilde{H} = \tilde{T}$ applies here because of the scalings used to non-dimensionalize the various flow variables. The total and relative total specific enthalpies of the fluid are given by

$$\tilde{H}_T^A = \tilde{H} + (\tilde{V}^A)^2/2 = \tilde{E}_T^A + \tilde{P}/\tilde{\rho} \qquad (3.15)$$

and

$$\tilde{H}_T = \tilde{H} + \tilde{V}^2/2 = \tilde{E}_T + \tilde{P}/\tilde{\rho} = \tilde{H}_T^A - \tilde{V} \cdot \Omega \times r - (\Omega \times r)^2/2 . \qquad (3.16)$$

We will also find it useful to introduce the fundamental thermodynamic identities

$$\tilde{T}d\tilde{S} = d\tilde{E} + \tilde{P}d(\tilde{\rho}^{-1}) = d\tilde{H} - \tilde{\rho}^{-1}d\tilde{P}, \qquad (3.17)$$

where $\tilde{S}$ is the specific entropy of the fluid. It then follows from (3.10) through (3.17) that the entropy is related to the pressure and density by the differential expression

$$d\tilde{S} = \gamma^{-1}d\tilde{P}/\tilde{P} - d\tilde{\rho}/\tilde{\rho} . \qquad (3.18)$$

Equation (3.18) can be integrated to relate the change in entropy between any two equilibrium states to the corresponding changes in pressure and density; i.e.,

$$\tilde{P}\tilde{\rho}^{-\gamma}e^{-\gamma\tilde{S}} \approx (\tilde{P}\tilde{\rho}^{-\gamma}e^{-\gamma\tilde{S}})_{\text{Ref}} , \qquad (3.19)$$

where the subscript refers to a reference thermodynamic state.

3.2 Field Equations

Equations that describe inviscid fluid motion at the field points, $\mathbf{x} = \bar{\mathbf{x}} + \mathcal{R}(\bar{\mathbf{x}}, t)$, i.e., the Euler equations, are obtained from the integral conservation laws, e.g., (3.1) – (3.3), by applying the transport theorem (3.8) to interchange the order of time differentiation and volume integration and Green's theorem (3.9) to convert the surface integrals to volume integrals. After taking the limit of the volume integrals as $\mathcal{V}(t) \to 0$, we find that the conservation laws, expressed in terms of the dependent variables $\tilde{\rho}$, $\tilde{\mathbf{V}}$ and $\tilde{E}_T$ and the independent variables $\mathbf{x}$ and t, have the form

$$\left.\frac{\partial \tilde{\rho}}{\partial t}\right|_{\mathbf{x}} + \nabla_{\mathbf{x}} \cdot (\dot{\mathcal{R}}\tilde{\rho}) + \nabla_{\mathbf{x}} \cdot [(\tilde{\mathbf{V}} - \dot{\mathcal{R}})\tilde{\rho}] = 0 \ . \tag{3.20}$$

$$\left.\frac{\partial \tilde{\rho}\tilde{\mathbf{V}}}{\partial t}\right|_{\mathbf{x}} + \nabla_{\mathbf{x}} \cdot (\dot{\mathcal{R}} \otimes \tilde{\rho}\tilde{\mathbf{V}}) + \nabla_{\mathbf{x}} \cdot [(\tilde{\mathbf{V}} - \dot{\mathcal{R}}) \otimes \tilde{\rho}\tilde{\mathbf{V}} + \tilde{P}\mathbf{I}] = -\tilde{\rho}[2\mathbf{\Omega} \times \tilde{\mathbf{V}} + \dot{\mathbf{\Omega}} \times \mathbf{r} + \mathbf{\Omega} \times (\mathbf{\Omega} \times \mathbf{r})] \tag{3.21}$$

and

$$\left.\frac{\partial (\tilde{\rho}\tilde{E}_T)}{\partial t}\right|_{\mathbf{x}} + \nabla_{\mathbf{x}} \cdot (\dot{\mathcal{R}}\tilde{\rho}\tilde{E}_T) + \nabla_{\mathbf{x}} \cdot [(\tilde{\mathbf{V}} - \dot{\mathcal{R}})\tilde{\rho}\tilde{E}_T + \tilde{P}\tilde{\mathbf{V}}] = -\tilde{\rho}\left[\tilde{\mathbf{V}} \cdot (\dot{\mathbf{\Omega}} \times \mathbf{r}) - \mathbf{\Omega} \times \mathbf{r} \cdot \mathbf{\Omega} \times \tilde{\mathbf{V}}\right] \ . \tag{3.22}$$

The right-hand-sides of the momentum (3.21) and energy (3.22) equations have been simplified by making use of (3.20) and (3.20) and (3.21), respectively, and performing some algebra. The source term on the right-hand-side of the momentum equation (3.21) accounts for the Coriolis, Euler and centripetal accelerations experienced by a fluid particle. To provide a complete set of governing equations, the conservation laws must be supplemented by the thermodynamic relation (3.12) which relates the fluid pressure to the density, relative total specific internal energy and the relative flow speed.

Equations (3.20)–(3.22) apply at all points within the fluid domain at which the fluid motion is continuous and differentiable. The displacement field $\mathcal{R}[\mathbf{x}(\bar{\mathbf{x}}, t)]$ is regarded as a known quantity and is usually prescribed so that field points that lie on moving solid surfaces always remain on such surfaces. Note that the terms containing $\mathcal{R}$ can be eliminated from (3.20) – (3.22). However, at this point, we have chosen to retain these terms so that there is a direct correspondence between the differential and the integral [(3.5) – (3.7)] forms of the conservation equations. Also, equations (3.20) – (3.22) have been written in terms of the independent variables $\mathbf{x}$ and t. The conservation laws could also be written using $\bar{\mathbf{x}}$ and t as independent variables by introducing the spatial coordinate transformation $\mathbf{x} \to \bar{\mathbf{x}}$. We will adopt this strategy in deriving the linearized Euler equations in §4.

Conservative forms of the governing differential equations are usually preferred for numerical simulations so that shocks and wakes can be "captured", but the convective forms of these equations are also useful, particularly in establishing analytic far-field conditions. These follow from (3.20) – (3.22) after applying some straightforward algebra. The convective form of the mass balance equation is

$$\frac{D\tilde{\rho}}{Dt} + \tilde{\rho}\nabla_{\mathbf{x}} \cdot \tilde{\mathbf{V}} = 0 \ , \tag{3.23}$$

13

where $D/Dt = \partial/\partial t|_{\mathbf{x}} + \check{\mathbf{V}} \cdot \boldsymbol{\nabla}_{\mathbf{x}}$ is the material or convective derivative operator relative to an observer fixed in the rotating frame. The convective form of the momentum equation, i.e.,

$$\tilde{\rho}\frac{D\check{\mathbf{V}}}{Dt} + \boldsymbol{\nabla}_{\mathbf{x}}\check{P} = -\tilde{\rho}\left[2\boldsymbol{\Omega} \times \check{\mathbf{V}} + \dot{\boldsymbol{\Omega}} \times \mathbf{r} + \boldsymbol{\Omega} \times (\boldsymbol{\Omega} \times \mathbf{r})\right] , \qquad (3.24)$$

is obtained by combining (3.21) and (3.23), and the convective form of the energy equation, i.e.,

$$\tilde{\rho}\frac{D\tilde{E}}{Dt} = -\check{P}\boldsymbol{\nabla}_{\mathbf{x}} \cdot \check{\mathbf{V}} , \qquad (3.25)$$

is obtained by combining (3.22), (3.23) and (3.24) and performing the necessary algebra.

Alternative convective forms of the energy equation can be determined by combining the thermal energy equation (3.25) with (3.23), (3.24) and the thermodynamic relations (3.17). We find that

$$\tilde{\rho}\frac{D\tilde{E}}{Dt} + \check{P}\boldsymbol{\nabla}_{\mathbf{x}} \cdot \check{\mathbf{V}} = \tilde{\rho}\check{T}\frac{D\check{S}}{Dt} = \tilde{\rho}\frac{D\check{H}}{Dt} - \frac{D\check{P}}{Dt} = 0 . \qquad (3.26)$$

In particular, the entropy of each fluid particle must remain constant in continuous regions of the inviscid flow. It also follows from equation (3.19) that, in such regions, the pressure and density of each fluid particle are related by the isentropic equation of state; i.e., $\check{P}\tilde{\rho}^{-\gamma} =$ constant.

Surface and Far-Field Conditions

For application to turbomachinery blade rows the foregoing field equations must be supplemented by boundary conditions at the moving blade surfaces and conditions on the flows at the inflow and outflow boundaries. Transient unsteady aerodynamic behavior is usually not of interest in turbomachinery aeroacoustic and aeroelastic calculations. Therefore, for such applications, a precise knowledge of the initial state of the fluid is not required.

For inviscid flows the flow tangency condition applies at the moving blade surfaces, i.e.,

$$(\check{\mathbf{V}} - \dot{\boldsymbol{\mathcal{R}}}) \cdot \mathbf{n} = 0 , \quad \mathbf{x} \in \mathcal{B}_n \quad (\text{or } \bar{\mathbf{x}} \in \mathrm{B}_n) , \qquad (3.27)$$

and at the stationary duct walls, i.e.,

$$\check{\mathbf{V}} \cdot \mathbf{n} = 0 , \quad \text{at } r = r_H \text{ and } r = r_D. \qquad (3.28)$$

The blade velocity $\dot{\boldsymbol{\mathcal{R}}}$ in (3.27) is a prescribed quantity [cf. (2.2) or (2.4)].

We also require conditions on the flow far upstream and far downstream from the blade row, i.e., at the inflow and outflow boundaries of the computational domain. Typically the circumferentially- and temporally-averaged values of the total pressure, total temperature and the inlet flow angle are specified as functions of radius at the inflow boundary. At the outflow boundary, the circumferentially- and temporally-averaged pressure is specified, consistent with radial equilibrium. In addition, total pressure and total temperature fluctuations at inlet, and the pressure fluctuations at inlet and exit, that carry energy towards the blade row, must be specified. Again, it should be noted that the unsteady excitations must be prescribed as solutions of the fluid-dynamic field equations. As discussed in §5, such prescriptions are only possible under restrictive assumptions about the flows far upstream

and far downstream of the blade row. Total pressure and total temperature fluctuations at exit and unsteady pressure disturbances at inlet and exit that carry energy away from the blade row must be determined as part of the unsteady solution. This is usually accomplished by extrapolating numerical "near-field" solutions through the inflow and outflow boundaries.

In principle, jump conditions should be imposed at vortex sheets ("viscous layers") and shocks, but the usual procedure in numerical calculations is to capture such discontinuities by solving the conservation forms of the field equations (3.20) – (3.22) over the entire fluid domain. However, for the sake of completeness, we will describe the jump conditions that apply at surfaces of discontinuity. These conditions are obtained from the integral conservation laws (3.1) – (3.3) or (3.5) – (3.7) by considering a control volume that contains a segment of such a surface, and taking limits, first, as the lateral extent of this volume normal to the surface segment approaches zero, and, then, as the area of the segment approaches zero. The resulting jump conditions for conserving mass, momentum and energy at a surface, $\mathcal{S}$, across which the flow variables are discontinuous are

$$[\![\tilde{M}_f]\!] = 0 \ , \tag{3.29}$$

$$\tilde{M}_f[\![\tilde{\mathbf{V}}^A]\!] + [\![\tilde{P}]\!]\mathbf{n} = \tilde{M}_f[\![\tilde{\mathbf{V}}]\!] + [\![\tilde{P}]\!]\mathbf{n} = 0 \tag{3.30}$$

and

$$\tilde{M}_f[\![\tilde{E}_T^A]\!] + [\![\tilde{P}\tilde{\mathbf{V}}^A]\!] \cdot \mathbf{n} = \tilde{M}_f[\![\tilde{E}_T]\!] + [\![\tilde{P}\tilde{\mathbf{V}}]\!] \cdot \mathbf{n} = 0 \ , \tag{3.31}$$

respectively. Here $[\![\ ]\!]$ denotes the jump in a flow quantity as experienced by an observer when moving across the surface of discontinuity $\mathcal{S}$ in the n-direction and

$$\tilde{M}_f = \tilde{\rho}(\tilde{\mathbf{V}}^A - \dot{\mathcal{R}}_S^A) \cdot \mathbf{n} = \tilde{\rho}(\tilde{\mathbf{V}} - \dot{\mathcal{R}}_S) \cdot \mathbf{n} \ , \quad \mathbf{x} \in \mathcal{S} \tag{3.32}$$

is the fluid mass flux through the surface.

Equations (3.29) – (3.31) have been derived by setting the field point velocity $\dot{\mathcal{R}}$ in the integral conservation laws equal to the surface velocity $\dot{\mathcal{R}}_S$. Thus, these equations are applied at points, $\mathbf{x} \in \mathcal{S}$ (or $\bar{\mathbf{x}} \in S$), that lie on a moving "boundary layer", wake or shock surface. In the present application the surface velocity vector $\dot{\mathcal{R}}_S$ is prescribed at blade surfaces, but at wake and shock surfaces it must be determined as part of the overall time-dependent, solution for the unsteady flow.

Since vortex sheets support a jump in tangential velocity, i.e., $[\![\tilde{\mathbf{V}}]\!] \cdot \boldsymbol{\tau} \neq 0$, it follows that the conditions

$$\tilde{M}_f = \tilde{\rho}(\tilde{\mathbf{V}} - \dot{\mathcal{R}}_S) \cdot \mathbf{n} = 0 \tag{3.33}$$

$$[\![\tilde{P}]\!] = 0 \tag{3.34}$$

and

$$[\![\tilde{\mathbf{V}}]\!] \cdot \mathbf{n} = 0 \ , \tag{3.35}$$

prevail at vortex sheet boundary-layer and wake surfaces. Since the vortex-sheet boundary layers coincide with the blade surfaces, (3.33) is equivalent to the inviscid flow tangency condition. At shocks, the mass flux is generally nonzero (i.e., $\tilde{M}_f \neq 0$). Hence, it follows from (3.30) that the tangential component of the fluid velocity $\tilde{\mathbf{V}} \cdot \boldsymbol{\tau}$, must be continuous across shocks. The remaining jump conditions, along with the thermodynamic equations of state, are then required to determine the shock velocity, $\dot{\mathcal{R}}_S$, and the changes in the normal component of the fluid velocity and the thermodynamic properties of the fluid as it passes through the shock.

15

3.3 Matrix Forms of the Governing Equations

The conservation equations are often written in matrix form. For example, we can write the integral conservation laws (3.5) – (3.7) and the corresponding differential expressions (3.20) – (3.22) as

$$\frac{d}{dt}\int_{\mathcal{V}}\tilde{\mathbf{U}}d\mathcal{V} + \int_{\mathcal{S}}[\tilde{\mathbf{F}}_j - \tilde{\mathbf{U}}\dot{\mathcal{R}}_{x_j}]n_{x_j}d\mathcal{S} = \int_{\mathcal{V}}\tilde{\mathbf{S}}d\mathcal{V} \qquad (3.36)$$

and

$$\left.\frac{\partial\tilde{\mathbf{U}}}{\partial t}\right|_{\mathbf{x}} + \frac{\partial}{\partial x_j}(\dot{\mathcal{R}}_{x_j}\tilde{\mathbf{U}}) + \frac{\partial}{\partial x_j}(\tilde{\mathbf{F}}_j - \tilde{\mathbf{U}}\dot{\mathcal{R}}_{x_j}) = \tilde{\mathbf{S}} , \qquad (3.37)$$

respectively. Here, the column vectors $\mathbf{U}, \mathbf{F}_j$, and $\mathbf{S}$ are referred to as state, extended flux. and source term vectors, respectively, $\dot{\mathcal{R}}_{x_j}, j = 1, 2, 3$ are the Cartesian components of the vector $\dot{\mathcal{R}}$, and a summation over repeated indices is implied.

The state vector, $\tilde{\mathbf{U}}$, the extended flux vector, $\tilde{\mathbf{F}}_j, j = 1, 2, 3$ and the source term vector, $\tilde{\mathbf{S}}$ are defined by

$$\tilde{\mathbf{U}} = \begin{bmatrix} \tilde{\rho} \\ \tilde{\rho}\tilde{V}_{x_1} \\ \tilde{\rho}\tilde{V}_{x_2} \\ \tilde{\rho}\tilde{V}_{x_3} \\ \tilde{\rho}\tilde{E}_T \end{bmatrix} , \qquad \tilde{\mathbf{F}}_j = \begin{bmatrix} \tilde{\rho}\tilde{V}_{x_j} \\ \tilde{\rho}\tilde{V}_{x_1}\tilde{V}_{x_j} + \tilde{P}\delta_{1j} \\ \tilde{\rho}\tilde{V}_{x_2}\tilde{V}_{x_j} + \tilde{P}\delta_{2j} \\ \tilde{\rho}\tilde{V}_{x_3}\tilde{V}_{x_j} + \tilde{P}\delta_{3j} \\ (\tilde{\rho}\tilde{E}_T + \tilde{P})\tilde{V}_{x_j} \end{bmatrix} ,$$

(3.38)

and

$$\tilde{\mathbf{S}} = \begin{bmatrix} 0 \\ 0 \\ \tilde{\rho}(2\Omega\tilde{V}_{x_3} + \dot{\Omega}x_3 + \Omega^2 x_2) \\ -\tilde{\rho}(2\Omega\tilde{V}_{x_2} + \dot{\Omega}x_2 - \Omega^2 x_3) \\ \tilde{\rho}[\dot{\Omega}(x_3\tilde{V}_{x_2} - x_2\tilde{V}_{x_3}) + \Omega^2(x_2\tilde{V}_{x_2} + x_3\tilde{V}_{x_3})] \end{bmatrix} .$$

The flux vectors $\tilde{\mathbf{F}}_j$ can also be expressed as explicit functions of the state variables $\tilde{U}_i$, $i = 1, 2 \ldots, 5$, and the source term vector $\tilde{\mathbf{S}}$ can be expressed as an explicit function of the

state variables and the spatial coordinates x_i, $i = 1, 2, 3$, i.e.,

$$\tilde{\mathbf{F}}_j(\tilde{\mathbf{U}}) = \begin{bmatrix} \tilde{U}_{j+1} \\ \tilde{U}_{j+1}\tilde{U}_2/\tilde{U}_1 + \tilde{P}\delta_{1j} \\ \tilde{U}_{j+1}\tilde{U}_3/\tilde{U}_1 + \tilde{P}\delta_{2j} \\ \tilde{U}_{j+1}\tilde{U}_4/\tilde{U}_1 + \tilde{P}\delta_{3j} \\ \tilde{U}_{j+1}(\tilde{U}_5 + \tilde{P})/\tilde{U}_1 \end{bmatrix} \quad \text{and} \quad \tilde{\mathbf{S}}(\tilde{\mathbf{U}}, \mathbf{x}) = \begin{bmatrix} 0 \\ 0 \\ \Omega^2\tilde{U}_1 x_2 + 2\Omega\tilde{U}_4 + \dot{\Omega}\tilde{U}_1 x_3 \\ \Omega^2\tilde{U}_1 x_3 - 2\Omega\tilde{U}_3 - \dot{\Omega}\tilde{U}_1 x_2 \\ \Omega^2(\tilde{U}_3 x_2 + \tilde{U}_4 x_3) + \dot{\Omega}(\tilde{U}_3 x_3 - \tilde{U}_4 x_2) \end{bmatrix}.$$

(3.39)

where

$$\tilde{P} = (\gamma - 1)[\tilde{U}_5 - \tilde{U}_1^{-1}(\tilde{U}_2^2 + \tilde{U}_3^2 + \tilde{U}_4^2)/2]$$ (3.40)

Our derivation of the field equations and surface conditions that govern the nonlinear, time-dependent, inviscid flow through a blade row operating within a cylindrical duct is now complete. The nonlinear, unsteady flow problem is formidable, and, to date, there has been relatively little attempt to apply time-accurate numerical simulations of unsteady flows in turbomachinery aeroelastic and aeroacoustic response studies, not only because of the associated mathematical complexities, but primarily because the computing resources needed for such simulations prohibits their use in detailed parametric investigations. Thus, in the next section we will make use of additional simplifying assumptions with the intention of providing a useful unsteady fluid dynamic model for turbomachinery aeroelastic and aeroacoustic design applications. In particular, we will restrict our consideration to small-amplitude, temporally and circumferentially periodic, unsteady excitations, and unsteady perturbations of a nonlinear background flow that is steady in the blade-row fixed, reference frame . In particular, the unsteady perturbations in the flow are assumed to be driven by prescribed blade motions of the form (2.2) and/or external aerodynamic excitations of the form (2.3).

4. The Small Unsteady-Disturbance Approximation

4.1 Mathematical Preliminaries

The computational resources required to simulate nonlinear inviscid and viscid unsteady fluid dynamic behavior will continue to prohibit the use of such simulations in repetitive aeroelastic or aeroacoustic design studies. Therefore, approximate analyses. based on the small-unsteady-disturbance assumption, are still needed to provide efficient predictions of unsteady aerodynamic response phenomena. Indeed, small-disturbance or linearized inviscid analyses have played and, for the forseeable future, will continue to play the central role in aeroelastic and aeroacoustic design calculations.

Thus, we consider inviscid unsteady flow through a three-dimensional blade row rotating at constant angular velocity, Ω, and seek approximations to the nonlinear, time-dependent, governing equations, which are valid for small-amplitude [i.e., of $\mathcal{O}(\epsilon) \ll 1$] unsteady excitations. If the excitations are of small amplitude, the unsteady part of the inviscid flow can be regarded as a linear perturbation of an underlying, nonlinear, zeroth-order, background flow. If the blades are identical in shape and orientation and equally spaced around the rotor, and the prescribed mean flow conditions at inlet and exit are axisymmetric, i.e., functions only of r and ξ, then the background flow will be steady in a reference frame that rotates with the blade row.

To determine approximate equations that describe the inviscid unsteady perturbation we must first expand the dependent flow variables in asymptotic series in ϵ. Thus, we consider dependent variable expansions of the form

$$\tilde{\mathbf{V}}[\mathbf{x}(\bar{\mathbf{x}},t),t] = \mathbf{V}(\bar{\mathbf{x}}) + \tilde{\mathbf{v}}[\mathbf{x}(\bar{\mathbf{x}},t),t] + \ldots = \mathbf{V}(\bar{\mathbf{x}}) + \tilde{\mathbf{v}}[\bar{\mathbf{x}}(\mathbf{x},t),t] + \ldots . \qquad (4.1)$$

Here $\tilde{\mathbf{V}}(\mathbf{x},t)$ is the nonlinear unsteady velocity at the instantaneous position $\mathbf{x}$ of a moving field point, $\mathbf{V}(\bar{\mathbf{x}}) \sim \mathcal{O}(1)$ is the zeroth-order or steady velocity at the reference position $\bar{\mathbf{x}}$, of this point, $\tilde{\mathbf{v}}[\bar{\mathbf{x}}(\mathbf{x},t),t] \sim \mathcal{O}(\epsilon)$ is first-order, unsteady, perturbation to the steady velocity at $\bar{\mathbf{x}}$ at the instantaneous location, $\mathbf{x}$, and the dots refer to higher order terms. We take the reference position $\bar{\mathbf{x}}$ of $\mathbf{x}$ to be the mean or steady-state position, and assume that $|\mathcal{R}| \sim \mathcal{O}(\epsilon)$. The asymptotic expansion (4.1) has been proposed only recently [HC93a] and [Gil93], and offers several advantages when used in conjunction with modern numerical solution procedures. According to this expansion $\partial \mathbf{V}/\partial t|_{\bar{\mathbf{x}}} = 0$ and therefore, it follows from (2.15) that $\partial \mathbf{V}/\partial t|_{\mathbf{x}} = -(\dot{\mathcal{R}} \cdot \nabla_{\bar{\mathbf{x}}})\mathbf{V}$.

If we set $\mathcal{R} \equiv 0$, then $\mathbf{x} = \bar{\mathbf{x}}$, and (4.1) becomes identical to the asymptotic expansion used in classical linearized analyses [Whi87] and in earlier linearizations relative to nonuniform, potential mean flows [Ver92, Ver93]. The latter leads to a set of linearized unsteady field equations, that apply at fixed points in space, and precludes the need to define a displacement field $\mathcal{R}(\bar{\mathbf{x}},t)$ over the entire solution domain. However, Taylor series expansions, e.g..

$$\tilde{P}_S = (\tilde{P} + \mathcal{R} \cdot \nabla \tilde{P} + \ldots)|_S \qquad (4.2)$$

are required to refer information at moving blade surfaces to the mean blade positions. As a result extrapolation terms of the form $(\mathcal{R} \cdot \nabla)\mathbf{V}$ and $(\mathcal{R} \cdot \nabla)P$ appear in the blade boundary conditions and in the expression used to evaluate the pressure at a moving blade

surface. These terms are difficult to evaluate accurately. Consequently, recent linearized solution methods [HC93a, HC93b, KK93, HL92] have employed the more general asymptotic expansion (4.1). With this expansion, if the displacement field $\mathcal{R}(\bar{\mathbf{x}}, t)$ satifies the condition $\mathcal{R}(\bar{\mathbf{x}}, t) = \mathcal{R}_{B_n}(\bar{\mathbf{x}}, t)$ for $\bar{\mathbf{x}} \in B_n$, extrapolation terms will not appear in the blade boundary conditions or surface pressure expressions. Instead, source terms, which are easier to evaluate accurately, will appear in the field equations for the linearized unsteady flow.

Up to this point we have expressed the fluid dynamic equations in terms of the independent variables $\mathbf{x}$ and t. However, the use of dependent variable expansions of the form (4.1) renders it more appropriate to express the steady and linearized unsteady equations in terms of the independent variables $\bar{\mathbf{x}}$ and t. The temporal derivatives $\partial(\quad)/\partial t|_{\mathbf{x}}$ and $\partial(\quad)/\partial t|_{\bar{\mathbf{x}}}$ transform according to (2.15); the gradient operators, according to

$$\nabla_{\mathbf{x}}(\quad) \approx \nabla_{\bar{\mathbf{x}}}(\quad) - (\nabla_{\bar{\mathbf{x}}} \otimes \mathcal{R}) \cdot \nabla_{\bar{\mathbf{x}}}(\quad) + \dots . \tag{4.3}$$

The equations that govern the zeroth-order steady and the first-order unsteady flows are obtained by substituting the series expansions for the dependent flow variables, e.g., (4.1) and the independent-variable relations (2.15) and (4.3) into the nonlinear, time-dependent, governing equations; equating terms of like power in ϵ; and neglecting terms of second and higher order in ϵ. After carrying out this procedure, we find that nonlinear and linear variable-coefficient equations are obtained, respectively, for the zeroth- and first-order flows. The variable coefficients that appear in the linearized unsteady problem depend upon the zeroth-order, steady background flow.

We will write the steady and linearized unsteady equations in terms of the rotating frame dependent variables, i.e., the relative velocity [cf. (4.1)] and the relative total specific internal energy

$$\tilde{E}_T(\mathbf{x}, t) = \tilde{E} + \tilde{V}^2/2 = E + V^2/2 + \tilde{e} + \mathbf{V} \cdot \tilde{\mathbf{v}} + \dots = E_T(\mathbf{x}) + \tilde{e}_T(\bar{\mathbf{x}}, t) + \dots . \tag{4.4}$$

It follows from (3.4) that the perturbation absolute velocity and specific total internal energy are given by

$$\tilde{\mathbf{v}}^A(\mathbf{x}, t) = \tilde{\mathbf{v}}(\mathbf{x}, t) + \Omega \times (\mathbf{r} - \bar{\mathbf{r}})$$

$$\tilde{e}_T^A = \tilde{e} + \mathbf{V}^A \cdot \tilde{\mathbf{v}}^A = \tilde{e}_T + \tilde{\mathbf{v}} \cdot \Omega \times \bar{\mathbf{r}} + \mathbf{V} \cdot \Omega \times (\mathbf{r} - \bar{\mathbf{r}}) , \tag{4.5}$$

where $\mathbf{r} = \mathbf{r}(\mathbf{x})$ and $\bar{\mathbf{r}} = \mathbf{r}(\bar{\mathbf{x}})$.

Consequences of the Small Unsteady Disturbance Approximation

A significant simplification offered by an unsteady aerodynamic linearization is that the fluid dynamic responses arising from various sources of unsteady excitation are not coupled, and hence, they can be determined separately. Indeed, it is usually sufficient in turbomachinery applications to develop solution procedures for a single harmonic (in space and time) component of a given unsteady excitation. Solutions for an arbitrary independent excitation and for arbitrary combinations of various independent excitations can then be obtained by superposition. It should be noted, however, that the linearization does limit the unsteady aerodynamic response phenomena that can be analyzed, since nonlinear inviscid unsteady

19

aerodynamic phenomena, such as phenomena associated with the appearance and disappearance of shocks or the effects of inlet flow distortion on blade flutter, cannot be taken into account.

Since the background flow is steady in the rotor fixed frame and the equations that govern the first-order unsteady flow properties are linear, the fluctuations in the unsteady flow properties caused by an unsteady excitation that is harmonic in time must have harmonic time dependence. We can take advantage of this feature by introducing a complex representation, for the first-order flow properties, e.g.,

$$\tilde{\mathbf{v}}(\bar{\mathbf{x}}, t) = Re[\mathbf{v}(\bar{\mathbf{x}}) \exp(i\omega t)] ,$$ (4.6)

where ω is the temporal frequency of the unsteady excitation in the blade-row fixed frame, and adopting the convention that the real parts of the various complex quantities represent the actual time-dependent physical quantities. The complex representation (4.6) can be used to remove explicit, physical, time dependence from the linearized unsteady problem; thereby, facilitating the determination of a solution.

As a consequence of our assumptions regarding rotor geometry and the mean inlet and exit flow conditions, the steady background flow will be periodic from blade-to-blade. Thus, for example, we can write

$$\mathbf{V}(\bar{r}, \bar{\theta} + 2\pi n/N, \bar{\xi}) = \mathbf{V}(\bar{r}, \bar{\theta}, \bar{\xi}) ,$$ (4.7)

where $\bar{r}$, $\bar{\theta}$, $\bar{\xi}$ are the cylindrical coordinates of the position vector $\bar{\mathbf{x}}$. If, in addition, the unsteady excitation is harmonic in time and in the circumferential or θ-direction, then the first-order unsteady flow will exhibit a phase-lagged, blade-to-blade periodicity, i.e.,

$$\mathbf{v}(\bar{r}, \bar{\theta} + 2\pi n/N, \bar{\xi}) = \mathbf{v}(\bar{r}, \bar{\theta}, \bar{\xi}) \exp(in\sigma) .$$ (4.8)

Here $\sigma = 2\pi m/N$ is the phase angle between the unsteady motions in adjacent blade passages, N is the number of distinct blades in the three-dimensional array and m is the number of disturbance cycles over one revolution, $0 \leq \theta \leq 2\pi$. Conditions (4.7) and (4.8) allow a numerical resolution of the steady and the linearized unsteady flows to be limited to a single extended blade-passage region and permit fluid properties at a point in the nth blade passage to be evaluated in terms of information available at the corresponding point in a reference $(n = 0)$ passage.

4.2 The Steady Background Flow

The field equations and surface conditions that govern the zeroth-order or steady background flow are obtained by substituting the expansions (4.1) into the appropriate time-dependent nonlinear equations and retaining only the zeroth-order terms. The zeroth-order flow serves as the background flow for the unsteady perturbation. Therefore, a solution to the zeroth-order problem is required to determine the variable coefficients that appear in the linearized unsteady problem.

The conservative forms of the differential mass, momentum and energy equations for the steady background flow are

$$\nabla_{\bar{\mathbf{x}}} \cdot (\bar{\rho}\mathbf{V}) = 0 ,$$ (4.9)

20

$$\nabla_{\bar{\mathbf{x}}} \cdot (\mathbf{V} \otimes \bar{\rho}\mathbf{V}) + \nabla_{\bar{\mathbf{x}}}P = -\bar{\rho}[2\boldsymbol{\Omega} \times \mathbf{V} + \boldsymbol{\Omega} \times (\boldsymbol{\Omega} \times \bar{\mathbf{r}})] \, , \tag{4.10}$$

and

$$\nabla_{\bar{\mathbf{x}}} \cdot (\mathbf{V}\bar{\rho}E_T + P\mathbf{V}) = \bar{\rho}\boldsymbol{\Omega} \times \bar{\mathbf{r}} \cdot \boldsymbol{\Omega} \times \mathbf{V} \, . \tag{4.11}$$

The convective forms of these equations are

$$\mathbf{V} \cdot \nabla_{\bar{\mathbf{x}}}\bar{\rho} + \bar{\rho}\nabla_{\bar{\mathbf{x}}} \cdot \mathbf{V} = 0 \, , \tag{4.12}$$

$$\bar{\rho}(\mathbf{V} \cdot \nabla_{\bar{\mathbf{x}}})\mathbf{V} + \nabla_{\bar{\mathbf{x}}}P = -\bar{\rho}[2\boldsymbol{\Omega} \times \mathbf{V} + \boldsymbol{\Omega} \times (\boldsymbol{\Omega} \times \bar{\mathbf{r}})] \, , \tag{4.13}$$

and

$$\mathbf{V} \cdot \nabla_{\bar{\mathbf{x}}}S = 0 \, . \tag{4.14}$$

Here $\bar{\rho}$, $\mathbf{V}$, P, E_T and S are the density, relative velocity, pressure, relative total specific internal energy, and entropy, respectively, in the steady background flow, $\bar{\mathbf{r}} = \mathbf{r}(\bar{\mathbf{x}})$, and the steady pressure can be determined in terms of the dependent variables $\bar{\rho}$ and E_T or $\bar{\rho}$ and S, by using (3.12) or (3.19) respectively.

Surface and Far-Field Conditions

In principle, surface conditions for the steady background flow follow from (3.29) through (3.35) and are imposed at the mean or steady-state positions of the blade, wake and shock surfaces. Mean blade positions are prescribed, but the mean wake and shock locations must be determined as part of the steady flow solution. However, the usual practice in nonlinear inviscid calculations is to capture shocks and wakes by solving the differential forms of the conservation laws throughout the fluid domain. Since we will follow this practice in the present study, shock and wake conditions will not be explicitly imposed.

By assumption, the steady background flow remains attached to the blades and the duct walls. Therefore, the conditions

$$\mathbf{V} \cdot \mathbf{n} = 0, \quad \text{for } \bar{\mathbf{x}} \in B_n, \quad r = r_H, \text{and } r = r_D \tag{4.15}$$

apply at the mean blade surfaces and at the inner and outer walls of the duct.

Conditions must also be imposed on the steady background flow far upstream and far downstream from the blade row. Steady-state non-reflecting inflow and outflow boundary conditions can be constructed [SG91] in which circumferentially averaged values of total temperature, total pressure and the flow angles are specified as functions of radius at the inflow boundary, and the circumferentially averaged value of the pressure is specified at the outflow boundary, consistent with radial equilibrium. Circumferential harmonics of the mean flow variables are not set to zero but are allowed to evolve to values that are consistent with the existence of an infinite annular duct upstream and downstream of the computational domain.

Finally, the periodic condition (4.7) can be imposed to restrict the steady flow solution domain to a single extended blade passage region, i.e., a region of angular pitch $\Delta\theta = 2\pi/N$. Since inlet and exit conditions are imposed at finite distances from the blade row, say at $\xi = \xi_-$ and $\xi = \xi_+$, respectively, the solution domain is a single extended blade passage region of finite axial extent.

21

4.3 The Linearized Unsteady Flow

The differential equations that govern the first-order or linearized inviscid unsteady flow are determined by substituting the asymptotic expansions for the flow variables (e.g., (4.1)) and the independent variable transformation ($\mathbf{x} \to \bar{\mathbf{x}}$) into the full time-dependent governing equations derived from the mass, momentum and energy conservation laws [i.e., (3.20), (3.21) and (3.22)], subtracting out the corresponding equations for the zeroth-order background flow, and neglecting terms of higher than first order in ϵ.

This procedure provides the following system of linearized Euler equations for the unsteady disturbance field:

$$\left.\frac{\partial \tilde{\rho}}{\partial t}\right|_{\bar{\mathbf{x}}} + \boldsymbol{\nabla}_{\bar{\mathbf{x}}} \cdot (\tilde{\rho}\mathbf{V} + \bar{\rho}\tilde{\mathbf{v}}) = \dot{\mathcal{R}} \cdot \boldsymbol{\nabla}_{\bar{\mathbf{x}}}\bar{\rho} + [(\boldsymbol{\nabla}_{\bar{\mathbf{x}}} \otimes \mathcal{R}) \cdot \boldsymbol{\nabla}_{\bar{\mathbf{x}}}] \cdot (\bar{\rho}\mathbf{V}) = 0 , \qquad (4.16)$$

$$\left.\frac{\partial}{\partial t}(\tilde{\rho}\mathbf{V} + \bar{\rho}\tilde{\mathbf{v}})\right|_{\bar{\mathbf{x}}} + \boldsymbol{\nabla}_{\bar{\mathbf{x}}} \cdot [\mathbf{V} \otimes (\tilde{\rho}\mathbf{V} + \bar{\rho}\tilde{\mathbf{v}}) + \tilde{\mathbf{v}} \otimes \bar{\rho}\mathbf{V} + \tilde{p}\tilde{\mathbf{I}}]$$

$$= \dot{\mathcal{R}} \cdot \boldsymbol{\nabla}_{\bar{\mathbf{x}}}(\bar{\rho}\tilde{\mathbf{V}}) + [(\boldsymbol{\nabla}_{\bar{\mathbf{x}}} \otimes \mathcal{R}) \cdot \boldsymbol{\nabla}_{\bar{\mathbf{x}}}] \cdot (\bar{\rho}\mathbf{V} \otimes \mathbf{V} + P\mathbf{I}) \qquad (4.17)$$

$$- \tilde{\rho}[2\boldsymbol{\Omega} \times \mathbf{V} + \boldsymbol{\Omega} \times (\boldsymbol{\Omega} \times \bar{\mathbf{r}})] - \bar{\rho}[2\boldsymbol{\Omega} \times \tilde{\mathbf{v}} + \boldsymbol{\Omega} \times (\boldsymbol{\Omega} \times \Delta\bar{\mathbf{r}})] ,$$

and

$$\left.\frac{\partial}{\partial t}(\tilde{\rho}E_T + \bar{\rho}\tilde{e}_T)\right|_{\bar{\mathbf{x}}} + \boldsymbol{\nabla}_{\bar{\mathbf{x}}} \cdot [\mathbf{V}(\tilde{\rho}E_T + \bar{\rho}\tilde{e}_T) + \tilde{\mathbf{v}}\bar{\rho}E_T + P\tilde{\mathbf{v}} + \tilde{p}\mathbf{V}]$$

$$= \dot{\mathcal{R}} \cdot \boldsymbol{\nabla}_{\bar{\mathbf{x}}}(\bar{\rho}E_T) + [(\boldsymbol{\nabla}_{\bar{\mathbf{x}}} \otimes \mathcal{R}) \cdot \boldsymbol{\nabla}_{\bar{\mathbf{x}}}] \cdot [(\bar{\rho}E_T + P)\mathbf{V}] \qquad (4.18)$$

$$+ \bar{\rho}[\boldsymbol{\Omega} \times \bar{\mathbf{r}} \cdot \boldsymbol{\Omega} \times \tilde{\mathbf{v}} + \boldsymbol{\Omega} \times \Delta\bar{\mathbf{r}} \cdot \boldsymbol{\Omega} \times \mathbf{V}] + \tilde{\rho}\boldsymbol{\Omega} \times \bar{\mathbf{r}} \cdot \boldsymbol{\Omega} \times \mathbf{V} .$$

Here $\tilde{\rho}$, $\tilde{\mathbf{v}}$, $\tilde{p}$ and $\tilde{e}_T$ are the time-dependent first-order density, relative velocity, pressure and relative total specific internal energy, respectively, and $\Delta\bar{\mathbf{r}} = \mathbf{r}[\mathbf{x}(\bar{\mathbf{x}}, t), t] - \mathbf{r}(\bar{\mathbf{x}})$. After expanding the equation of state (3.12), we find that the first-order pressure, density and total internal energy are related by

$$\tilde{p} = (\gamma - 1)[\bar{\rho}(\tilde{e}_T - \mathbf{V} \cdot \tilde{\mathbf{v}}) + \tilde{\rho}(E_T - V^2/2)] . \qquad (4.19)$$

The terms that depend on the blade motion, i.e., the terms containing $\mathcal{R}$, $\dot{\mathcal{R}}$ or $\boldsymbol{\Omega}$, are regarded as source terms and have therefore been placed on the right-hand-sides of equations (4.16) — (4.18).

Convective Forms of the Linearized Unsteady Equations

The convective forms of the first-order unsteady equations follow after applying the asymptotic expansions for the dependent flow variables and the independent variable transformation $\mathbf{x} \to \bar{\mathbf{x}}$ to equations (3.23), (3.24) and (3.26). We find that

$$\frac{\bar{D}\tilde{\rho}}{Dt} + \tilde{\mathbf{v}} \cdot \boldsymbol{\nabla}_{\bar{\mathbf{x}}}\bar{\rho} + \bar{\rho}\boldsymbol{\nabla}_{\bar{\mathbf{x}}} \cdot \tilde{\mathbf{v}} + \tilde{\rho}\boldsymbol{\nabla}_{\bar{\mathbf{x}}} \cdot \mathbf{V} = \dot{\mathcal{R}} \cdot \boldsymbol{\nabla}_{\bar{\mathbf{x}}}\bar{\rho} + [(\boldsymbol{\nabla}_{\bar{\mathbf{x}}} \otimes \mathcal{R}) \cdot \boldsymbol{\nabla}_{\bar{\mathbf{x}}}] \cdot (\bar{\rho}\mathbf{V}) , \qquad (4.20)$$

22

$$\bar{\rho}\left[\frac{\bar{D}\tilde{v}}{Dt} + (\tilde{v} \cdot \nabla_{\bar{x}})V\right] + \tilde{\rho}(V \cdot \nabla_{\bar{x}})V + \nabla_{\bar{x}}\tilde{p}$$

$$= \bar{\rho}(\dot{\mathcal{R}} \cdot \nabla_{\bar{x}})V + \bar{\rho}[V \cdot (\nabla_{\bar{x}} \otimes \mathcal{R}) \cdot \nabla_{\bar{x}}]V + (\nabla_{\bar{x}} \otimes \mathcal{R}) \cdot \nabla_{\bar{x}}P \qquad (4.21)$$

$$-\bar{\rho}[2\Omega \times \tilde{v} + \Omega \times (\Omega \times \Delta\bar{r})] - \tilde{\rho}[2\Omega \times V + \Omega \times (\Omega \times \bar{r})] \; ,$$

and

$$\frac{\bar{D}\tilde{s}}{Dt} + (\tilde{v} \cdot \nabla_{\bar{x}})S = \dot{\mathcal{R}} \cdot \nabla_{\bar{x}}S + [V \cdot (\nabla_{\bar{x}} \otimes \mathcal{R}) \cdot \nabla_{\bar{x}}]S \qquad (4.22)$$

where $\tilde{s}$ is the first-order entropy. In equations (4.20) – (4.22) $\bar{D}/Dt = \partial/\partial t|_{\bar{x}} + V \cdot \nabla_{\bar{x}}$ is a convective derivative operator based upon the mean-flow, relative velocity.

To complete the system of convection equations we require an additional equation relating the first-order density, pressure and entropy. This is obtained by expanding the thermodynamic relation (3.19), using (4.1), to obtain

$$\tilde{\rho} = \bar{\rho}[\gamma^{-1}\tilde{p}/P - \tilde{s}] = A^{-2}\tilde{p} - \bar{\rho}\tilde{s} = 0. \qquad (4.23)$$

Harmonic Unsteady Excitation

If we assume that the excitation driving the linearized unsteady flow is harmonic in time with temporal frequency ω, then we can express each unsteady flow variable as the real part of the product of a complex amplitude, which depends only on the spatial coordinates $\bar{x}$. and the exponential function $\exp(i\omega t)$, cf. (4.6). In this case the local, $\partial/\partial t|_{\bar{x}}$, and convective, $\bar{D}/Dt$, time derivatives of, say, the first-order unsteady pressure are given by

$$\left.\frac{\partial\tilde{p}}{\partial t}\right|_{\bar{x}} = Re\{i\omega p \exp(i\omega t)\} \qquad (4.24)$$

and

$$\frac{\bar{D}\tilde{p}}{Dt} = Re\{(i\omega + V \cdot \nabla_{\bar{x}})p \exp(i\omega t)\} = Re\left\{\frac{\bar{D}_\omega p}{Dt}\exp(i\omega t)\right\} \; , \qquad (4.25)$$

where $\bar{D}_\omega/Dt \equiv i\omega + V \cdot \nabla_{\bar{x}}$.

If we now replace the first-order unsteady flow properties in the linearized field equations by their complex representations, we arrive at time-independent, linear, partial differential equations for the complex amplitudes of the first harmonic unsteady flow variables. For example, the conservative forms of the first-order equations have the form

$$i\omega\rho + \nabla_{\bar{x}} \cdot (\rho V + \bar{\rho}v) = i\omega R \cdot \nabla_{\bar{x}}\bar{\rho} + [(\nabla_{\bar{x}} \otimes R) \cdot \nabla_{\bar{x}}] \cdot \bar{\rho}V \; , \qquad (4.26)$$

$$i\omega(\rho V + \bar{\rho}v) + \nabla_{\bar{x}} \cdot [V \otimes (\rho V + \bar{\rho}v) + v \otimes \bar{\rho}V + pI]$$

$$= i\omega R \cdot \nabla_{\bar{x}}(\bar{\rho}V) + [(\nabla_{\bar{x}} \otimes R) \cdot \nabla_{\bar{x}}](\bar{\rho}V \otimes V + PI) \qquad (4.27)$$

$$-\rho[2\Omega \times V + \Omega \times (\Omega \times \bar{r})] - \bar{\rho}[2\Omega \times v + \Omega \times (\Omega \times \Delta\bar{r})] \; ,$$

23

and

$$i\omega(\rho E_T + \bar{\rho}e_T) + \nabla_{\bar{x}} \cdot [\mathbf{V}(\rho E_T + \bar{\rho}e_T) + \mathbf{v}\bar{\rho}E_T] + \nabla_{\bar{x}} \cdot (P\mathbf{v} + p\mathbf{V})$$

$$= i\omega\mathbf{R} \cdot \nabla_{\bar{x}}(\bar{\rho}E_T) + [(\nabla_{\bar{x}} \otimes \mathbf{R}) \cdot \nabla_{\bar{x}}] \cdot (\bar{\rho}E_T + P)\mathbf{V} \qquad (4.28)$$

$$+\bar{\rho}[\Omega \times \dot{\mathbf{r}} \cdot \Omega \times \mathbf{v} + \Omega \times \Delta\bar{\mathbf{r}} \cdot \Omega \times \mathbf{V}] + \rho\Omega \times \bar{\mathbf{r}} \cdot \Omega \times \mathbf{V}$$

where

$$p = (\gamma - 1)[\bar{\rho}(e_T - \mathbf{V} \cdot \mathbf{v}) + \rho(E_T - V^2/2)] \ . \qquad (4.29)$$

Boundary Conditions

Conditions on the unsteady perturbation at the moving blade surfaces, $\mathbf{x} \in \mathcal{B}_n$ or $\bar{\mathbf{x}} \in B_n$, are obtained by substituting the asymptotic series expansion (4.1) and the relation between the unit normals at points $\mathbf{x} = \bar{\mathbf{x}} + \mathcal{R}(\bar{\mathbf{x}}, t)$ and $\bar{\mathbf{x}}$ on the instantaneous and reference surface positions, i.e.,

$$\mathbf{n}_{\mathcal{B}_n} = \mathbf{n}_{B_n} - \nabla_T \otimes \mathcal{R} \cdot \mathbf{n}_{B_n} + \cdots \ , \qquad (4.30)$$

into the full time-dependent surface conditions, subtracting out the corresponding zeroth-order conditions and neglecting terms of higher than first order in ϵ. In equation (4.30) ∇_T involves only derivatives along a reference blade surface, B_n. Thus, if τ and ν are orthogonal unit tangent vectors at a point on B_n, we can write

$$\nabla_T = \tau\frac{\partial}{\partial\tau} + \nu\frac{\partial}{\partial\nu} \qquad (4.31)$$

It follows from the nonlinear unsteady (3.27) and the zeroth-order, steady (4.15) flow tangency conditions, that the linearized unsteady flow tangency condition can be expressed as

$$\tilde{\mathbf{v}} \cdot \mathbf{n} = \left[\dot{\mathcal{R}} + \mathbf{V} \cdot \nabla_T \otimes \mathcal{R}\right] \cdot \mathbf{n} \ , \bar{\mathbf{x}} \in B_n \ . \qquad (4.32)$$

Condition (4.32) indicates that the normal component of the unsteady velocity at a reference blade depends upon the zeroth-order velocity, $\mathbf{V}$, and the prescribed blade displacement $\mathcal{R}$. We must also impose flow tangency conditions at the duct walls. Since these walls are assumed to be stationary, the appropriate conditions are

$$\tilde{\mathbf{v}} \cdot \mathbf{n} = 0, \quad \text{for } r = r_H \text{ and } r = r_D \qquad (4.33)$$

If the unsteady excitation is harmonic in time, then the linearized flow tangency conditions can be written as

$$\mathbf{v} \cdot \mathbf{n} = [i\omega\mathbf{R} + \mathbf{V} \cdot \nabla_T \otimes \mathbf{R}] \cdot \mathbf{n} \ , \quad \bar{\mathbf{x}} \text{ on } B_m \ , \qquad (4.34)$$

and

$$\mathbf{v} \cdot \mathbf{n} = 0, \quad r = r_H, r_D \qquad (4.35)$$

where $\mathbf{v}(\bar{\mathbf{x}})$ and $\mathbf{R}(\bar{\mathbf{x}})$, $\bar{\mathbf{x}} \in B$, are the complex amplitudes of the unsteady velocity fluctuation and the unsteady blade displacement, respectively.

In addition to the foregoing surface conditions, phase-lagged periodicity [cf. (4.10)] and far-field conditions must be imposed on the linearized unsteady flow. The latter conditions will be discussed in some detail in §5.

24

4.4 Matrix Forms of the Steady and Linearized Unsteady Equations

The nonlinear, time-independent Euler equations (3.20)–(3.22) have been written in matrix form in (3.37). For small-amplitude unsteady perturbations of a nonlinear mean or steady background flow, the state vector $\check{\mathbf{U}}$ in (3.37) can be approximated by the asymptotic series

$$\check{\mathbf{U}}[\mathbf{x}(\bar{\mathbf{x}},t)] = \mathbf{U}(\bar{\mathbf{x}}) + \check{\mathbf{u}}[\bar{\mathbf{x}}(\mathbf{x},t),t] + \ldots , \qquad (4.36)$$

where $\mathbf{U}(\bar{\mathbf{x}})$ is the vector of conservation variables for the steady background flow at $\bar{\mathbf{x}}$ and $\check{\mathbf{u}}[\bar{\mathbf{x}}(\mathbf{x},t),t]$ is the vector of conservation variables for the first-order unsteady flow at $\mathbf{x} = \bar{\mathbf{x}} + \mathcal{R}(\bar{\mathbf{x}},t)$. The flux $\check{\mathbf{F}}_j$ and source term, $\check{\mathbf{S}}$, vectors can be approximated using Taylor series expansions about the mean flow, $\mathbf{U}$, and the reference spatial location, $\bar{\mathbf{x}}$, i.e.,

$$\check{\mathbf{F}}_j(\check{\mathbf{U}}) \;=\; \mathbf{F}_j(\mathbf{U}) + \frac{\partial \mathbf{F}_j}{\partial \mathbf{U}}\check{\mathbf{u}} + \ldots$$

and

$$\check{\mathbf{S}}(\check{\mathbf{U}},\mathbf{x}) \;=\; \mathbf{S}(\mathbf{U},\bar{\mathbf{x}}) + \frac{\partial \mathbf{S}}{\partial \mathbf{U}}\check{\mathbf{u}} + (\mathcal{R}\cdot\nabla_{\bar{\mathbf{x}}})\mathbf{S} + \ldots \quad . \qquad (4.37)$$

The Jacobian matrices $\partial \mathbf{F}_j/\partial \mathbf{U} = \{\partial F_{ij}/\partial U_k\}$ and $\partial \mathbf{S}/\partial \mathbf{U} = \{\partial S_i/\partial U_k\}$, where the subscripts i and k refer to the ith row and kth column, respectively, depend only upon the mean flow solution, $\mathbf{U}$ and the reference spatial location $\bar{\mathbf{x}}$.

In terms of the physical variables

$$\check{\mathbf{u}} = \begin{bmatrix} \tilde{\rho} \\ \bar{\rho}\tilde{v}_{x_1} + \tilde{\rho}V_{x_1} \\ \bar{\rho}\tilde{v}_{x_2} + \tilde{\rho}V_{x_2} \\ \bar{\rho}\tilde{v}_{x_3} + \tilde{\rho}V_{x_3} \\ \bar{\rho}\tilde{e}_T + \tilde{\rho}E_T \end{bmatrix}, \quad \frac{\partial \mathbf{F}_j}{\partial \mathbf{U}}\check{\mathbf{u}} = \begin{bmatrix} \bar{\rho}\tilde{v}_{x_j} + \tilde{\rho}V_{x_j} \\ \bar{\rho}\tilde{v}_{x_1}V_{x_j} + \bar{\rho}V_{x_1}\tilde{v}_{x_j} + \tilde{\rho}V_{x_1}V_{x_j} + \tilde{p}\delta_{j1} \\ \bar{\rho}\tilde{v}_{x_2}V_{x_j} + \bar{\rho}V_{x_2}\tilde{v}_{x_j} + \tilde{\rho}V_{x_2}V_{x_j} + \tilde{p}\delta_{j2} \\ \bar{\rho}\tilde{v}_{x_3}V_{x_j} + \bar{\rho}V_{x_3}\tilde{v}_{x_j} + \tilde{\rho}V_{x_3}V_{x_j} + \tilde{p}\delta_{j3} \\ \bar{\rho}\tilde{h}_TV_{x_j} + \bar{\rho}H_T\tilde{v}_{x_j} + \tilde{\rho}H_TV_{x_j} , \end{bmatrix},$$

$$\frac{\partial \check{\mathbf{S}}}{\partial \mathbf{U}}\check{\mathbf{u}} = \begin{bmatrix} 0 \\ 0 \\ 2\Omega(\bar{\rho}\tilde{v}_{x_3} + \tilde{\rho}V_{x_3}) + \Omega^2\tilde{\rho}\bar{x}_2 \\ -2\Omega(\bar{\rho}\tilde{v}_{x_2} + \tilde{\rho}V_{x_2}) + \Omega^2\tilde{\rho}\bar{x}_3 \\ \Omega^2\bar{\rho}(\bar{x}_2\tilde{v}_{x_2} + \bar{x}_3\tilde{v}_{x_3}) \\ +\Omega^2\tilde{\rho}(\bar{x}_2V_{x_2} + \bar{x}_3V_{x_3}) \end{bmatrix}, \quad (\mathcal{R}\cdot\nabla_{\bar{\mathbf{x}}})\mathbf{S} = \begin{bmatrix} 0 \\ 0 \\ \bar{\rho}\Omega^2\mathcal{R}_{x_2} \\ \bar{\rho}\Omega^2\mathcal{R}_{x_3} \\ \bar{\rho}\Omega^2(V_{x_2}\mathcal{R}_{x_2} + V_{x_3}\mathcal{R}_{x_3}) \end{bmatrix} \qquad (4.38)$$

where $\tilde{p}$ is given by (4.19), H_T is the relative total specific enthalpy [cf. (3.16)] in the steady background flow and

$$\tilde{h}_T = \tilde{e}_T + \bar{\rho}^{-1}(P\tilde{\rho}/\bar{\rho} + \tilde{p}) \qquad (4.39)$$

25

is the first-order relative total specific enthalpy.

After substituting the expansions (4.36) and (4.37) and the transformation relations (2.15) and (4.3) into the nonlinear field equation (3.37), we find that the zeroth-order, steady background flow and the first-order unsteady perturbation are governed by the equations

$$\frac{\partial}{\partial \bar{x}_j} \mathbf{F}_j = \mathbf{S} \tag{4.40}$$

and

$$\left.\frac{\partial \tilde{\mathbf{u}}}{\partial t}\right|_{\bar{\mathbf{x}}} + \frac{\partial}{\partial \bar{x}_j}\left(\frac{\partial \mathbf{F}_j}{\partial \mathbf{U}}\tilde{\mathbf{u}}\right) = (\dot{\mathcal{R}} \cdot \boldsymbol{\nabla}_{\bar{\mathbf{x}}})\mathbf{U} + \left(\frac{\partial \mathcal{R}}{\partial \bar{x}_j} \cdot \boldsymbol{\nabla}_{\bar{\mathbf{x}}}\right)\mathbf{F}_j + \frac{\partial \mathbf{S}}{\partial \mathbf{U}}\tilde{\mathbf{u}} + (\mathcal{R} \cdot \boldsymbol{\nabla}_{\bar{\mathbf{x}}})\mathbf{S} , \tag{4.41}$$

respectively. If the excitation driving the linearized unsteady flow is harmonic in time with temporal frequency ω, we can set

$$\tilde{\mathbf{u}} = Re\{\mathbf{u}\exp(i\omega t)\} \quad \text{and} \quad \mathcal{R} = Re\{\mathbf{R}\exp(i\omega t)\} , \tag{4.42}$$

where the components of the state vector $\mathbf{u}$ are the complex amplitudes of the linearized unsteady conservation variables. In this case we can write the linearized unsteady equations in the form

$$i\omega\mathbf{u} + \frac{\partial}{\partial \bar{x}_j}\left(\frac{\partial \mathbf{F}_j}{\partial \mathbf{U}}\mathbf{u}\right) = i\omega(\mathbf{R} \cdot \boldsymbol{\nabla}_{\bar{\mathbf{x}}})\mathbf{U} + \left(\frac{\partial \mathbf{R}}{\partial \bar{x}_j} \cdot \boldsymbol{\nabla}_{\bar{\mathbf{x}}}\right)\mathbf{F}_j + \frac{\partial \mathbf{S}}{\partial \mathbf{U}}\mathbf{u} + (\mathbf{R} \cdot \boldsymbol{\nabla}_{\bar{\mathbf{x}}})\mathbf{S} , \tag{4.43}$$

The general solution procedure is first to solve for the nonlinear mean flow, and then, for the unsteady perturbation. The steady solution is used to form the Jacobian matrices $\partial \mathbf{F}_j/\partial \mathbf{U}$ and $\partial \mathbf{S}/\partial \mathbf{U}$ that appear in the linearized unsteady equation, (4.43).

Forms of the Equations Used in Numerical Calculations

For numerical calculations it is preferable to express the first harmonic unsteady equations in strong conservation form. This can be accomplished by multiplying the terms the steady equation (4.40) by $\boldsymbol{\nabla}_{\bar{\mathbf{x}}} \cdot \mathbf{R}$, adding the result to the right-hand-side of the linearized unsteady equation (4.43) and performing some algebra. This procedure results in a first harmonic unsteady equation of the form

$$i\omega\mathbf{u} \;+\; \frac{\partial}{\partial \bar{x}_j}\left(\frac{\partial \mathbf{F}_j}{\partial \mathbf{U}}\mathbf{u}\right) = -i\omega(\boldsymbol{\nabla}_{\bar{\mathbf{x}}} \cdot \mathbf{R})\mathbf{U} + i\omega\frac{\partial}{\partial \bar{x}_j}(\bar{R}_{x_j}\mathbf{U})$$

$$+ \; \frac{\partial}{\partial \bar{x}_j}\left[\frac{\partial R_{x_j}}{\partial \bar{x}_m}\mathbf{F}_m - (\boldsymbol{\nabla}_{\bar{\mathbf{x}}} \cdot \mathbf{R})\mathbf{F}_j\right] + \frac{\partial}{\partial \bar{x}_j}(R_{x_j}\mathbf{S}) + \frac{\partial \mathbf{S}}{\partial \mathbf{U}}\mathbf{u} \tag{4.44}$$

The first term on the right-hand-side of (4.44) is associated with temporal changes in the dependent variables within a moving control volume; the second, third and fourth terms, with fluxes across the control surface that bounds this volume; and the last term, with the changes in the source term, associated with the rotation of the reference frame, caused by the unsteady perturbation,.

26

For the numerical integration of equations (4.40) and (4.44), it is convenient to make the state vectors $\mathbf{U}$ and $\mathbf{u}$ pseudo-time dependent, as first suggested by Ni and Sisto [NS76]. Thus, we set

$$\tilde{\mathbf{U}}(\bar{\mathbf{x}}, t, \tau) = \mathbf{U}(\bar{\mathbf{x}}, \tau) + Re\{\mathbf{u}(\bar{\mathbf{x}}, \tau) \exp(i\omega t)\} , \qquad (4.45)$$

and write the steady and linearized unsteady equations in the form

$$\left.\frac{\partial \mathbf{U}}{\partial \tau}\right|_{\bar{\mathbf{x}}} + \frac{\partial \mathbf{F}_j}{\partial \bar{x}_j} = \mathbf{S} \qquad (4.46)$$

and

$$\left.\frac{\partial \mathbf{u}}{\partial \tau}\right|_{\bar{\mathbf{x}}} + i\omega \mathbf{u} + \frac{\partial}{\partial \bar{x}_j}\left(\frac{\partial \mathbf{F}_j}{\partial \mathbf{U}} \cdot \mathbf{u}\right) = -i\omega(\boldsymbol{\nabla}_{\bar{\mathbf{x}}} \cdot \mathbf{R})\mathbf{U} + i\omega\frac{\partial}{\partial \bar{x}_j}(\bar{R}_{x_j}\mathbf{U})$$

$$+ \frac{\partial}{\partial \bar{x}_j}\left[\frac{\partial R_{x_j}}{\partial x_m}\mathbf{F}_m - (\boldsymbol{\nabla}_{\bar{\mathbf{x}}} \cdot \mathbf{R})\mathbf{F}_j\right] + \frac{\partial}{\partial \bar{x}_j}(R_{x_j}\mathbf{S}) + \frac{\partial \mathbf{S}}{\partial \mathbf{U}}\mathbf{u} \qquad (4.47)$$

Now, both the nonlinear mean flow equation and the linearized Euler equation contain explicit pseudo-time derivative terms, that allow iterative solutions to be determined using conventional time-marching algorithms. The equations are marched forward in pseudo time until the steady and the complex amplitudes of the unsteady conservation variables reach steady state values. Because we are only interested in the steady state values of $\mathbf{U}$ and $\mathbf{u}$, there is no need to march the equations time accurately. Therefore, acceleration techniques such as multiple-grid and local time stepping can be applied to greatly reduce the computing time needed to solve an unsteady flow problem.

For finite volume calculations integral forms of (4.46) and (4.47) are required. These may be found by direct integration, and are given by

$$\frac{d}{d\tau}\int_{\mathcal{V}} \mathbf{U}d\mathcal{V} + \int_{\mathcal{S}} \mathbf{F}_j n_{x_j}d\mathcal{S} = \int_{\mathcal{V}} \mathbf{S}d\mathcal{V} , \qquad (4.48)$$

and

$$\left(\left.\frac{\partial}{\partial \tau}\right|_{\bar{\mathbf{x}}} + i\omega\right)\int_{\mathcal{V}} \mathbf{u}d\mathcal{V} + \int_{\mathcal{S}}\left(\frac{\partial \mathbf{F}_j}{\partial \mathbf{U}}\mathbf{u}\right)n_{x_j}d\mathcal{S} = -i\omega\int_{\mathcal{V}}(\boldsymbol{\nabla}_{\bar{\mathbf{x}}} \cdot \mathbf{R})\mathbf{U}d\mathcal{V}$$

$$+ \int_{\mathcal{S}}\left[i\omega R_{x_j}\mathbf{U} + \frac{\partial R_{x_j}}{\partial \bar{x}_m}\mathbf{F}_m - (\boldsymbol{\nabla}_{\bar{\mathbf{x}}} \cdot \mathbf{R})\mathbf{F}_j\right]n_{x_j}d\mathcal{S} + \int_{\mathcal{V}}\left[\frac{\partial}{\partial \bar{x}_j}(R_{x_j}\mathbf{S}) + \frac{\partial \mathbf{S}}{\partial \mathbf{U}}\mathbf{u}\right]d\mathcal{V} , \qquad (4.49)$$

where all terms on the right hand side of (4.49), except the last, depend only on the mean flow and displacement field, $\mathbf{R}(\bar{\mathbf{x}})$.

5. Far-Field Behavior

Conditions on the linearized unsteady flow at the computational inflow (at $\xi = \xi_-$) and outflow ($\xi = \xi_+$) boundaries are needed to allow the computational domain to be reduced to one of finite extent in the axial direction. Specifically, we must be able to prescribe incoming aerodynamic disturbances (excitations) as solutions of the governing equations, and the computational inflow and outflow boundaries must be transparent to all outgoing waves, so that spurious, nonphysical reflections are not generated. An approach, that has been applied successfully in two-dimensional unsteady flow calculations, is to determine analytic solutions for the unsteady flow variables far upstream and far downstream of a blade row, and to match these solutions to a numerical near-field solution [Ver89b]. Unfortunately, analytic solutions for three-dimensional unsteady disturbances are only available for the special case of a uniform, axial, steady background flow. Thus, at present, approximate far-field conditions must be applied in computational simulations of three-dimensional flows.

In this section, equations that describe the steady and linearized unsteady flows in the far field (i.e., for $\xi \lessgtr \xi_{\mp}$) of a blade row operating within a cylindrical duct will be examined. We will write these equations for a stationary ($\Omega = 0$) frame of reference, but as a convenience, we will omit the superscript A in describing absolute vector quantities and the subscript A in describing convective time derivatives [cf. (2.10) and (2.11)]. Thus, in this section, vector quantities, e.g., the fluid velocity, $\mathbf{V}$, and the time derivatives D/Dt and $\partial/\partial t|_x$ are measured relative to the stationary frame ($\Omega = 0$) and are, therefore, absolute flow quantities. In addition, we will consider fixed computational domains, i.e., $\mathcal{R} \equiv 0$, in the regions far upstream and far downstream of the blade row.

We assume that, in the far field, the mean or steady flow quantities are at most dependent only on radial position, the mean flow is isentropic, and that the radial component of the steady velocity is negligible, i.e.,

$$\mathbf{V} \approx V_\theta(r)\mathbf{e}_\theta + V_\xi(r)\mathbf{e}_\xi \ . \tag{5.1}$$

Under these conditions [cf. (4.13) and (3.18)]

$$\bar{\rho}^{-1}\frac{dP}{dr} = \gamma(\gamma-1)^{-1}\frac{d(\bar{\rho}^{-1}P)}{dr} = r^{-1}V_\theta^2 \ . \tag{5.2}$$

As a consequence of the foregoing mean-flow assumptions, the first-order equations of motion (4.22), (4.21), and (4.20) reduce to

$$\frac{\bar{D}\tilde{s}}{Dt} = 0 \ , \tag{5.3}$$

$$\frac{\bar{D}\tilde{\mathbf{v}}}{Dt} + \tilde{v}_r\frac{\partial}{\partial r}\mathbf{V} + (\tilde{s}V_\theta - \tilde{v}_\theta)r^{-1}V_\theta\mathbf{e}_r + \bar{\rho}^{-1}\nabla_x\tilde{p} - (\bar{\rho}rA^2)^{-1}V_\theta^2\tilde{p}\mathbf{e}_r = 0 \ , \tag{5.4}$$

and

$$\frac{\bar{D}\tilde{p}}{Dt} + \bar{\rho}A^2\nabla_x \cdot \tilde{\mathbf{v}} + r^{-1}\bar{\rho}V_\theta^2\tilde{v}_r = 0 \ . \tag{5.5}$$

We have made use of the first-order equation of state (4.23) and the mean-flow isentropic relation, $dP/d\bar{\rho} = A^2$ in deriving the momentum (5.4) and continuity (5.5) equations, and

28

$$\bar{D}/Dt = \partial/\partial t|_{\mathbf{x}} + r^{-1}V_\theta \partial/\partial\theta + V_\xi \partial/\partial\xi.$$ (5.6)

The linearized unsteady flow in the far-field can be determined by solving the system of convection equations (5.3), (5.4) and (5.5), for the first-order unsteady entropy ($\tilde{s}$), velocity ($\tilde{\mathbf{v}}$) and pressure ($\tilde{p}$). It follows from (5.3) that an entropic disturbance is convected by the mean flow, and it therefore has a general solution of the form

$$\tilde{s}(\mathbf{x},t) = \tilde{s}(r, r\theta - V_\theta t, \xi - V_\xi t)$$ (5.7)

If the mean flow is uniform, i.e., $\mathbf{V} = V_\xi \mathbf{e}_\xi$, the unsteady equations (5.3)–(5.5) have analytic solutions, which will be examined in detail in §5.1. These give some insight into three-dimensional unsteady flow behavior within a cylindrical duct. Analytical approaches for three-dimensional mean flows with axial shear and swirl will be discussed in §5.2. Another important situation in which analytic far-field solutions can be determined, is one in which the radial component of the unsteady velocity can be regarded as negligible [i.e., $\tilde{v}_r \sim \mathcal{O}(\epsilon^2)$]. This "two-dimensional", unsteady-flow approximation will be examined in §5.3. Finally, the techniques used for formulating and implementing numerical far-field boundary conditions will be discussed in §5.4.

5.1 Uniform Mean Flow in a Cylindrical Duct

First, we consider the unsteady perturbation of a uniform flow in a cylindrical duct, with velocity $\mathbf{V} = V_\xi \mathbf{e}_\xi$. In this case the unsteady equations (5.4) and (5.5) reduce to

$$\frac{\bar{D}\tilde{\mathbf{v}}}{Dt} + \bar{\rho}^{-1}\nabla_{\mathbf{x}}\tilde{p} = 0,$$ (5.8)

and

$$\frac{\bar{D}\tilde{p}}{Dt} + \bar{\rho}A^2\nabla_{\mathbf{x}}\cdot\tilde{\mathbf{v}} = 0,$$ (5.9)

where

$$\bar{D}/Dt = \partial/\partial t|_{\mathbf{x}} + V_\xi \partial/\partial\xi.$$ (5.10)

After taking the curl of each term in the momentum equation (5.8), we find that

$$\frac{\bar{D}\tilde{\zeta}}{Dt} = 0,$$ (5.11)

where $\tilde{\zeta} = \nabla \times \tilde{\mathbf{v}}$ is the unsteady vorticity. In addition, after applying the operators $-\bar{\rho}A^2\nabla\cdot(\ )$ and $\bar{D}(\ )/Dt$ to the terms in the momentum (5.8) and continuity equations (5.9), respectively, and combining the resulting equations, we find that

$$\frac{\bar{D}^2\tilde{p}}{Dt^2} - A^2\nabla_{\mathbf{x}}^2\tilde{p} = 0.$$ (5.12)

Equations (5.3), (5.11), and (5.12) indicate that first-order entropic, vortical and acoustic perturbations of a uniform mean flow are independent modes of unsteady motion. Entropic

29

and vortical disturbances are convected by the mean flow, and therefore have general solutions of the form

$$\tilde{s} = \tilde{s}(r, \theta, \xi - V_\xi t) \quad \text{and} \quad \tilde{\zeta} = \tilde{\zeta}(r, \theta, \xi - V_\xi t) \ . \tag{5.13}$$

Pressure disturbances are governed by a convected wave equation, and, as a consequence, such disturbances exhibit a more complicated behavior than entropic or vortical disturbances.

The unsteady perturbation can also be expressed in terms of independent entropic, rotational velocity, $\tilde{v}_R$, and irrotational velocity, $\nabla\tilde{\phi}$, disturbances. Following Goldstein [Gol76], we introduce the velocity splitting

$$\tilde{\mathbf{v}} = \tilde{\mathbf{v}}_R + \nabla_{\mathbf{x}}\tilde{\phi}, \tag{5.14}$$

where the rotational velocity is divergence free, i.e., $\nabla_{\mathbf{x}} \cdot \tilde{\mathbf{v}}_R \equiv 0$, and the velocity potential and pressure are related by

$$\tilde{p} = -\bar{\rho}\frac{\bar{D}\tilde{\phi}}{Dt} \ . \tag{5.15}$$

It follows from equations (5.8) and (5.9) that

$$\frac{D\tilde{\mathbf{v}}_R}{Dt} = 0 \quad \text{or} \quad \tilde{\mathbf{v}}_R = \tilde{\mathbf{v}}_R(r, \theta, \xi - V_\xi t) \ , \tag{5.16}$$

and

$$\frac{\bar{D}^2\tilde{\phi}}{Dt^2} + A^2\nabla_{\mathbf{x}}^2\tilde{\phi} = 0 \ . \tag{5.17}$$

Thus the rotational velocity, like the entropy and vorticity, is a convected quantity and the velocity potential, like the pressure, is governed by a convected wave equation. The solution to this equation can be used to determine the irrotational component, $\tilde{\mathbf{v}}_I = \nabla\tilde{\phi}$, of the unsteady velocity as well as the unsteady pressure.

For turbomachinery applications it is usually appropriate to restrict consideration to unsteady perturbations that are harmonic in time and periodic in the circumferential direction. Thus, e.g., we can write

$$\tilde{p}(\mathbf{x}, t) = Re\left\{p(\mathbf{x})\exp(i\omega t)\right\} = Re\left\{\left[\sum_{m=-\infty}^{\infty} p_m(r, \xi)\exp(im\theta)\right]\exp(i\omega t)\right\} \ , \tag{5.18}$$

where $p(\mathbf{x})$ is the complex amplitude and ω is the temporal frequency of the unsteady pressure fluctuation, and m is an integer equal to the number of complete cycles or "lobes" in the interval $0 \le \theta \le 2\pi$ of the mth component of the unsteady pressure disturbance. It follows that convected quantities, say entropy and rotational velocity, have complex amplitudes of the form

$$s(\mathbf{x}) = \left[\sum_{m=-\infty}^{\infty} s_m(r)\exp(im\theta)\right]\exp(i\kappa_\xi\xi) \tag{5.19}$$

and

$$\mathbf{v}_R(\mathbf{x}) = \left[\sum_{m=-\infty}^{\infty} \mathbf{v}_{R,m}(r)\exp(im\theta)\right]\exp(i\kappa_\xi\xi) \tag{5.20}$$

where $\kappa_\xi = -\omega V_\xi^{-1}$.

An analytic solution to the convected wave equation (5.12) for the unsteady pressure can be determined using the method of separation of variables [TS62, VTM82], leading to a solution for the functions $p_m(r, \xi)$ of the form

$$
\begin{aligned}
p_m(r, \xi) &= \sum_{n=0}^{\infty} a_{m,n} [J_m(k_{m,n}r) + Q_{m,n} Y_m(k_{m,n}r)] \exp(\chi_{m,n}\xi) \\
&= \sum_{n=0}^{\infty} a_{m,n} E_{m,n}(k_{m,n}r) \exp(\chi_{m,n}\xi) .
\end{aligned}
\tag{5.21}
$$

Here $a_{m,n}$, $Q_{m,n}$ and $k_{m,n}$ are constants, J_m and Y_m are Bessel functions of order m of the first and second kinds, respectively, $E(k_{m,n}r)$ is referred to as a "characteristic E-function", and

$$
\chi_{m,n} = \beta_{m,n} + i\kappa_{\xi,m,n} = (1 - M^2)^{-1} \left[iM\omega A^{-1} \mp \sqrt{(1 - M^2)k_{m,n}^2 - \omega^2 A^{-2}} \; \right] ,
\tag{5.22}
$$

where $M = V_\xi/A$ is the Mach number of the steady background flow. Note that $\chi_{m,n}$ is purely imaginary whenever $\omega/A > (1 - M^2)^{1/2}k_{m,n}$. Under this condition, the two-components of the m, nth pressure pattern propagate unattenuated along spiral paths normal to the lines $\kappa_{\xi,m,n}\xi + m\theta + \omega t = $ constant. If $\omega/A < (1 - M^2)k_{m,n}$, $\chi_{m,n}$ is complex and an m, nth acoustic disturbance grows or decays exponentially along the duct depending on whether the $-$ or $+$ sign is applicable. The appropriate sign, $-$ or $+$ in (5.22), is determined by the conditions imposed on the propagation of an acoustic wave. For example, an acoustic excitation must either attenuate as it approaches the blade row, or propagate carrying energy toward the blade row. Thus, for a subsonic mean flow ($M < 1$) the $-$ sign must be selected to describe an acoustic excitation from upstream; the $+$ sign, to describe an acoustic excitation from downstream.

The constants, $k_{m,n}$ and $Q_{m,n}$, in Equation (5.21) are determined by applying boundary conditions at the inner (hub), $r = r_H$, and outer (casing), $r = r_D$, walls of the duct. The so-called "hard wall" conditions,

$$
\frac{\partial p}{\partial r} = 0 \quad \text{at} \quad r = r_H \quad \text{and} \quad r = r_D ,
\tag{5.23}
$$

will be used here, but "soft-wall" boundary conditions, in which an acoustic impedance is specified along the walls, could also be applied. Conditions (5.23) lead to two simultaneous equations for determining the $k_{m,n}$ and $Q_{m,n}$, i.e.,

$$
J_m'(\mu k_{m,n}r_D) + Q_{m,n} Y_m'(\mu k_{m,n}r_D) = 0
\tag{5.24}
$$

and

$$
J_m'(k_{m,n}r_D) + Q_{m,n} Y_m'(k_{m,n}r_D) = 0 ,
\tag{5.25}
$$

where $\mu = r_H/r_D$ and the primes indicate differentiation with respect to r. This system has a nontrivial solution if and only if the determinant of the coefficients is equal to zero, i.e.,

$$
\begin{vmatrix}
J_m'(\mu k_{m,n}r_D) & Y_m'(\mu k_{m,n}r_D) \\
J_m'(k_{m,n}r_D) & Y_m'(k_{m,n}r_D)
\end{vmatrix} = 0 .
\tag{5.26}
$$

CHARACTERISTIC NUMBERS
Ordered by Magnitude

m	n	$k_{m,n}r_D$	m	n	$k_{m,n}r_D$	m	n	$k_{m,n}r_D$	m	n	$k_{m,n}r_D$
1	0	1.353429	1	2	12.702435	11	1	17.518803	19	0	21.182236
2	0	2.682314	11	0	12.826052	16	0	18.063198	7	3	21.382603
3	0	3.957204	2	2	12.951395	9	1	18.444412	8	3	22.127346
4	0	5.178097	3	2	13.342711	12	1	18.689379	15	0	22.135458
5	0	6.335176	8	1	13.802131	1	3	18.907080	20	0	22.219130
1	1	6.576327	12	0	13.878820	2	3	19.077499	12	2	22.223667
2	1	7.060908	4	2	13.896018	3	3	19.390278	9	2	22.999720
6	0	7.462803	5	2	14.542588	10	1	19.682482	16	1	23.256639
3	1	7.844923	13	0	14.927908	4	3	19.707966	13	2	23.469107
7	0	8.560980	9	0	15.067202	13	1	19.856277	10	2	23.845089
4	1	8.830198	6	2	15.395325	18	0	20.144039	17	0	24.381201
8	0	9.639520	14	0	15.975153	5	3	20.197456	14	2	24.771610
5	1	9.987278	7	2	16.277517	6	3	20.736031	11	3	24.823000
6	1	11.232715	10	0	16.305273	11	2	20.896011	1	4	25.190264
7	1	12.507607	8	2	17.336420	14	1	21.001701	2	4	25.360685

Table 5.1: Roots of the determinant equation (5.26) with $\mu = 0.5$ arranged in order of increasing magnitude (only the first 60 are shown).

The trancendental equation (5.26) has a countably infinite number of distinct roots $k_{m,n}r_D$ for each integer m, which can be placed in increasing order of magnitude and numbered $n = 0, 1, 2, \ldots$. The functions $E_{m,n}(k_{m,n}r)$ then have n zeros in the interval $r_H < r < r_D$.

A solution scheme for determining the roots of (5.26) is given in [VTM82]. It involves a combination of a fixed point iteration for each of the roots, along with a bisection algorithm for calculating roots that are either skipped by the iteration routine or occur in regions in which the iteration has difficulty in converging. Ordered results of this algorithm are shown in Table 5.1 for $\mu = 0.5$. Once the roots have been found and the constants $Q_{m,n}$ have been evaluated, the radial mode shapes or characteristic E-functions, can be determined. A few of these functions, normalized by their largest value, are shown in Figure 3.

As indicated by the foregoing results, a general acoustic perturbation of a uniform mean flow in a cylindrical duct consists of a combination of "spinning" modes, each containing m lobes and having a radial dependence described by linear combinations of mth order Bessel functions of the first and second kinds. These modes either decay as the move axially away from their source of origin, or propagate along spiral paths, unattenuated in amplitude.

5.2 Unsteady Perturbations of Nonuniform Mean Flows

If the underlying steady flow is not uniform, the equations of motion for three-dimensional unsteady disturbances do not reduce to a simple convection equation for the unsteady vor-

ticity nor to the standard convected wave equation for the unsteady pressure. The entropy is still a purely convected quantity with general solution given by (5.13); but vortical and acoustic disturbances are not independent modes of unsteady motion, and it is not possible to determine analytic solutions for these first-order unsteady flow variables. However, by assuming an exponential dependence for the temporal, circumferential, and axial behaviors of the unsteady perturbation quantities, the first order momentum and continuity equations can be reduced to a single, but complicated, second-order, ordinary differential equation for the radial behavior of the pressure. This equation along with the boundary conditions at the duct walls provides an eigenvalue problem for the unsteady perturbation, which must be solved numerically. A technique for determining this eigenvalue problem for a mean flow with axial shear and swirl is given below.

We consider a steady background flow containing both axial and swirling components of velocity, but no radial component. The steady velocity and thermodynamic properties are described by equations (5.1) and (5.2), respectively. If we assume that the first-order unsteady entropy, velocity and pressure consist of a superposition of fundamental disturbances that vary harmonically in time and in the circumferential direction and exponentially in the axial direction; e.g.,

$$\tilde{p}(r, \theta, \xi, t) = Re\{p(r) \exp[\chi(r)\xi + i(m\theta + \omega t)]\}, \tag{5.27}$$

and set

$$\lambda = i(\omega + mr^{-1}V_\theta) + \chi V_\xi, \tag{5.28}$$

the unsteady equations (5.3)–(5.5) reduce to

$$\lambda s = 0, \tag{5.29}$$

$$\lambda v_r - 2r^{-1}V_\theta v_\theta + r^{-1}V_\theta^2 s = -\bar{\rho}^{-1}\left(\frac{dp}{dr} + \frac{d\chi}{dr}\xi p\right) + (\bar{\rho}rA^2)^{-1}V_\theta^2 p, \tag{5.30}$$

$$\lambda v_\theta + \left(r^{-1}V_\theta + \frac{dV_\theta}{dr}\right)v_r = -im(\bar{\rho}r)^{-1}p, \tag{5.31}$$

$$\lambda v_\xi + \frac{dV_\xi}{dr}v_r = -\bar{\rho}^{-1}\chi p, \tag{5.32}$$

and

$$\lambda(\bar{\rho}A^2)^{-1}p + (rA^2)^{-1}V_\theta^2 v_r + \frac{dv_r}{dr} + r^{-1}v_r + \frac{d\chi}{dr}\xi v_r + imr^{-1}v_\theta + \chi v_\xi = 0. \tag{5.33}$$

The unsteady solutions will be composed of convected ($\lambda = 0$) and nonconvected ($\lambda \neq 0$) components. The entropy is a convected disturbance with axial wave number

$$\kappa_\xi = -i\chi = -(\omega + mr^{-1}V_\theta)V_\xi^{-1}, \tag{5.34}$$

which, in this case, varies with radial position. Other convected disturbances can be determined as solutions of the momentum and continuity equations. For example, the assumption

33

$\lambda = 0$ applied to the circumferential (5.31) and axial (5.32) momentum equations results in inconsistent equations for v_r and p unless the steady flow satisfies the condition

$$\left(r^{-1}V_\theta + \frac{dV_\theta}{dr}\right)\left(\omega + mr^{-1}V_\theta\right) = -mr^{-1}V_\xi\frac{dV_\xi}{dr}. \qquad (5.35)$$

If (5.35) is not satisfied, then $v_r = p = 0$, and the radial momentum (5.30) and continuity (5.33) equations have solutions of the form

$$v_\theta = \frac{V_\theta}{2}s \quad \text{and} \quad v_\xi = \frac{mV_\theta V_\xi s}{2(\omega + mr^{-1}V_\theta)}. \qquad (5.36)$$

If, in addition to $\lambda = 0$, there are no entropic perturbations, then $v_\theta = 0$. The axial disturbance velocity v_ξ will also be zero, implying no disturbances, unless $\omega + mr^{-1}V_\theta = 0$, whereupon v_ξ is arbitrary, and the axial wavenumber of this disturbance is zero. This condition can be satisfied if the swirl velocity is linearly dependent upon r, e.g., if $V_\theta = \Omega r$, where Ω is a constant angular velocity. This situation is designated as "solid-body swirl," and according to Kerrebrock [Ker70], reasonably represents the flow behind a high work blade row.

If there is no axial shear in the mean flow, i.e., $dV_\xi/dr = 0$, then the condition (5.35) is satisfied for the cases of solid-body swirl, if $\omega = -m\Omega$, and "free-vortex" swirl, which is described by $V_\theta = \Gamma/r$ and approximates the flow directly behind a fan rotor [Ker70]. Under either of these circumstances, the circumferential and axial momentum equations become simple multiples of each other, and either v_r or p can be specified independently.

Finally, if the circumferential component of the steady velocity is zero ($V_\theta = 0$) and $m \neq 0$, it follows from (5.31) and (5.32) that $v_r = 0$ and $p = 0$ and from (5.33) that

$$v_\xi = m(\omega r)^{-1}V_\xi v_\theta. \qquad (5.37)$$

This solution describes an unsteady velocity disturbance that carries no pressure and is convected at the mean flow velocity.

Nonconvected disturbances ($\lambda \neq 0$) are isentropic, i.e., $s = 0$. For such disturbances equations (5.30) – (5.32) can be solved simultaneously to give v_r, v_θ and v_ξ in terms of p and dp/dr, as long as

$$D = \lambda^2 + 2r^{-1}V_\theta\left(r^{-1}V_\theta + \frac{dV_\theta}{dr}\right) \neq 0, \qquad (5.38)$$

and the results can be subtituted into (5.33) to determine a second-order differential equation for $p(r)$. It can be shown that the condition $D = 0$ leads to the trivial solution in which all unsteady variables are zero. If $D \neq 0$ and we assume that χ is a constant, the unsteady velocities are given by

$$v_r = -\lambda(\bar{\rho}D)^{-1}\left[\frac{dp}{dr} - V_\theta r^{-1}[V_\theta A^{-2} - 2im(\lambda r)^{-1}]p\right], \qquad (5.39)$$

$$v_\theta = (\bar{\rho}D)^{-1}\left\{\left(r^{-1}V_\theta + \frac{dV_\theta}{dr}\right)\frac{dp}{dr} - r^{-1}\left[V_\theta^2 A^{-2}\left(r^{-1}V_\theta + \frac{dV_\theta}{dr}\right) + im\lambda\right]\right\}p, \qquad (5.40)$$

and

$$v_\xi = (\bar\rho D)^{-1}\frac{dV_\xi}{dr}\left[\frac{dp}{dr} - r^{-1}V_\theta\left(V_\theta A^{-2} - 2im(\lambda r)^{-1}\right)p\right] - \chi(\bar\rho\lambda)^{-1}p\ . \tag{5.41}$$

After substituting these expressions into the continuity equation and performing the necessary algebra we find that

$$\frac{d^2p}{dr^2} + f_1(r)\frac{dp}{dr} + f_2(r)p = 0, \tag{5.42}$$

where

$$
\begin{aligned}
f_1(r) &= \bar\rho\lambda^{-1}D\frac{d}{dr}\left[\lambda(\bar\rho D)^{-1}\right] - r^{-1}V_\theta(V_\theta A^{-2} - 2im\lambda^{-1}r^{-1}) \\
&\quad -im(\lambda r)^{-1}\left(r^{-1}V_\theta + \frac{dV_\theta}{dr}\right) + r^{-1}(A^{-2}V_\theta^2 + 1) - \lambda^{-1}\chi\frac{dV_\xi}{dr}
\end{aligned}
\tag{5.43}
$$

and

$$
\begin{aligned}
f_2(r) &= -\bar\rho\lambda^{-1}D\frac{d}{dr}\left[\lambda(\bar\rho Dr)^{-1}V_\theta(V_\theta A^{-2} - 2im\lambda^{-1}r^{-1})\right] \\
&\quad -r^{-2}V_\theta(A^{-2}V_\theta^2 + 1)(V_\theta^2 A^{-2} - 2im\lambda^{-1}r^{-1}) \\
&\quad +im\lambda^{-1}r^{-2}\left[V_\theta^2 A^{-2}\left(r^{-1}V_\theta + \frac{dV_\theta}{dr}\right) + im\lambda\right] \\
&\quad +r^{-1}V_\theta\frac{dV_\xi}{dr}\left(V_\theta^2 A^{-2} - 2im\lambda^{-1}r^{-1}\right) + \lambda^{-2}D(\chi^2 - \lambda^2 A^{-2}).
\end{aligned}
\tag{5.44}
$$

Equation (5.42) is a rather complicated ordinary differential equation which must be solved numerically subject to boundary conditions at the hub $(r = r_H)$ and duct $(r = r_D)$ walls. Nontrivial solutions of the resulting eigenvalue problem determine the radial modes $p(r)$ corresponding to the eigenvalues χ, which determine the attenuation constants and/or the axial wavenumbers of the nonconvected disturbances.

It is interesting to compare the foregoing results to those arising from this same process carried out for a uniform steady flow. If V_ξ is a constant, $V_\theta = 0$ and $\lambda = 0$. It then follows from (5.30) – (5.32) that $p(r) = 0$, the velocity of this pressure-less disturbance (i.e., the rotational velocity) is convected by the mean flow, and this velocity has a solution of the form (5.16). If $\lambda \neq 0$, the velocity components are given by Eq. (5.39) – (5.41) with dV_ξ/dr and V_θ set equal to zero, and $p(r)$ is governed by the second-order ordinary differential equation

$$\frac{d^2p}{dr^2} + r^{-1}\frac{dp}{dr} + (k^2 - m^2 r^{-2})p = 0\ , \tag{5.45}$$

where

$$k^2 = A^{-2}\left[(A^2 - V_\xi^2)\chi^2 - 2i\omega V_\xi\chi + \omega^2\right]\ . \tag{5.46}$$

Equation (5.45) is Bessel's equation of order m and has a solution of the form indicated in (5.21), and (5.46) yields solutions for χ of the form (5.22).

35

5.3 Two-Dimensional Flow in a Cylindrical Annulus

In deriving equations (5.3) through (5.5), we have assumed that the radial component of the steady velocity is zero [cf. (5.1)]. If we also assume that the radial component of the unsteady velocity is negligible, i.e., $v_r \sim \mathcal{O}(\epsilon^2)$, we can obtain analytic solutions for the first-order unsteady flow variables in the far field that account for the effects of mean swirl. Thus, if $\tilde{v}_r \sim \mathcal{O}(\epsilon^2)$, we find from (5.4) and (5.5) that the axial and circumferential variations in the unsteady velocity and pressure, within the cylindrical annulus $r_0 - dr < r < r_0 + dr$, are determined by the equations

$$\frac{\bar{D}\tilde{\mathbf{v}}}{Dt} = -\bar{\rho}\boldsymbol{\nabla}_{\mathbf{x}_0}\tilde{p} \tag{5.47}$$

$$\frac{\bar{D}\tilde{p}}{Dt} = -\bar{\rho}A^2\boldsymbol{\nabla}_{\mathbf{x}_0} \cdot \tilde{\mathbf{v}} \tag{5.48}$$

where $\mathbf{x}_0 = (r_0, \xi, \theta)$, $\bar{D}/Dt$ is defined in (5.6), $\mathbf{v} = v_\xi \mathbf{e}_\xi + v_\theta \mathbf{e}_\theta$, and

$$\boldsymbol{\nabla}_{\mathbf{x}_0} = \mathbf{e}_\xi \frac{\partial}{\partial \xi} + r^{-1}\mathbf{e}_\theta \frac{\partial}{\partial \theta} \tag{5.49}$$

In addition, the radial component of the first-order momentum equation (5.4) reduces to

$$r^{-1}V_\theta(V_\theta \tilde{s} - 2\tilde{v}_\theta) = \bar{\rho}^{-1}\left(r^{-1}A^{-2}V_\theta^2\tilde{p} - \frac{\partial \tilde{p}}{\partial r}\right) . \tag{5.50}$$

We can unwrap the cylindrical annulus, set $\mathbf{e}_\eta = \mathbf{e}_\theta$, $V_\eta = V_\theta$, $v_\eta = v_\theta$, and $\partial/\partial\eta = r^{-1}\partial/\partial\theta$, and regard ξ and η as Cartesian axial and tangential coordinates such that $\mathbf{e}_\xi \times \mathbf{e}_\eta = \mathbf{e}_z$ points out from the page. In this case equations (5.3), (5.47) and (5.48) govern the two-dimensional, linearized, unsteady perturbation of a uniform stream flowing at an angle $\Omega = \tan^{-1}(V_\eta/V_\xi)$ to the axial direction. As for the case of uniform mean flow in a cylindrical duct, the unsteady vorticity $\boldsymbol{\zeta} = \boldsymbol{\nabla} \times \mathbf{v} = \zeta \mathbf{e}_z$ (or $-\zeta \mathbf{e}_r$) associated with this two-dimensional flow is convected by the mean flow, the pressure is governed by a (two-dimensional) convected wave equation, and the unsteady velocity can be decomposed into rotational, $\tilde{\mathbf{v}}_R$, and irrotational, $\tilde{\mathbf{v}}_I = \boldsymbol{\nabla}\tilde{\phi}$, components. The rotational velocity determines the unsteady vorticity and is convected by the mean flow, the velocity potential determines the pressure and is governed by a convected wave equation.

For an unsteady perturbation that is harmonic in time and periodic in the tangential, η, (or circumferential, θ) directions the (two-dimensional) solutions for the complex amplitudes of the first-order unsteady entropy and rotational velocity are

$$s(\mathbf{x}_0) = \sum_{m=-\infty}^{\infty} s_m(r_0)\exp[i(\kappa_{\xi,m}\xi + \kappa_{\eta,m}\eta)] \tag{5.51}$$

and

$$\mathbf{v}_R(\mathbf{x}_0) = \sum_{m=-\infty}^{\infty} \mathbf{v}_{R,m}(r_0)\exp[i(\kappa_{\xi,m}\xi + \kappa_{\eta,m}\eta)] \tag{5.52}$$

where $\kappa_{\eta,m} = mr_0^{-1}$ is the "circumferential" wave number of the mth disturbance, and $\kappa_{\xi,m} = -(\omega + \kappa_{\eta,m}V_\eta)V_\xi^{-1}$ is the axial wave number of the mth entropic and rotational velocity disturbances.

36

The solution of the two-dimensional convected wave equation for the complex amplitude of the pressure, as determined by the method of separation of variables, is

$$p(\mathbf{x}_0) = \sum_{m=-\infty}^{\infty} p_m(r_0) \exp(\chi_m \xi + i\kappa_{\eta,m}\eta) \tag{5.53}$$

where

$$\chi_m = \beta_m + i\kappa_{\xi,m} = \mp d_m + iM^2\delta_m \cos\Omega \ ,$$

$$\delta_m = (\omega V^{-1} + \kappa_{\eta,m}\sin\Omega)/(1 - M^2\cos^2\Omega) \ , \tag{5.54}$$

$$d_m^2 = (1 - M^2\cos^2\Omega)^{-1}\kappa_{\eta,m}^2 - M^2\delta_m^2$$

and d_m is the principal root of d_m^2; i.e., $d_m = |d_m|$ if $d_m^2 > 0$ and $d_m = i|d_m|$ if $d_m^2 < 0$.

If $d_m^2 \neq 0$, each fundamental solution describes two wave-like disturbances which, depending upon the sign of d_m^2, either grow or decay exponentially in the axial direction ($d_m^2 > 0$) or propagate carrying energy away from or toward the blade row ($d_m^2 < 0$). The condition $d_m^2 = 0$ which divides these two types of behavior is referred to as the "cut off" or acoustic resonance condition. In each case, $d_m^2 > 0$, $d_m^2 < 0$ or $d_m^2 = 0$, we can write

$$p_m(\mathbf{x}_0) = p_m(r_0)\exp[(h_m d_m + iM^2\delta_m \cos\ \Omega)\xi + ik_{\eta,m}\eta] \ , \tag{5.55}$$

where the correct value of h_m (i.e., +1 or −1) for $d_m^2 \neq 0$, must be determined by whether the pressure wave travels in the positive or negative axial directions.

The two-dimensional, far-field, conditions account for the effects of mean swirl, and for this reason they are often applied (in "strips") in three-dimensional unsteady flow calculations. These conditions do not properly account for the radial dependence of the unsteady flow variables. Consequently, solutions determined using this quasi-three-dimensional (or strip theory) approach may be of limited use for forced vibration and aeroacoustic response studies in which the excitation frequencies of interest are usually high, i.e., $\omega \sim \mathcal{O}(10)$.

5.4 Numerical Far-Field Boundary Conditions

The development of numerical far-field boundary conditions typically involves an examination of an approximate set of linear unsteady equations followed by a decomposition of the unsteady disturbances into incoming and outgoing waves. The incoming and outgoing disturbances at the far-field boundaries are determined by the characteristics of the governing equations. The characteristic values or eigenvalues represent the velocities of the fundamental disturbance waves, and the eigenfunctions describe the shapes of these waves. Conditions must be formulated to neutralize undesired incoming disturbances. Such conditions are termed "non-reflecting."

We can write the first-order unsteady equations (5.3) – (5.5), in matrix form, i.e.,

$$\frac{\partial \tilde{\mathbf{u}}^p}{\partial t} + \mathbf{A}\frac{\partial \tilde{\mathbf{u}}^p}{\partial r} + \mathbf{B}r^{-1}\frac{\partial \tilde{\mathbf{u}}^p}{\partial \theta} + \mathbf{C}\frac{\partial \tilde{\mathbf{u}}^p}{\partial \xi} + \mathbf{D}\tilde{\mathbf{u}}^p = 0 \tag{5.56}$$

where

$$
\tilde{u}^p = \begin{Bmatrix} \tilde{s} \\ \tilde{v}_r \\ \tilde{v}_\theta \\ \tilde{v}_\xi \\ \tilde{p} \end{Bmatrix}, \qquad
A = \begin{bmatrix} 0 & 0 & 0 & 0 & 0 \\ 0 & 0 & 0 & 0 & \bar{\rho}^{-1} \\ 0 & 0 & 0 & 0 & 0 \\ 0 & 0 & 0 & 0 & 0 \\ 0 & \bar{\rho}A^2 & 0 & 0 & 0 \end{bmatrix},
\tag{5.57}
$$

$$
B = \begin{bmatrix} V_\theta & 0 & 0 & 0 & 0 \\ 0 & V_\theta & 0 & 0 & 0 \\ 0 & 0 & V_\theta & 0 & \bar{\rho}^{-1} \\ 0 & 0 & 0 & V_\theta & 0 \\ 0 & 0 & \bar{\rho}A^2 & 0 & V_\theta \end{bmatrix}, \quad
C = \begin{bmatrix} V_\xi & 0 & 0 & 0 & 0 \\ 0 & V_\xi & 0 & 0 & 0 \\ 0 & 0 & V_\xi & 0 & 0 \\ 0 & 0 & 0 & V_\xi & \bar{\rho}^{-1} \\ 0 & 0 & 0 & \bar{\rho}A^2 & V_\xi \end{bmatrix},
\tag{5.58}
$$

and

$$
D = \begin{bmatrix} 0 & 0 & 0 & 0 & 0 \\ r^{-1}V_\theta^2 & 0 & -2r^{-1}V_\theta & 0 & -(\bar{\rho}r)^{-1}A^{-2}V_\theta^2 \\ 0 & r^{-1}V_\theta + dV_\theta/dr & 0 & 0 & 0 \\ 0 & dV_\xi/dr & 0 & 0 & 0 \\ 0 & \bar{\rho}r^{-1}(V_\theta^2 + A^2) & 0 & 0 & 0 \end{bmatrix}
\tag{5.59}
$$

The components of the column vector $\tilde{u}^p$ are the primitive unsteady flow variables; those of the matrices A, B, C and D are determined by the mean or steady background flow.

One-Dimensional Conditions

We assume that $\tilde{v}_r \sim \mathcal{O}(\epsilon^2)$, the unsteady entropy, circumferential velocity and pressure are related by (5.50), and the circumferential variations $(\partial\,/\partial\theta)$ in the unsteady flow properties are of $\mathcal{O}(\epsilon^2)$. Then, the components of the column vectors $A\partial\tilde{u}^p/\partial r + D\tilde{u}^p$ and $Br^{-1}\partial\tilde{u}^p/\partial\Theta$ are at most of $\mathcal{O}(\epsilon^2)$, and the system of equations (5.56) for the first-order unsteady flow variables can be approximated by

$$
\frac{\partial\tilde{u}^p}{\partial t} + C\frac{\partial\tilde{u}^p}{\partial\xi} = 0 \ .
\tag{5.60}
$$

Note that, although we have assumed $\tilde{v}_r \sim \mathcal{O}(\epsilon^2)$ in deriving (5.60), a convective equation for v_r has been retained within this system of equations.

The matrix C can be diagonalized by employing a similarity transformation, i.e.,

$$
S^{-1}CS = \Lambda
\tag{5.61}
$$

where S contains the eigenvectors of C as its columns and Λ is a diagonal matrix whose elements are the eigenvalues of C. Premultiplying (5.60) by S^{-1} and transforming to the characteristic variables $\tilde{c} = S^{-1}\tilde{u}^p$ results in

$$
\frac{\partial\tilde{c}}{\partial t} + \Lambda\frac{\partial\tilde{c}}{\partial\xi} = 0
\tag{5.62}
$$

Equation (5.62) leads to an application of "one-dimensional" boundary conditions to the three-dimensional unsteady problem. Such an application is effective if the unsteady disturbance waves travel along lines that are nearly parallel to the ξ-axis. The matrix S is used

38

in transforming from characteristic to physical variables via the equation $\tilde{\mathbf{u}}^P = \mathbf{S}\tilde{\mathbf{c}}$. In the present application $\mathbf{S}$ and its inverse, $\mathbf{S}^{-1}$, are given by

$$
\mathbf{S} = \begin{bmatrix} 1 & 0 & 0 & 0 & 0 \\ 0 & 1 & 0 & 0 & 0 \\ 0 & 0 & 1 & 0 & 0 \\ 0 & 0 & 0 & 1 & 1 \\ 0 & 0 & 0 & \bar{\rho}A & -\bar{\rho}A \end{bmatrix} \quad \text{and} \quad \mathbf{S}^{-1} = \begin{bmatrix} 1 & 0 & 0 & 0 & 0 \\ 0 & 1 & 0 & 0 & 0 \\ 0 & 0 & 1 & 0 & 0 \\ 0 & 0 & 0 & 1/2 & (2\bar{\rho}A)^{-1} \\ 0 & 0 & 0 & 1/2 & -(2\bar{\rho}A)^{-1} \end{bmatrix} \tag{5.63}
$$

The five eigenvalues of the matrix $\mathbf{C}$ are

$$
\lambda_1 = \lambda_2 = \lambda_3 = V_\xi , \quad \lambda_4 = V_\xi + A , \quad \text{and} \quad \lambda_5 = V_\xi - A . \tag{5.64}
$$

For subsonic flow, the first four eigenvalues of $\mathbf{C}$ are positive and the fifth is negative. Therefore, at the inlet boundary, there are four waves entering the computational domain which must be specified, and one wave exiting which is extrapolated from the interior. At the downstream boundary, waves corresponding to the first four eigenvalues are exiting the domain and are therefore extrapolated, while the wave corresponding to λ_5 must be specified. For example, if it is assumed that there are no external excitations, then the conditions $\tilde{c}_1 = \tilde{c}_2 = \tilde{c}_3 = \tilde{c}_4 = 0$ are specified at the upstream boundary, and $\tilde{c}_5 = 0$ is specified at the downstream boundary. These conditions imply that

$$
\tilde{s} = 0 , \quad \tilde{v}_r = 0 , \quad \tilde{v}_\theta = 0 , \quad \tilde{v}_\xi = \tilde{c}_5 , \quad \text{and} \quad \tilde{p} = -\bar{\rho}A\tilde{c}_5 , \tag{5.65}
$$

at the upstream boundary where the value of $\tilde{c}_5$ is extrapolated from the interior of the solution domain. At the downstream boundary

$$
\tilde{s} = \tilde{c}_1 , \quad \tilde{v}_r = \tilde{c}_2 , \quad \tilde{v}_\theta = \tilde{c}_3 , \quad \tilde{v}_\xi = \tilde{c}_4 , \quad \text{and} \quad \tilde{p} = +\bar{\rho}A\tilde{c}_4 , \tag{5.66}
$$

where, here, the values of $\tilde{c}_1, \tilde{c}_2, \tilde{c}_3$, and $\tilde{c}_4$ are extrapolated from the interior.

Two-Dimensional Conditions

The one-dimensional boundary conditions are useful if all unsteady disturbance waves travel nearly in the positive or negative axial directions. Two-dimensional conditions which allow for both axial and circumferential variations in the unsteady disturbances can be determined by analyzing the coefficient matrices $\mathbf{B}$ and $\mathbf{C}$ in (5.56). The approach is detailed in [Gil90], and its application to three-dimensional flow which yields "quasi-three-dimensional" boundary conditions is discussed in [SG91].

In developing the two-dimensional far-field conditions, the equations of motion (5.56) are approximated by

$$
\frac{\partial \tilde{\mathbf{u}}^P}{\partial t} + \mathbf{B}r^{-1}\frac{\partial \tilde{\mathbf{u}}^P}{\partial \theta} + \mathbf{C}\frac{\partial \tilde{\mathbf{u}}^P}{\partial \xi} = 0 \tag{5.67}
$$

This approximation is equivalent to setting $\tilde{v}_r \equiv 0$ in the circumferential and axial momentum equations in (5.4) and in the continuity equation (5.5), assuming that (5.50) holds, and replacing the radial momentum equation in (5.4) by $\bar{D}\tilde{v}_r/Dt \equiv 0$. If we consider a wave-like solution of the form

$$
\tilde{\mathbf{u}}^P(\xi, \theta, t) = \mathbf{u}\exp[\chi\xi + i(m\theta + \omega t)] , \tag{5.68}
$$

39

where χ, m and ω are constants, and substitute (5.68) into (5.67), we find that

$$[i\omega\mathbf{I} + imr^{-1}\mathbf{B} + \chi\mathbf{C}]\mathbf{u} = 0 , \qquad (5.69)$$

where $\mathbf{I}$ is the identity matrix. In general, ω and m are specified, and χ must be determined. A right eigenvector $\mathbf{u}^R$ of the system (5.69) is determined by solving the equation

$$[i\omega\mathbf{I} + imr^{-1}\mathbf{B} + \chi\mathbf{C}]\mathbf{u}^R = 0 \qquad (5.70)$$

indicating that $\mathbf{u}^R$ corresponds to the eigenvalue $-i\omega$ of the matrix $[imr^{-1}\mathbf{B} + \chi\mathbf{C}]$. Premultiplying (5.70) by $\mathbf{C}^{-1}$ yields

$$\mathbf{C}^{-1}[i\omega\mathbf{I} + imr^{-1}\mathbf{B} + \chi\mathbf{C}]\mathbf{u}^R = 0 \qquad (5.71)$$

so that $\mathbf{u}^R$ is also the right eigenvector of the matrix $[i\omega\mathbf{C}^{-1} + imr^{-1}\mathbf{C}^{-1}\mathbf{B}]$ corresponding to the eigenvalue $-\chi$. The perturbation vector $\tilde{\mathbf{u}}$ can be expressed as a linear combination of the right eigenvectors $\mathbf{u}_n^R$, $n = 1, 2, \ldots, 5$, with eigenvalues $-\chi_n$, i.e.,

$$\tilde{\mathbf{u}}^p = \left(\sum_{n=1}^{5} a_n \mathbf{u}_n^R \exp[\chi_n\xi] \right) \exp[i(m\theta + \omega t)] . \qquad (5.72)$$

Analogously, a left eigenvector $\mathbf{u}^L$ of the matrix $[imr^{-1}\mathbf{B} + \chi\mathbf{C}]$ corresponding to eigenvalue $-i\omega$ is defined by

$$\mathbf{u}^L[i\omega\mathbf{I} + imr^{-1}\mathbf{B} + \chi\mathbf{C}] = 0 , \qquad (5.73)$$

and a left eigenvector $\mathbf{v}^L$ of the matrix $i\omega\mathbf{C}^{-1} + imr^{-1}\mathbf{C}^{-1}\mathbf{B}$ corresponding to the eigenvalue $-\chi$ is defined by

$$\mathbf{v}^L\mathbf{C}^{-1}[i\omega\mathbf{I} + imr^{-1}\mathbf{B} + \chi\mathbf{C}] = 0 \qquad (5.74)$$

The right and left eigenvectors corresponding to the eigenvalues χ_n are thus $\mathbf{u}_n^R$ and $\mathbf{v}_n^L = \mathbf{u}_n^L\mathbf{C}$. It can be shown that the scalar product $\mathbf{v}_m^L \cdot \mathbf{u}_n^R = 0$ for $m \neq n$, so premultiplying (5.72) by $\mathbf{v}_m^L$ results in

$$\mathbf{v}_n^L \cdot \tilde{\mathbf{u}}^p = a_n(\mathbf{v}_n^L \cdot \mathbf{u}_n^R)\exp[\chi_n\xi]\exp[i(m\theta + \omega t)] , n = 1, 2, \ldots, 5 \qquad (5.75)$$

Nonreflecting boundary conditions are found by identifying which of the 5 modes correspond to incoming waves at the boundaries, and specifying the constants a_n in (5.75) for those waves.

For the two-dimensional system (5.69), the eigenvalues are found from the determinant of the coefficient matrix, which yields

$$\left[i(\omega + mr^{-1}V_\theta) + \chi_n V_\xi\right]^3 \left\{ \left[i(\omega + mr^{-1}V_\theta) + \chi_n V_\xi\right]^2 + A^2(m^2r^{-2} - \chi_n^2)\right\} = 0 \qquad (5.76)$$

This equation is a dispersion relation that relates the wave number of a given disturbance to its frequency. Three of its roots are identical, and are given by [cf. (5.34)]

$$\chi_{1,2,3} = -i(\omega + mr^{-1}V_\theta)V_\xi^{-1} = i\kappa_\xi \qquad (5.77)$$

40

indicating that the disturbances associated with these roots are convected by the mean flow and that they do not decay with axial distance. The remaining two roots are found by solving the quadratic in (5.76), which gives,

$$(A^2 - V_\xi^2)\chi_{4,5} = i(\omega + mr^{-1}V_\theta)V_\xi \mp (A^2 - V_\xi^2)d_m \tag{5.78}$$

where

$$(A^2 - V_\xi^2)d_m = A\sqrt{(A^2 - V_\xi^2)(mr^{-1})^2 - (\omega + mr^{-1}V_\theta)^2}. \tag{5.79}$$

These results become identical to those given in (5.54) if we replace mr^{-1} by κ_η and V_θ by V_η. The corresponding right eigenvectors are given by

$$\mathbf{u}_1^R = \left\{ \begin{array}{c} 1 \\ 0 \\ 0 \\ 0 \\ 0 \end{array} \right\}, \quad \mathbf{u}_2^R = \left\{ \begin{array}{c} 0 \\ 1 \\ 0 \\ 0 \\ 0 \end{array} \right\}, \quad \mathbf{u}_3^R = \left\{ \begin{array}{c} 0 \\ 0 \\ (mV_\xi)^{-1}r\gamma \\ 1 \\ 0 \end{array} \right\}, \quad \mathbf{u}_{4,5}^R = \left\{ \begin{array}{c} 0 \\ 0 \\ im(\bar{\rho}r)^{-1} \\ \bar{\rho}^{-1}\chi_{4,5} \\ -(i\gamma + \chi_{4,5}V_\xi) \end{array} \right\}. \tag{5.80}$$

where $\gamma = \omega + mr^{-1}V_\theta$. The left eigenvectors $\mathbf{v}_n^L$ are given by

$$\mathbf{v}_1^L = \{1 \quad 0 \quad 0 \quad 0 \quad 0\}$$

$$\mathbf{v}_2^L = \{0 \quad 1 \quad 0 \quad 0 \quad 0\}$$

$$\mathbf{v}_3^L = \{0 \quad 0 \quad (mV_\xi)^{-1}r\gamma \quad 1 \quad (\bar{\rho}V_\xi)^{-1}\} \tag{5.81}$$

and

$$\mathbf{v}_{4,5}^L = \left\{0 \quad 0 \quad im(\bar{\rho}r)^{-1} \quad -i\gamma(\bar{\rho}V_\xi)^{-1} \quad (\bar{\rho}A)^{-2}V_\xi^{-1}\left[(A^2 - V_\xi^2)\chi_{4,5} - i\gamma V_\xi\right]\right\}.$$

The first eigenvector is associated with an entropic disturbance, the second and third with vortical disturbances, and the fourth and fifth with downstream and upstream moving acoustic disturbances.

Assuming that there are no specified external disturbances entering the domain, it is necessary to specify

$$\mathbf{v}_n^L \cdot \check{\mathbf{u}}^P = 0, \; n = 1,2,3,4 \quad \text{and} \quad \mathbf{v}_n^L \cdot \check{\mathbf{u}}^P = 0, \; n = 5 \tag{5.82}$$

at the upstream boundary and downstream boundaries, respectively.

Alternative Techniques

Both the one-dimensional and the two-dimensional far field conditions presented above provide only approximate representations of the three-dimensional, unsteady flow behavior in the far field of a blade row operating within a cylindrical duct. Since the full system of equations contains variable coefficients, an extension of these techniques to three dimensional flows is not readily apparent. One alternative approach used in flutter calculations is to stretch the computational grid in the axial direction so as to dissipate acoustic response waves that travel away from the blade row and thereby prevent the occurrence of any reflected

41

waves. This approach can not be used in forced vibration or noise generation studies, in which external aerodynamic excitations and far-field acoustic responses must be accurately modeled.

Current aeroacoustic analyses make use of the three-dimensional analytic solutions available for uniform axial mean flows. This has the benefit of accounting for the radial behavior of acoustic disturbances, but ignores the effects of mean swirl. As such, it is only useful in special situations, e.g., to represent the unsteady flow ahead of the first blade row of a machine. The technique generally employed in modern computational simulations is to use the analytic solutions available for two-dimensional flows in a strip-theory fashion. This quasi-three-dimensional approach [SG91] incorporates the effects of mean swirl, but it does not properly account for radial variations in the unsteady flow quantities. An examination of radial mode behavior in uniform, axial, mean flows (e.g., see Figure 3) indicates that this approach may not be very useful for aeroacoustic response studies.

Another approach that has been tried for two-dimensional flows is due to Hall and Clark [HC93a], wherein the fluid dynamic field equations are first discretized and an eigenvalue analysis is performed on the resulting set of discretized equations. This method computes the eigenvalues and eigenvectors of the discretized system, and any incoming disturbances are then specified at the boundaries. Since the orders of the matrices involved in this type of analysis are quite large, the method is computationally intensive. The technique also requires constant coefficient matrices, and thus it contains the same difficulties for nonuniform mean flows as the analytical and characteristic-based methods described herein.

One potentially promising approach to finding useful three-dimensional solutions for far-field unsteady disturbances is to develop reliable methods for solving the ordinary differential equation (5.42) for the radial behavior of the unsteady pressure in a nonuniform mean flow. By integrating this equation numerically, subject to boundary conditions at the duct walls, both the eigenvalues and the radial mode shapes can be determined. In principle, the resulting far-field solutions can be coupled to an interior numerical solution to complete the description of the unsteady flow field.

6. Numerical Model

The governing equations for the nonlinear three-dimensional unsteady flow problem were formulated in §3; those for the three-dimensional steady and linearized unsteady flow problems, in §4. In this Section, approximate representations of these equations will be developed using both finite difference and finite volume discretizations. Also, the particular finite volume model used in the development of the NPHASE and LINFLUX codes will be described.

The numerical model for solving the three-dimensional unsteady, steady and linearized unsteady flow problems is based on the nonlinear, time-marching, Euler analysis originally developed by Whitfield, Janus and Simpson [WJS88], and subsequently extended for turbomachinery unsteady aerodynamic applications by Huff, Swafford and Reddy [HSR91]. The latter authors provided an implicit, multi-block, finite-volume analysis and computer code, called NPHASE, for predicting nonlinear, two-dimensional, unsteady flows through vibrating cascades. This analysis has been shown to be robust, with a proven capability to predict transonic flows with sharp shock definitions, and accurate, allowing second and third-order spatial discretizations. A detailed description of the latest version of NPHASE can be found in [SLH+94] and the references cited therein. Under the present effort the NPHASE code has been modified to take advantage of the efficiencies inherent in a linearized unsteady aerodynamic formulation. The linearized version of NPHASE is called LINFLUX.

6.1 Discretization of Physical Domain

In order to develop a discrete approximation to the governing equations, the physical domain must first be described as a set of discrete points, that form a computational mesh or grid. For the NPHASE and LINFLUX analyses, the computational mesh is a sheared H-mesh, typically generated using the IGB grid generation package of [BH92]. This structured mesh defines a curvilinear coordinate system, the boundaries of which lie along the boundaries of the physical domain, such that there is a one-to-one transformation from points in the physical domain, $(\mathbf{x})$, to points in the computational domain, $(\boldsymbol{\alpha})$. Such a transformation allows clustering of grid points in regions where flow variables undergo high gradients and accounts for any grid point motion. A time-dependent coordinate transformation, $(\mathbf{x}, t) \rightarrow (\boldsymbol{\alpha}, t)$, from the physical domain, in which the grid deforms with the blade motion, to the computational domain, in which the grid is fixed, can be applied to simplify the implementation of numerical differencing and boundary conditions. The numerical grid is usually defined to be uniform, orthogonal and stationary in computational space for convenience in defining finite-difference approximations. This type of coordinate transformation is described by Anderson, et al. [ATP84] and illustrated in Figures 4a and 4c.

Finite-Difference Coordinate Transformation Metrics

For finite difference approximations, expressed in the computational domain, we consider a transformation $(\mathbf{X} \rightarrow \mathcal{A})$ of the governing equations from physical $(\mathbf{x}, t)$ to computational $(\boldsymbol{\alpha}, t^c)$ coordinates. Note that time is defined to be the same in the two coordinate systems, but has been given separate symbols, t and t^c, to avoid confusion. For arbitrary physical domains the transformation from physical to computational coordinates must, in general,

43

be defined numerically, and is typically done by solving a set of elliptic partial differential equations, as described by Thompson, et al. [TTM77], for (x, t) in terms of (α, t^c). This inverse transformation, $\mathcal{A} \rightarrow \mathbf{X}$, contains all the information needed to describe the location of the grid points in physical space and to determine the metrics $\partial x_k / \partial t^c$ and $\partial x_k / \partial \alpha_j, j, k = 1, 2, 3$. However, the metrics of the forward transformation, $\mathbf{X} \rightarrow \mathcal{A}$, appear explicitly when the governing equations are written in terms of computational coordinates; therefore, the values of the forward metrics $\partial \alpha_j / \partial t$ and $\partial \alpha_j / \partial x_k$ must also be determined.

For a formulation based on the differential form of the governing equations the forward metrics are obtained by considering total differentials in the two (physical and computational) coordinate systems, i.e.,

$$
d\mathbf{X} = \begin{bmatrix} dt \\ dx_1 \\ dx_2 \\ dx_3 \end{bmatrix} = \begin{bmatrix} 1 & 0 & 0 & 0 \\ \dfrac{\partial x_1}{\partial t^c} & \dfrac{\partial x_1}{\partial \alpha_1} & \dfrac{\partial x_1}{\partial \alpha_2} & \dfrac{\partial x_1}{\partial \alpha_3} \\ \dfrac{\partial x_2}{\partial t^c} & \dfrac{\partial x_2}{\partial \alpha_1} & \dfrac{\partial x_2}{\partial \alpha_2} & \dfrac{\partial x_2}{\partial \alpha_3} \\ \dfrac{\partial x_3}{\partial t^c} & \dfrac{\partial x_3}{\partial \alpha_1} & \dfrac{\partial x_3}{\partial \alpha_2} & \dfrac{\partial x_3}{\partial \alpha_3} \end{bmatrix} \begin{bmatrix} dt^c \\ d\alpha_1 \\ d\alpha_2 \\ d\alpha_3 \end{bmatrix} = \mathbf{I}^{\alpha x} d\mathcal{A} \tag{6.1}
$$

and

$$
d\mathcal{A} = \begin{bmatrix} dt^c \\ d\alpha_1 \\ d\alpha_2 \\ d\alpha_3 \end{bmatrix} = \begin{bmatrix} 1 & 0 & 0 & 0 \\ \dfrac{\partial \alpha_1}{\partial t} & \dfrac{\partial \alpha_1}{\partial x_1} & \dfrac{\partial \alpha_1}{\partial x_2} & \dfrac{\partial \alpha_1}{\partial x_3} \\ \dfrac{\partial \alpha_2}{\partial t} & \dfrac{\partial \alpha_2}{\partial x_1} & \dfrac{\partial \alpha_2}{\partial x_2} & \dfrac{\partial \alpha_2}{\partial x_3} \\ \dfrac{\partial \alpha_3}{\partial t} & \dfrac{\partial \alpha_3}{\partial x_1} & \dfrac{\partial \alpha_3}{\partial x_2} & \dfrac{\partial \alpha_3}{\partial x_3} \end{bmatrix} \begin{bmatrix} dt \\ dx_1 \\ dx_2 \\ dx_3 \end{bmatrix} = \mathbf{J}^{x\alpha} d\mathbf{X} \tag{6.2}
$$

where $\mathbf{J}^{x\alpha}$ and $\mathbf{I}^{\alpha x}$ are the matrices of the forward , $(x, t) \rightarrow (\alpha, t^c)$ and the inverse, $(\alpha, t^c) \rightarrow (x, t)$, transformations, respectively. The two matrices $\mathbf{J}^{x\alpha}$ and $\mathbf{I}^{\alpha x}$ are inverses of each other, i.e.,

$$
\mathbf{J}^{x\alpha} = (\mathbf{I}^{\alpha x})^{-1} . \tag{6.3}
$$

Equation (6.3) provides the needed relationships between the forward, $\partial \alpha_j / \partial x_k$, and inverse, $\partial x_k / \partial \alpha_j$, metrics. The Jacobians $J^{x\alpha} = det(\mathbf{J}^{x\alpha}) = (I^{\alpha x})^{-1}$ and $I^{\alpha x} = det(\mathbf{I}^{\alpha x}) = (J^{x\alpha})^{-1}$ of the forward and inverse transformations are referred to as metric Jacobians.

Finite Volume Geometry

For a finite volume discretization, based on the integral forms of the governing field equations, the geometries of the mesh cells in physical space are required. The mesh points define the eight vertices of the non-overlapping hexahedral cells which fill the physical solution domain. Cell faces are surfaces of constant computational coordinate, so that each cell

44

is bounded by the six surfaces, say $\alpha_1 = I, I - 1$ and $\alpha_2 = J, J - 1$ and $\alpha_3 = K, K - 1$. The connectivity of the cells is thus known from the computational coordinates, with neighboring cells given by changing a computational coordinate by one.

The geometric properties of the cell are computed from the locations of the cell vertices. For example, the area vector of a cell face is given by the cross product of the directed line segments that cross the cell face from "lower left" to "upper right" and from "lower right" to "upper left". Let subscripts correspond to mesh indices, then the area vector of a constant α_1 face is

$$\mathbf{A}_I = \frac{1}{2} \left(\mathbf{x}_{I,J,K} - \mathbf{x}_{I,J-1,K-1} \right) \times \left(\mathbf{x}_{I,J-1,K} - \mathbf{x}_{I,J,K-1} \right) , \qquad (6.4)$$

and similar expressions exist for constant α_2 faces, $\mathbf{A}_J$, and constant α_3 faces, $\mathbf{A}_K$. The components of the area vectors can be treated as a matrix, with A_{jk} being the area of the constant α_j face projected in the x_k direction. These area vectors are illustrated for a two-dimensional geometry in the accompanying sketch.
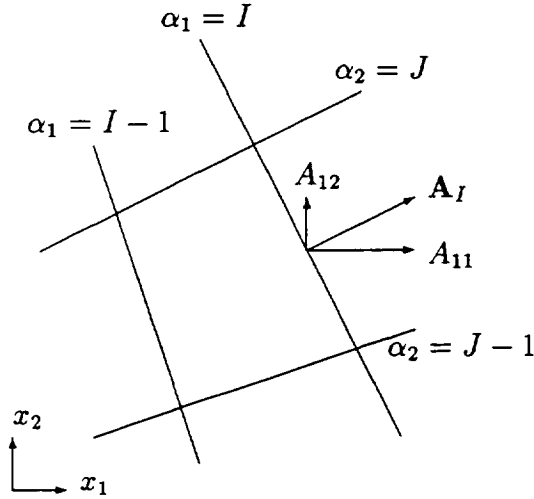
Two-dimensional cell with face area vectors.

The cell volume can be computed from the six face area vectors and the location of the mid-points of the faces. Let the mid-point of a constant $\alpha_1 = I$ face be $\mathbf{x}_{I,\text{mid}}$, so that the distance between mid-points across the cell in the α_1 direction is

$$\Delta \mathbf{x}_I = \mathbf{x}_{I,\text{mid}} - \mathbf{x}_{I-1,\text{mid}} \qquad (6.5)$$

The cell volume is then

$$\vartheta = \frac{1}{6} \left[\left(\mathbf{A}_I + \mathbf{A}_{I-1} \right) \cdot \Delta \mathbf{x}_I + \left(\mathbf{A}_J + \mathbf{A}_{J-1} \right) \cdot \Delta \mathbf{x}_J + \left(\mathbf{A}_K + \mathbf{A}_{K-1} \right) \cdot \Delta \mathbf{x}_K \right] \qquad (6.6)$$

which is equivalent to adding the volumes of the pentahedrons defined by each cell face and the center point of the cell.

45

6.2 Nonlinear Analysis

The equations that describe nonlinear, inviscid, unsteady flow through a rotating blade row have been given in §3 of this report. For cascades in which the blades are vibrating, the points, $\mathbf{x}$, move in physical space, i.e., $\mathbf{x} = \bar{\mathbf{x}} + \mathcal{R}(\bar{\mathbf{x}}, t)$ is the instantaneous position of a moving field point having its reference position at $\bar{\mathbf{x}}$. Currently, two methods are used for determining the unsteady displacement field, $\mathcal{R}(\bar{\mathbf{x}}, t)$. The NPHASE code originally contained the grid motion formulation of Huff [Huf87], which is based on an algebraic description. As part of the present effort a grid motion formulation, based on a displacement field that is determined as a solution of Laplace's equation subject to Dirichlet boundary conditions at the blade surfaces and in the far field, was incorporated into NPHASE. The latter formulation, which is described in §6.3, is more robust than the algebraic formulation in that larger amplitudes of blade motion can be considered without grid line intersections occurring.

Finite Difference Approximation

Since the mesh is time dependent, a time-dependent coordinate transformation, $(\mathbf{x}, t) \to (\boldsymbol{\alpha}, t^c)$, from the deforming mesh in the physical domain to the fixed mesh in the computational domain is applied. The Euler governing equations (3.37) can be written in terms of the computational coordinates $\boldsymbol{\alpha}$ and t^c by applying the chain rule of partial differentiation, i.e.,

$$\frac{\partial}{\partial t} = \frac{\partial}{\partial t^c} + \frac{\partial \alpha_j}{\partial t}\frac{\partial}{\partial \alpha_j} \quad \text{and} \quad \frac{\partial}{\partial x_k} = \frac{\partial \alpha_j}{\partial x_k}\frac{\partial}{\partial \alpha_j} \quad , \tag{6.7}$$

leading to equations of the form

$$\left(\frac{\partial}{\partial t^c} + \frac{\partial \alpha_j}{\partial t}\frac{\partial}{\partial \alpha_j} \right)\tilde{\mathbf{U}} + \frac{\partial \alpha_j}{\partial x_k}\frac{\partial}{\partial \alpha_j}\tilde{\mathbf{F}}_k = \tilde{\mathbf{S}} \ . \tag{6.8}$$

Equation (6.8) can be written in strong conservation form by multiplying all terms by $(J^{x\alpha})^{-1} = I^{\alpha x}$ and making use of the tensor identities

$$\frac{\partial}{\partial \alpha_j}\left(I^{\alpha x}\frac{\partial \alpha_j}{\partial x_k} \right) = 0 \quad \text{and} \quad \frac{\partial I^{\alpha x}}{\partial t^c} + \frac{\partial}{\partial \alpha_j}\left(I^{\alpha x}\frac{\partial \alpha_j}{\partial t} \right) = 0 \tag{6.9}$$

After applying the necessary algebra, we find that

$$\frac{\partial}{\partial t^c}\bar{\mathbf{U}} + \frac{\partial}{\partial \alpha_j}\bar{\mathbf{F}}_j = \bar{\mathbf{S}} \tag{6.10}$$

where

$$\bar{\mathbf{U}} = I^{\alpha x}\tilde{\mathbf{U}}, \quad \bar{\mathbf{F}}_j = I^{\alpha x}\left(\frac{\partial \alpha_j}{\partial t}\tilde{\mathbf{U}} + \frac{\partial \alpha_j}{\partial x_k}\tilde{\mathbf{F}}_k \right), \quad \text{and} \quad \bar{\mathbf{S}} = I^{\alpha x}\tilde{\mathbf{S}} \ . \tag{6.11}$$

46

In order to apply a finite volume discretization, the Euler governing equations (3.37) must be written in terms of the cell geometry. For example, in three dimensions the cell geometry is defined by ϑ, the cell volume, $\dot{\vartheta}_j$, the volume swept out per unit time by the constant α_j face as the cell interface moves, and A_{jk}, the area of the constant α_j face projected in the x_k direction. Thus, we can write the finite volume spatial discretization of equation (3.37) as

$$\frac{\partial \bar{\tilde{U}}}{\partial t^c}\bigg|_{\alpha} = -\delta_j \bar{\tilde{F}}_j + \bar{\tilde{S}} = -\bar{\tilde{R}} \tag{6.12}$$

where

$$\bar{\tilde{U}} = \vartheta \tilde{U} \quad , \quad \bar{\tilde{F}}_j = -\dot{\vartheta}_j \tilde{U} + A_{jk}\tilde{F}_k \quad , \quad \text{and} \quad \bar{\tilde{S}} = \vartheta \tilde{S} \tag{6.13}$$

In equation (6.13) the vectors $\tilde{U}$ and $\tilde{S}$ represent averages over the cell volume of the conserved quantities and the source terms, respectively. In equation (6.12) the vector $\bar{\tilde{F}}_j$ is the flux across a constant α_j face; the symbol δ_j represents the difference across adjacent cell interfaces, i.e. $\delta_j(\ ) = (\ )_{j+1/2} - (\ )_{j-1/2}$; and $\bar{\tilde{R}}$ is referred to as the residual. The repeated j index implies summation over all computational coordinate directions, so that the term $\delta_j \bar{\tilde{F}}_j$ is the net flux through the cell. Since the grid deforms as the blades move, the cell geometry terms, ϑ, $\dot{\vartheta}_j$ and A_{jk}, are time dependent.

The finite difference and finite volume discretizations are seen to be related if the transformation metrics of the finite difference discretization are interpreted in terms of cell geometry. For example, in three dimensions ϑ is analogous to $I^{\alpha x}$, $\dot{\vartheta}_j$ is analogous to $-I^{\alpha x}\partial\alpha_j/\partial t$, and A_{jk} is analogous to $I^{\alpha x}\partial\alpha_j/\partial x_k$. This interpretation shows the similarity between the finite difference definitions in equation (6.11) and the finite volume definitions in equation (6.13).

In the NPHASE analysis [HSR91], the fluxes at the cell interfaces are computed from the values of the state vector on either side of the interface using the approximate one-dimensional Riemann solver developed by Roe [Roe81]. The interfacial flux is computed by multiplying the difference in the state vector across the interface by a flux Jacobian matrix representing the local interface conditions. The eigenvalues of this flux Jacobian matrix are used to determine which characteristic modes are included, thus controlling the direction of spatial differencing. This technique is known as flux difference splitting and results in a first-order accurate spatial differencing scheme. Higher order accuracy is obtained by using a corrective flux, which is limited by a TVD scheme [OC84] to control dispersive errors. This flux differencing scheme is described in §6.4 for the steady and linearized unsteady fluxes.

The NPHASE time differencing is based on the three level Beam-Warming [WB77] representation of the time derivative. Thus, if we let the superscript n refer to the current or nth time level, we can write

$$\bar{\tilde{U}}^{n+1} - \bar{\tilde{U}}^n = \Delta\bar{\tilde{U}}^n = \frac{1}{1+\Psi}\left(\Theta\Delta t^c\frac{\partial(\Delta\bar{\tilde{U}}^n)}{\partial t^c} + \Delta t^c\frac{\partial\bar{\tilde{U}}^n}{\partial t^c} + \Psi\Delta\bar{\tilde{U}}^{n-1}\right), \tag{6.14}$$

where Θ and Ψ are constants that define the relative weighting of the time levels. For example, setting $\Theta = 1$ and $\Psi = 1/2$ results in the second-order accurate, implicit, three

point backward difference scheme currently used in the NPHASE code. The time derivatives on the right hand side of Equation (6.14) are expressed in terms of the residual of the governing equation, as defined by Equation (6.12). Collecting terms and substituting for Θ and Ψ results in

$$\frac{3\Delta\tilde{\mathbf{U}}^n - \Delta\tilde{\mathbf{U}}^{n-1}}{2\Delta t^c} = -\tilde{\mathbf{R}}^{n+1} ,$$ (6.15)

where the differences on the left hand side involve both the state vector and the cell volume. Separating the time dependence of the state vector and the cell volume results in

$$\tilde{\mathbf{U}}^{n+1} - \tilde{\mathbf{U}}^n + \frac{2\Delta t^c}{3\vartheta^{n+1}}\tilde{\mathbf{R}}^{n+1} - \frac{\vartheta^{n-1}}{3\vartheta^{n+1}}\left(\tilde{\mathbf{U}}^n - \tilde{\mathbf{U}}^{n-1}\right) + \frac{\tilde{\mathbf{U}}^n}{\vartheta^{n+1}}\left(\vartheta^{n+1} - \frac{4}{3}\vartheta^n + \frac{\vartheta^{n-1}}{3}\right) = 0 .$$ (6.16)

Equation (6.16) is nonlinear, since $\tilde{\mathbf{R}}^{n+1} = \tilde{\mathbf{R}}^{n+1}(\tilde{\mathbf{U}}^{n+1})$ is a nonlinear function of $\tilde{\mathbf{U}}^{n+1}$. Therefore, it is solved using a Newton iteration procedure in which the residual equation is linearized using flux vector splitting and the flux terms are approximately factored to facilitate the numerical solution of the resulting linear, block-tridiagonal, system of equations. Symmetric Gauss-Seidel sub-iterations (cf. §6.4) are used to reduce the approximate factorization error.

The field equation (6.12) must be solved subject to flow tangency conditions (3.27) and (3.28) at the blade surfaces and the duct walls, and far-field conditions at the inflow and outflow boundaries. The far-field conditions must permit the prescription of external unsteady aerodynamic excitations, and allow unsteady disturbance waves coming from within the solution domain to pass through the inflow and outflow boundaries without reflection.

The flow tangency condition in the original NPHASE analysis was based on characteristic theory, and one phantom cell was used in its numerical implementation. This condition was changed to a two phantom-cell, pressure-symmetry, condition, which lowers the spurious numerical entropy and vorticity that is generated at a blade surface. The current NPHASE, multi-block, nonlinear analysis uses the solution from the previous time step when computing across a block interface, thus introducing a time lag at the periodic block boundaries. In the original NPHASE analysis the computational mesh was stretched in the axial direction to dissipate outgoing waves. As part of the current effort, far-field conditions based on one-dimensional characteristic theory, cf. equation (5.60), and on approximate two-dimensional characteristic theory [Gil90], were implemented. These conditions allow for the prescription of incoming unsteady excitations, but result in reflections of outgoing disturbances, if the latter have significant variation in the circumferential direction. As a result we used the stretched mesh capability for the NPHASE blade vibration calculations reported in §7.

6.3 The Steady and Linearized Unsteady Analyses

The field equations that govern the nonlinear steady and the first-harmonic unsteady flows through a blade row rotating at constant angular velocity Ω have been given in §4, as equations (4.46) and (4.47), respectively. These equations have been written in strong conservation form in which terms that depend upon the blade motion, i.e., upon Ω and/or $\mathbf{R}$ are regarded as source terms. The dependent unsteady flow variables $\mathbf{u}$ and the displacement field $\mathbf{R}$ are assumed to be of $\mathcal{O}(\epsilon)$ and τ is a pseudo time variable. The displacement field

48

must be prescribed throughout the solution domain, i.e., a single, extended, blade-passage region of finite extent in the axial direction. In addition, the steady and linearized unsteady field equations must be solved subject to appropriate conditions at the blade surfaces, the duct walls, the blade-to-blade periodic boundaries, and the inflow and outflow boundaries of the computational domain.

Deforming Grids and the Dual Coordinate Transformation

The equations that describe the steady and linearized unsteady flows have been written in terms of the independent variables $\bar{x}$ and t, where $\bar{x}$ is the reference or steady state position of a moving field point. This description is based on an independent variable transformation suggested by Hall and Clark [HC93a] and by Giles [Gil93]. It allows linearized unsteady flow solutions to be determined on a fixed domain or grid in reference physical space (cf. Figure 4b) without introducing difficult extrapolation terms in the blade surface conditions. The transformation from the instantaneous spatial coordinates, $x(\bar{x}, t)$ to the stationary reference spatial coordinates, $\bar{x}$, contains the information that describes the blade motion and the corresponding grid deformation. The time-dependent locations of the grid points, i.e., $x(\bar{x}, t) = \bar{x} + \mathcal{R}(\bar{x}, t)$, define an elastically deforming grid in physical space (see Figure 4a) which, if $\mathbf{R} \equiv 0$, overlays the fixed undeformed grid (Figure 4b) used for the mean flow solution . The deforming grid moves in physical space in response to the unsteady blade motion; whereas the reference grid is stationary.

Because of the transformation $(\mathbf{x}, t) \rightarrow (\bar{x}, t)$, the geometric terms required to define the spatial discretization are time independent. For a finite volume discretization, this means that the mean cell volume and face areas are used in computing the steady and linearized unsteady flow. For a finite difference discretization, the coordinate transformation from the reference physical coordinates to computational coordinates, i.e., $\bar{x} \rightarrow \alpha$, is independent of time. This dual coordinate transformation, $(\mathbf{x}, t) \rightarrow (\bar{x}, t)$ and $\bar{x} \rightarrow \alpha$, results in governing equations for the steady and linearized unsteady flows that are based on the same grid geometry, with source terms, resulting from the grid deformation, appearing in the linearized unsteady equation.

The field (or grid) point displacement $\mathcal{R}(\bar{x}, t) = Re\{\mathbf{R}(\bar{x}) \exp(i\omega t)\}$ must be prescribed. For unsteady flows through vibrating blade rows the vector $\mathcal{R}$ should be defined so that the physical solution domain conforms to the motions of the blades, i.e., a field point on a moving blade surface should have the same $\bar{x}$-coordinate for all time, and this coordinate corresponds to the physical mean or steady state position of the point in the rotating frame of reference. Throughout the remainder of the computational domain, $\mathcal{R}$ can be defined in whatever manner is most convenient for implementing the flow boundary conditions.

The blade motion and, therefore, the deformation field, are harmonic in time, so the instantaneous position x of a field point in physical space is given by

$$x = \bar{x} + Re\{\mathbf{R}(\bar{x}) \exp(i\omega t)\} . \tag{6.17}$$

The deformation field at the grid boundaries is defined in a manner that facilitates implementation of the flow boundary conditions. At the blade surfaces, $\bar{x} \in B_n$, we set

$$\mathbf{R}(\bar{x}) \equiv \mathbf{R}_{B_n}(\bar{x}), \tag{6.18}$$

49

and, since the duct walls are rigid, we set

$$\mathbf{R}(\bar{\mathbf{x}}) \equiv \mathbf{0}, \quad \text{at} \quad \bar{r} = r_H, r_D .$$

(6.19)

As a convenience in imposing the inflow and outflow boundary conditions, the deformation field is assumed to vanish at the far field boundaries, i.e.,

$$\mathbf{R}(\bar{\mathbf{x}}) \equiv \mathbf{0} \quad \text{for} \quad \bar{\xi} \gtrless \bar{\xi}_{\mp} ,$$

(6.20)

where $\bar{\xi}_-$ and $\bar{\xi}_+$ are the axial coordinates of planes parallel to the blade row that form the inflow and outflow boundaries of the computational domain. Also, as a convenience in imposing the phase-lagged, periodic, boundary conditions, the deformation field $\mathbf{R}(\bar{\mathbf{x}})$ is assumed to satisfy the condition

$$\mathbf{R}(\bar{r}, \bar{\theta} + 2\pi/N, \bar{\xi}) \equiv \mathbf{R}(\bar{r}, \bar{\theta}, \bar{\xi}) \exp(in\sigma)$$

(6.21)

The displacement or deformation field in the interior of the computational domain can be chosen arbitrarily, and is defined here by solving Laplace's equation to obtain the smoothest possible distribution within the field and to place the maximum displacements on the boundaries. Thus to prescribe the deformation field $\mathbf{R}(\bar{\mathbf{x}})$ we require a solution of the equation

$$\nabla_{\bar{\mathbf{x}}}^2 \mathbf{R} = \mathbf{0}$$

(6.22)

over a single, extended, blade-passage region, subject to the Dirichlet boundary conditions (6.18)–(6.20) and the phase-lagged periodicity condition (6.21).

Finite Difference Approximation

To write the steady and linearized unsteady equations in terms of computational coordinates we employ a time-independent, spatial coordinate transformation, $\bar{\mathbf{x}} \to \boldsymbol{\alpha}$, from reference physical space to computational space. Because the unsteady grid deformation was absorbed into the definition of the $\mathbf{x} \Leftrightarrow \bar{\mathbf{x}}$ transformation, there is no unsteadiness in the $\bar{\mathbf{x}} \Leftrightarrow \boldsymbol{\alpha}$ transformation. Also, the pseudo time variable τ is defined to be the same in all coordinate systems. The steady (4.46) and first-harmonic unsteady (4.47) equations can be written in terms of the computational coordinates by applying the chain rule for the stationary $\bar{\mathbf{x}} \to \boldsymbol{\alpha}$ transformation, i.e.,

$$\frac{\partial}{\partial \bar{x}_k} = \frac{\partial \alpha_j}{\partial \bar{x}_k} \frac{\partial}{\partial \alpha_j} ,$$

(6.23)

and manipulating the resulting expressions into strong conservation form by using the tensor identity

$$\frac{\partial}{\partial \alpha_j} \left(I^{\alpha\bar{x}} \frac{\partial \alpha_j}{\partial \bar{x}_k} \right) \equiv 0 .$$

(6.24)

where $I^{\alpha\bar{x}}$ is the Jacobian of the inverse transformation $\boldsymbol{\alpha} \to \bar{\mathbf{x}}$.

After performing the required algebra we find that the zeroth-order or mean flow equation becomes

$$\frac{\partial \bar{\mathbf{U}}}{\partial \tau} \bigg|_{\boldsymbol{\alpha}} + \frac{\partial \bar{\mathbf{F}}_j}{\partial \alpha_j} = \bar{\mathbf{S}} ,$$

(6.25)

50

where

$$\bar{\mathbf{U}} = I^{\alpha\bar{x}}\mathbf{U} , \quad \bar{\mathbf{F}}_j = I^{\alpha\bar{x}}\frac{\partial\alpha_j}{\partial\bar{x}_k}\mathbf{F}_k \quad \text{and} \quad \bar{\mathbf{S}} = I^{\alpha\bar{x}}\mathbf{S} . \tag{6.26}$$

The perturbation equation is

$$\frac{\partial\bar{\mathbf{u}}}{\partial\tau}\bigg|_{\boldsymbol{\alpha}} + i\omega\bar{\mathbf{u}} + \frac{\partial\bar{\mathbf{f}}_j}{\partial\alpha_j} - \frac{\partial\mathbf{S}}{\partial\mathbf{U}}\bar{\mathbf{u}} = -\frac{\partial\bar{\mathbf{f}}_j^d}{\partial\alpha_j}$$

$$+ I^{\alpha\bar{x}}[-i\omega(\boldsymbol{\nabla}_{\bar{\mathbf{x}}}\cdot\mathbf{R})\mathbf{U} + (\boldsymbol{\nabla}_{\bar{\mathbf{x}}}\cdot\mathbf{R})\mathbf{S} + (\mathbf{R}\cdot\boldsymbol{\nabla}_{\bar{\mathbf{x}}})\mathbf{S}] , \tag{6.27}$$

where

$$\bar{\mathbf{u}} = I^{\alpha\bar{x}}\mathbf{u} , \qquad \bar{\mathbf{f}}_j = I^{\alpha\bar{x}}\frac{\partial\alpha_j}{\partial\bar{x}_k}\mathbf{f}_k = I^{\alpha\bar{x}}\frac{\partial\alpha_j}{\partial\bar{x}_k}\frac{\partial\mathbf{F}_k}{\partial\mathbf{U}}\mathbf{u} ,$$

and

$$\tag{6.28}$$

$$\bar{\mathbf{f}}_j^d = I^{\alpha\bar{x}}\frac{\partial\alpha_j}{\partial\bar{x}_k}\left[-i\omega R_{x_k}\mathbf{U} - \frac{\partial R_{x_k}}{\partial\bar{x}_m}\mathbf{F}_m + (\boldsymbol{\nabla}_{\bar{\mathbf{x}}}\cdot\mathbf{R})\mathbf{F}_k\right] .$$

The right hand side of equation (6.27) contains source terms, due to the grid deformation, which depend upon the specified deformation field and the mean flow solution.

Finite Volume Approximation

In order to apply a finite volume discretization, the integral forms of the governing equations for the steady (4.48) and the linearized unsteady (4.49) flows must be written in terms of the cell geometry. For example, in three dimensions the mean cell geometry is defined by $\bar{\vartheta}$, the mean cell volume and $\bar{A}_{jk}$, the mean area of the constant α_j cell face projected in the $\bar{x}_k$ direction. Thus, we can write the finite volume spatial discretization of equation (4.48) as

$$\frac{\partial\bar{\mathbf{U}}}{\partial\tau}\bigg|_{\boldsymbol{\alpha}} = -\delta_j\bar{\mathbf{F}}_j + \bar{\mathbf{S}} = -\bar{\mathbf{R}} \tag{6.29}$$

where

$$\bar{\mathbf{U}} = \bar{\vartheta}\mathbf{U} , \quad \bar{\mathbf{F}}_j = \bar{A}_{jk}\mathbf{F}_k , \quad \text{and} \quad \bar{\mathbf{S}} = \bar{\vartheta}\mathbf{S} \tag{6.30}$$

Here, the vectors $\mathbf{U}$ and $\mathbf{S}$ represent averages of the state and source-term vectors, respectively, over the mean cell volume and $\bar{\mathbf{R}}$ is the residual, which should not be confused with the complex amplitude ($\mathbf{R}$) of the grid-point displacement field. The vector $\bar{\mathbf{F}}_j$ is the flux across a constant α_j face, and the symbol δ_j represents the difference across adjacent cell interfaces, i.e. $\delta_j(\quad) = (\quad)_{j+1/2} - (\quad)_{j-1/2}$. The repeated j index implies summation over all computational coordinate directions, so that the term $\delta_j\bar{\mathbf{F}}_j$ is the net flux through the cell, which is balanced by the source term once the pseudo-time integration converges.

In addition to the metrics $\bar{\vartheta}$ and $\bar{A}_{jk}$, that describe the mean cell geometry, the perturbation equation contains terms that depend upon the displacement $\mathbf{R}$, which must also be interpreted in terms of cell geometry. For example, in three dimensions $\Delta\vartheta \approx \vartheta - \bar{\vartheta}$ is the instantaneous cell dilatation, $\vartheta_j = i\omega\bar{A}_{jk}R_{x_k}$ is the volume swept out by the constant α_j face

51

per unit time, and the $a_{jk} \approx A_{jk} - \bar{A}_{jk}$ are the perturbations in the cell-face area vectors. Thus we can write (4.49) as

$$\frac{\partial \bar{\mathbf{u}}}{\partial \tau}\bigg|_{\alpha} + i\omega \bar{\mathbf{u}} + \delta_j \bar{\mathbf{f}}_j - \frac{\partial \mathbf{S}}{\partial \mathbf{U}} \bar{\mathbf{u}} = -i\omega(\Delta \vartheta)\mathbf{U} - \delta_j \bar{\mathbf{f}}_j^d + (\Delta \vartheta)\mathbf{S} + \bar{\vartheta}(\mathbf{R} \cdot \boldsymbol{\nabla}_{\bar{x}})\mathbf{S} \qquad (6.31)$$

where

$$\bar{\mathbf{u}} = \bar{\vartheta}\mathbf{u} \;, \quad \bar{\mathbf{f}}_j = \bar{A}_{jk}\mathbf{f}_k = \bar{A}_{jk}\frac{\partial \mathbf{F}_k}{\partial \mathbf{U}}\mathbf{u} \;, \text{and} \quad \bar{\mathbf{f}}_j^d = -\vartheta_j \mathbf{U} + a_{jk}\mathbf{F}_k \;. \qquad (6.32)$$

Written in terms of a residual, equation (6.31) becomes

$$\frac{\partial \bar{\mathbf{u}}}{\partial \tau}\bigg|_{\alpha} = -i\omega \bar{\mathbf{u}} - \delta_j \bar{\mathbf{f}}_j + \frac{\partial \mathbf{S}}{\partial \mathbf{U}} \bar{\mathbf{u}} - i\omega(\Delta \vartheta)\mathbf{U} - \delta_j \bar{\mathbf{f}}_j^d + (\Delta \vartheta)\mathbf{S} + \bar{\vartheta}(\mathbf{R} \cdot \boldsymbol{\nabla}_{\bar{x}})\mathbf{S} = -\bar{\mathbf{r}} \qquad (6.33)$$

The flux term, $\bar{\mathbf{f}}_j$, on the left hand side of (6.31) is computed using flux difference splitting. The terms on the right hand side of equation (6.31) are grid-deformation, source terms, and are determined by the mean-flow state vector, $\mathbf{U}$, and the deformation field, $\mathbf{R}$.

The pseudo-time differencing is accomplished by setting $\Theta = 1$ and $\Psi = 0$ in equation (6.14), resulting in a first-order accurate, implicit, two point, backward, difference scheme. The pseudo-time difference expressions for the steady and linearized unsteady equations are

$$\frac{\Delta \bar{\mathbf{U}}^n}{\Delta \tau} = \bar{\vartheta}\frac{\mathbf{U}^{n+1} - \mathbf{U}^n}{\Delta \tau} = -\bar{\mathbf{R}}^{n+1} \quad \text{and} \quad \frac{\Delta \bar{\mathbf{u}}^n}{\Delta \tau} = \bar{\vartheta}\frac{\mathbf{u}^{n+1} - \mathbf{u}^n}{\Delta \tau} = -\bar{\mathbf{r}}^{n+1} \;, \qquad (6.34)$$

respectively, where the mean cell volume is independent of the pseudo time. The steady equation is nonlinear because $\bar{\mathbf{R}}^{n+1}$ is a nonlinear function of $\mathbf{U}^{n+1}$. Newton iterations are used to solve this nonlinear equation for the residual in terms of the state vector. The residual equation is linearized using flux vector splitting, and then approximately factored to facilitate the numerical solution of the resulting linear block tridiagonal equations. Symmetric Gauss-Seidel sub-iterations are used to reduce the approximate factorization error. This iteration procedure is described in §6.4.

The steady field equation (6.29) must be solved subject to flow tangency conditions (4.8) at the blade surfaces and duct walls, blade-to-blade periodicity conditions (4.7) and far-field conditions at the inflow and outflow boundaries. Similarly, the unsteady field equation (6.31) must be solved subject to the flow tangency conditions (4.32) and (4.33), the phase-lagged periodicity conditions (4.8) and far-field conditions that allow the prescription of unsteady excitations and the passage of unsteady disturbance waves coming from within the solution domain through the inflow and outflow boundaries without reflection.

The flow tangency condition, now used in the NPHASE analysis, is based on characteristic theory, and a two-phantom-cell, pressure-symmetry implementation, which lowers the spurious numerical entropy and vorticity generated at the blade surfaces. The steady far-field conditions are based on one-dimensional characteristic theory, whereas the unsteady far-field conditions are based on the analytic two-dimensional, single-frequency conditions described in §5.3 and 5.4.

52

6.4 Discretization Scheme

In the nonlinear unsteady analyses of [WJS88] and [HSR91] a cell-centered finite-volume method is used to spatially discretize the governing equations. The residuals due to net fluxes at the cell interfaces are obtained by flux-difference splitting, obtaining an approximate Riemann solution with Roe averaged variables [Roe81]. A corrective flux is used to obtain higher order spatial accuracy. This particular numerical approach offers the ability to capture discontinuities within a few mesh points without producing spurious non-physical oscillations.

Evaluation of Steady and Linearized Unsteady Flux Terms

The flux vectors associated with changes in the steady and unsteady state variables, i.e., $\bar{\mathbf{F}}_j$ and $\bar{\mathbf{f}}_j$ in equations (6.29) and (6.31), respectively, are evaluated using a flux splitting procedure, which is based on fluxes normal to the cell faces. The inviscid flux vectors, $\mathbf{F}_k$, are homogeneous in $\mathbf{U}$ of degree one, i.e., $\mathbf{F}_k = (\partial \mathbf{F}_k / \partial \mathbf{U})\mathbf{U}$. Thus, in computational space, the flux vectors for the steady and first-harmonic unsteady flows [cf. (6.30) and (6.29)] can be written as

$$\bar{\mathbf{F}}_j = \bar{A}_{jk}\mathbf{F}_k = \bar{A}_{jk}\frac{\partial \mathbf{F}_k}{\partial \mathbf{U}}\mathbf{U} = \frac{\partial \bar{\mathbf{F}}_j}{\partial \mathbf{U}}\mathbf{U} \; , \tag{6.35}$$

and

$$\bar{\mathbf{f}}_j = \bar{A}_{jk}\mathbf{f}_k = \bar{A}_{jk}\frac{\partial \mathbf{F}_k}{\partial \mathbf{U}}\mathbf{u} = \frac{\partial \bar{\mathbf{F}}_j}{\partial \mathbf{U}}\mathbf{u} \; , \tag{6.36}$$

so the functional relations $\bar{\mathbf{F}}_j(\mathbf{U})$ and $\bar{\mathbf{f}}_j(\mathbf{u})$ are identical. Equations (6.35) and (6.36) relate the transformed flux vectors $\bar{\mathbf{F}}_j$ and $\bar{\mathbf{f}}_j$ to the cell face geometries, $\bar{A}_{jk}$, and the dependent-variable state vectors, $\mathbf{U}$ and $\mathbf{u}$, in reference physical space. Both the steady and unsteady fluxes are computed by using flux difference splitting to solve an approximate Riemann problem, as outlined below.

The flux splitting is based on a similarity transformation of the computational flux Jacobian matrix $\partial \bar{\mathbf{F}}_j / \partial \mathbf{U}$. We set

$$\frac{\partial \bar{\mathbf{F}}_j}{\partial \mathbf{U}} = (\mathbf{T}\Lambda\mathbf{T}^{-1})_j \tag{6.37}$$

where $\mathbf{T}$ is the matrix of right eigenvectors, Λ is the diagonal matrix of eigenvalues, and $\mathbf{T}^{-1}$ is the matrix of left eigenvectors, of the flux Jacobian matrix, $\partial \bar{\mathbf{F}}_j / \partial \mathbf{U}$. From equation (6.35) it can be seen that this transformation is determined by the $\bar{A}_{jk}$ and the physical flux Jacobian matrix $(\partial \mathbf{F}_k / \partial \mathbf{U})$. The flux Jacobian matrix is split into the sum of right and left traveling modes, i.e.,

$$\frac{\partial \bar{\mathbf{F}}_j^{\pm}}{\partial \mathbf{U}} = (\mathbf{T}\Lambda^{\pm}\mathbf{T}^{-1})_j \tag{6.38}$$

where Λ^+ and Λ^- are diagonal matrices containing the positive (+) and negative (−) eigenvalues, respectively. Positive eigenvalues correspond to right traveling disturbances and negative eigenvalues correspond to left traveling disturbances. The sign of the wave speed

(i.e., Λ^+ or Λ^-) determines the direction in which spatial differencing is applied. Thus, the flux vectors can split according to

$$\bar{\mathbf{F}}_j = \frac{\partial \bar{\mathbf{F}}_j}{\partial \mathbf{U}} \mathbf{U} = \left(\frac{\partial \bar{\mathbf{F}}_j^+}{\partial \mathbf{U}} + \frac{\partial \bar{\mathbf{F}}_j^-}{\partial \mathbf{U}} \right) \mathbf{U} \qquad (6.39)$$

with the $(+)$ terms using information from the negative coordinate direction and the $(-)$ terms using information from the positive coordinate direction.

A cell-centered finite-volume discretization requires that the fluxes at the cell surfaces be computed in terms of values of the state vector in the cell volumes. One method of determining these fluxes is to solve an approximate Riemann problem. Roe [Roe81] solved this problem by defining a flux Jacobian matrix representing average interface conditions. Let the values of the state vector on opposite sides of a cell interface be denoted by the subscripts L and R, and the value of the flux vector at the interface by the subscript I. An intermediate state vector, $\mathbf{U}_{\text{Roe}}$, based on $\mathbf{U}_L$ and $\mathbf{U}_R$ is defined using the following relations

$$\bar{\rho}_{\text{Roe}} = \sqrt{\bar{\rho}_L \bar{\rho}_R}, \quad \text{and} \quad \mathbf{V}_{\text{Roe}} = \frac{\sqrt{\bar{\rho}_L} \mathbf{V}_L + \sqrt{\bar{\rho}_R} \mathbf{V}_R}{\sqrt{\bar{\rho}_L} + \sqrt{\bar{\rho}_R}}, \quad \text{and} \quad E_{T,\text{Roe}} = \frac{\sqrt{\bar{\rho}_L} E_{T,L} + \sqrt{\bar{\rho}_R} E_{T,R}}{\sqrt{\bar{\rho}_L} + \sqrt{\bar{\rho}_R}}. \qquad (6.40)$$

The flux at the interface is constructed from the flux in the cell on either side of the interface, plus the flux due to waves approaching the interface due to the jump in the state vector across the interface.

We have chosen to evaluate the flux vectors, $\bar{\mathbf{F}}$ and $\bar{\mathbf{f}}$, based on $\mathbf{U} = \mathbf{U}_L$ and the flux Jacobian matrices based on left traveling disturbances. Thus, we set

$$\bar{\mathbf{F}}_I = \bar{\mathbf{F}}(\mathbf{U}_L) + \left(\left. \frac{\partial \bar{\mathbf{F}}}{\partial \mathbf{U}} \right|_{\mathbf{U}=\mathbf{U}_{\text{Roe}}} \right)^- (\mathbf{U}_R - \mathbf{U}_L) , \qquad (6.41)$$

and

$$\bar{\mathbf{f}}_I = \bar{\mathbf{f}}(\mathbf{u}_L) + \left(\left. \frac{\partial \bar{\mathbf{F}}}{\partial \mathbf{U}} \right|_{\mathbf{U}=\mathbf{U}_{\text{Roe}}} \right)^- (\mathbf{u}_R - \mathbf{u}_L) , \qquad (6.42)$$

where the disturbances with negative wave speed have been arbitrarily chosen to construct the fluxes, $\bar{\mathbf{F}}_I$ and $\bar{\mathbf{f}}_I$, at the interface, I. The fluxes could have been constructed from the disturbances at positive wave speeds, or an average of the disturbances traveling at positive and negative wave speeds.

An alternative method of flux splitting is the flux vector splitting proposed by Steger and Warming [SW81]. This method is used in the approximate factorization of the time integration scheme. As in flux difference splitting an eigenvalue decomposition of the flux Jacobian matrix is used to distinguish between left and right traveling disturbances. The interfacial flux is based on values of the state vector on either side of the interface, split according to the sign of the wave speed, i.e.,

$$\bar{\mathbf{F}}_I = \left(\left. \frac{\partial \bar{\mathbf{F}}}{\partial \mathbf{U}} \right|_{\mathbf{U}=\mathbf{U}_L} \right)^+ \mathbf{U}_L + \left(\left. \frac{\partial \bar{\mathbf{F}}}{\partial \mathbf{U}} \right|_{\mathbf{U}=\mathbf{U}_R} \right)^- \mathbf{U}_R \qquad (6.43)$$

This flux formulation, as written, results in a first order spatially accurate scheme, but it is only used in the approximate factorization, and does not appear in the converged solution.

54

Once the fluxes have been computed, they are spatially differenced to compute the net flux through the control volume. The difference expression is

$$\delta_j \bar{\mathbf{F}}_j = \sum_j \left[\bar{\mathbf{F}}_j \big|_{j+\frac{1}{2}} - \bar{\mathbf{F}}_j \big|_{j-\frac{1}{2}} \right] \qquad (6.44)$$

where j corresponds to the computational coordinate direction, and fractional grid indices indicate cell interfaces. This difference approximation is first-order accurate if the flux is based only on information from adjacent cells, but higher order spatial accuracy can be achieved by adding a corrective flux. The corrective flux brings in information from additional neighboring cells, but requires the use of a flux limiter to control dispersive errors. Various flux limiting schemes exist, and the choice between them is not clear. The NPHASE code currently supports min-mod [OC84], Superbee [Roe85], and Van Leer flux limiters [VL74], with Van Leer being preferred.

In the present implementation flux limiters are used in the steady analysis, but not in the linearized unsteady analysis. The limiters used in the steady analysis are activated by changes of sign in the jumps in characteristic variables at adjacent interfaces, such as occur at shocks and at stagnation points. The corrected steady flux is given by

$$\bar{\mathbf{F}}_j \big|_{j+\frac{1}{2}} = \bar{\mathbf{F}}_j(\mathbf{U}_j) + \left(\frac{\partial \bar{\mathbf{F}}}{\partial \mathbf{U}} \bigg|_{\mathbf{U}=\mathbf{U}_{\text{Roe}}} \right)^{-} (\mathbf{U}_{j+1} - \mathbf{U}_j) + \frac{1}{2}\mathbf{T}[\boldsymbol{\sigma}^+ - \boldsymbol{\sigma}^-] , \qquad (6.45)$$

where the limited jumps in the characteristic variables are

$$\boldsymbol{\sigma}^+ = \mathbf{L}(\boldsymbol{\sigma}^+_{j-\frac{1}{2}}, \boldsymbol{\sigma}^+_{j+\frac{1}{2}}) \quad \text{and} \quad \boldsymbol{\sigma}^- = \mathbf{L}(\boldsymbol{\sigma}^-_{j+\frac{1}{2}}, \boldsymbol{\sigma}^-_{j+\frac{3}{2}})] , \qquad (6.46)$$

and the jumps in the characteristic variables at the $j - \frac{m}{2}$ cell interface are given by

$$\boldsymbol{\sigma}^{\pm}_{j-\frac{m}{2}} = \Lambda^{\pm} \mathbf{T}^{-1} \left(\mathbf{U}_{j-\frac{m}{2}+\frac{1}{2}} - \mathbf{U}_{j-\frac{m}{2}-\frac{1}{2}} \right) \qquad (6.47)$$

The matrices $\mathbf{T}$ and Λ in (6.47) are computed based on Roe averaged variables, and the function $\mathbf{L}$ in (6.46) is a generic limiting function. For example, the Van Leer limiter can be expressed as

$$L^n(\boldsymbol{\sigma}_1, \boldsymbol{\sigma}_2) = \frac{\sigma_1^n \sigma_2^n + |\sigma_1^n \sigma_2^n|}{\sigma_1^n + \sigma_2^n} , \qquad (6.48)$$

where the superscript n refers to the nth component of the column vector.

No flux limiter is used for the perturbation fluxes, so the corrective flux is comprised of left traveling waves at the upstream interface of the adjacent upstream cell and right traveling waves at the downstream interface of the adjacent downstream cell. These waves at adjacent cell interfaces are approximated using the Roe averaged matrix at the current interface. Thus, the corrected perturbation flux is given by

$$
\begin{aligned}
\bar{\mathbf{f}}_j \big|_{j+\frac{1}{2}} &= \bar{\mathbf{f}}(\mathbf{u}_j) + \left(\frac{\partial \bar{\mathbf{F}}}{\partial \mathbf{U}} \bigg|_{\mathbf{U}=\mathbf{U}_{\text{Roe}}} \right)^{-} (\mathbf{u}_{j+1} - \mathbf{u}_j) \\
&\quad + \frac{1}{2} \left[\left(\frac{\partial \bar{\mathbf{F}}}{\partial \mathbf{U}} \bigg|_{\mathbf{U}=\mathbf{U}_{\text{Roe}}} \right)^{+} (\mathbf{u}_j - \mathbf{u}_{j-1}) - \left(\frac{\partial \bar{\mathbf{F}}}{\partial \mathbf{U}} \bigg|_{\mathbf{U}=\mathbf{U}_{\text{Roe}}} \right)^{-} (\mathbf{u}_{j+2} - \mathbf{u}_{j+1}) \right]
\end{aligned}
\qquad (6.49)
$$

This expression results in second order spatial accuracy.

Evaluation of Grid Deformation Source Terms

In the linearized unsteady analysis source terms arise from the grid deformation because the governing equations are expressed in reference physical coordinates. These source terms are due to changes in cell volume, cell face areas, and cell radial location. The volume source term is given by $-i\omega(\Delta\vartheta)\mathbf{U} + (\Delta\vartheta)\mathbf{S}$, where $\Delta\vartheta$ represents the first order, in $\mathbf{R}$, perturbation in cell volume, as determined by equation (6.6). The cell, face-area, source term, $\bar{\mathbf{f}}_j^d$, accounts for the mean flux through the moving cell faces, and is defined in equation (6.32). The perturbations in projected face area, a_{jk}, are computed using first order expansions in $\mathbf{R}$ for the area of a cell face, as defined in equation (6.4). The swept volume is given by $\dot{\vartheta}_j = i\omega\bar{A}_{jk}R_{x_k}$, where the displacement $\mathbf{R}$ is taken to be the average over a cell face. The remaining grid deformation source term [cf. (4.38)] accounts for changes in radial location. In finite volume form this term is $\bar{\vartheta}(\mathbf{R} \cdot \boldsymbol{\nabla}_{\bar{x}})\mathbf{S}$ where $\mathbf{R}$ is based on the average displacement of the cell vertices.

Pseudo-Time Integration

Solutions to the nonlinear steady and linearized unsteady flow problems are obtained by integrating in pseudo time until a converged steady state solutions are determined. The pseudo-time integrations are performed using an implicit, approximately-factored method [VW93]. For the steady analysis, the implicit pseudo-time discretization results in a nonlinear equation that is solved using Newton iteration. For both the steady and linearized unsteady analyses, the approximate factorization error is reduced using Gauss-Seidel sub iterations, as explained below. The implicit time discretization requires evaluations of flux Jacobian matrices. These are calculated analytically based on Steger-Warming flux-vector splitting, as opposed to a more computationally expensive numerical calculation of these matrices, based on Roe-averaged flux-difference splitting. A simplification in the linearized unsteady analysis resulting from the transformation to reference physical coordinates is that cell geometric quantities do not vary with time, even though the computational domain deforms with time in physical space.

The particular time discretization scheme chosen for the nonlinear steady analysis, cf. (6.34), is expressed as

$$\mathbf{L}(\mathbf{U}^{n+1}) = (\mathbf{U}^{n+1} - \mathbf{U}^n)/\bar{\Theta} + \bar{\mathbf{R}}^{n+1} = 0 , \qquad (6.50)$$

where $\mathbf{L}$ is nonlinear in $\mathbf{U}^{n+1}$, since $\bar{\mathbf{R}}^{n+1}$ is a nonlinear function of $\mathbf{U}^{n+1}$, and

$$\bar{\Theta} = \frac{\Delta\tau\Theta}{(1 + \Psi)\vartheta} = \frac{\Delta\tau}{\vartheta} , \qquad (6.51)$$

since the constants $\Theta = 1$ and $\Psi = 0$ were chosen to define the time discretization.

Equation (6.50) is solved using Newton iteration. Let the superscript p denote the Newton iteration index, then the iteration formula is

$$\left(\left.\frac{\partial\mathbf{L}}{\partial\mathbf{U}}\right|_{\mathbf{U}=\mathbf{U}^{p-1}}\right)(\mathbf{U}^p - \mathbf{U}^{p-1}) = -\mathbf{L}(\mathbf{U}^{p-1}) , \qquad (6.52)$$

56

where $U^0 = U^n$ and $\Delta U^p = U^p - U^{p-1}$ is the Newton update to the state vector. Once the Newton iteration converges, $\Delta U^p = 0$ and $U^p = U^{n+1}$. The flux terms on the left hand side of equation (6.52) are computed using flux vector splitting, for convenience in defining the approximate factorization, while the flux terms on the right hand side are evaluated with flux difference splitting, corrected for higher order spatial accuracy.

The Newton iteration matrix in (6.52) is given by

$$\frac{\partial \mathbf{L}}{\partial \mathbf{U}} = \bar{\Theta}^{-1}\mathbf{I} + \frac{\partial \bar{\mathbf{R}}}{\partial \mathbf{U}} , \tag{6.53}$$

where the residual, $\bar{\mathbf{R}}$, is defined in (6.29). The change in the residual due to the Newton update thus depends upon a change in the net flux and a change in the source term. The change in the net flux due to the Newton update is

$$\delta_j \left[\frac{\partial \bar{\mathbf{F}}_j^{p-1}}{\partial \mathbf{U}} \Delta \mathbf{U}^p \right] , \tag{6.54}$$

and is evaluated using flux vector splitting. To apply flux vector splitting, the geometric terms defining $\partial \bar{\mathbf{F}}/\partial \mathbf{U}$ must be evaluated at the proper location. For example, consider the flux crossing the $j - 1/2$ and $j + 1/2$ cell faces, which are the boundaries of the cell in the α_j computational coordinate direction. When evaluating flux Jacobians using flux vector splitting, let the first subscript indicate the cell index and the second subscript indicate the interface index. The flux in the α_j direction as evaluated using (6.54) is

$$\left[\left(\left.\frac{\partial \bar{\mathbf{F}}_j^{p-1}}{\partial \mathbf{U}}\right|_{j,j+1/2} \right)^+ \left(\Delta \mathbf{U}_j^p\right) + \left(\left.\frac{\partial \bar{\mathbf{F}}_j^{p-1}}{\partial \mathbf{U}}\right|_{j+1,j+1/2} \right)^- \left(\Delta \mathbf{U}_{j+1}^p\right) \right]$$
$$- \left[\left(\left.\frac{\partial \bar{\mathbf{F}}_j^{p-1}}{\partial \mathbf{U}}\right|_{j,j-1/2} \right)^- \left(\Delta \mathbf{U}_j^p\right) + \left(\left.\frac{\partial \bar{\mathbf{F}}_j^{p-1}}{\partial \mathbf{U}}\right|_{j-1,j-1/2} \right)^+ \left(\Delta \mathbf{U}_{j-1}^p\right) \right] , \tag{6.55}$$

which is based on the flux vector splitting given in (6.43). The Newton iteration formula is thus

$$\bar{\Theta}^{-1}\Delta \mathbf{U}^p + \delta_j \left[\frac{\partial \bar{\mathbf{F}}_j^{p-1}}{\partial \mathbf{U}} \Delta \mathbf{U}^p \right] - \frac{\partial \bar{\mathbf{S}}^{p-1}}{\partial \mathbf{U}} \Delta \mathbf{U}^p = -\bar{\Theta}^{-1}(\mathbf{U}^{p-1} - \mathbf{U}^n) - \bar{\mathbf{R}}^{p-1} , \tag{6.56}$$

where the repeated j index for the flux term implies summation over all coordinate directions. Once the Newton iteration converges, Equation (6.50) is satisfied.

For the linearized unsteady analysis, the particular time discretization scheme chosen, cf. (6.34), can be expressed in the form

$$\mathbf{L}(\mathbf{u}^{n+1}) = \bar{\Theta}^{-1}(\mathbf{u}^{n+1} - \mathbf{u}^n) + \bar{\mathbf{r}}^{n+1} = \bar{\Theta}^{-1}\Delta \mathbf{u} + \bar{\mathbf{r}}^{n+1} = 0 \tag{6.57}$$

where $\Delta \mathbf{u}$ is the pseudo-time update, and $\mathbf{L}$ is linear, since $\bar{\mathbf{r}}^{n+1}$ is a linear function of $\mathbf{u}^{n+1}$. Equation (6.57) is solved by using a Taylor series expansion in pseudo time for the residual, i.e.,

$$\bar{\mathbf{r}}^{n+1} = \bar{\mathbf{r}}^n + \frac{\partial \bar{\mathbf{r}}}{\partial \mathbf{u}} \left(\mathbf{u}^{n+1} - \mathbf{u}^n\right) + \dots . \tag{6.58}$$

This can be combined with (6.57) to obtain

$$\left(\bar{\Theta}^{-1} \mathbf{I} + \frac{\partial \bar{\mathbf{r}}}{\partial \mathbf{u}} \right) \left(\mathbf{u}^{n+1} - \mathbf{u}^n \right) = -\bar{\mathbf{r}}^n . \tag{6.59}$$

The flux terms on both the left- and right-hand-sides of equation (6.59) are computed using flux difference splitting and the approximations to the flux terms on both sides are corrected for higher order spatial accuracy. This is feasable for the linear problem, since the flux Jacobian matrices are evaluated only once, and it leads to much better convergence rates for linear unsteady solutions.

The residual $\bar{\mathbf{r}}$ in (6.57)–(6.59) is defined in (6.33). The change in the residual due to the pseudo-time update thus depends upon changes in the volume term, the net flux term, and the source term, i.e.,

$$\frac{\partial \bar{\mathbf{r}}}{\partial \mathbf{u}} \Delta \mathbf{u} = i \omega \bar{\vartheta} \Delta \mathbf{u} + \delta_j \left[\frac{\partial \bar{\mathbf{F}}_j}{\partial \mathbf{U}} \Delta \mathbf{u}^n \right] - \frac{\partial \bar{\mathbf{S}}}{\partial \mathbf{U}} \Delta \mathbf{u}^n , \tag{6.60}$$

where the flux term is evaluated using flux difference splitting. The pseudo-time update formula is thus

$$\bar{\Theta}^{-1} \Delta \mathbf{u}^n + i \omega \bar{\vartheta} \Delta \mathbf{u}^n + \delta_j \left[\frac{\partial \bar{\mathbf{F}}_j}{\partial \mathbf{U}} \Delta \mathbf{u}^n \right] - \frac{\partial \bar{\mathbf{S}}}{\partial \mathbf{U}} \Delta \mathbf{u}^n = -\mathbf{r}^n \tag{6.61}$$

where the repeated j index implies summation over all coordinate directions. Since the unsteady problem is linear, Newton iterations are not required. However, the current LINFLUX implementation uses explicit boundary conditions, which are incorporated into a Newton-like iteration procedure, so that the boundary conditions can be treated in a semi-implicit manner.

The coupling between adjacent cells introduced by the flux terms makes equations (6.56) and (6.61) expensive to evaluate, so the flux evaluation is approximately factored into the product of a positive and negative operator. In order to reduce the error introduced by the approximate factorization, Gauss-Seidel sub-iterations [WT91] are used as part of the time stepping procedure. The approximate factorization equation for the Newton iteration procedure used in the nonlinear steady analysis is

$$\left(\bar{\Theta}^{-1} \mathbf{I} + \frac{\partial \bar{\mathbf{R}}}{\partial \mathbf{U}} \right) \Delta \mathbf{U}^p \approx \mathbf{D}_j \Delta \mathbf{U}_j^p - \mathbf{M}_{j-1}^+ \Delta \mathbf{U}_{j-1}^p + \mathbf{M}_{j+1}^- \Delta \mathbf{U}_{j+1}^p = -\bar{\Theta}^{-1} (\mathbf{U}^{p-1} - \mathbf{U}^n) - \bar{\mathbf{R}}^{p-1} , \tag{6.62}$$

and the approximate factorization equation used for the pseudo-time stepping in the linearized unsteady analysis is

$$\left(\bar{\Theta}^{-1} \mathbf{I} + \frac{\partial \bar{\mathbf{r}}}{\partial \mathbf{u}} \right) \Delta \mathbf{u}^n \approx \mathbf{D}_j \Delta \mathbf{u}_j^n - \mathbf{M}_{j-1}^+ \Delta \mathbf{u}_{j-1}^n + \mathbf{M}_{j+1}^- \Delta \mathbf{u}_{j+1}^n = -\bar{\mathbf{r}}^n . \tag{6.63}$$

In both equations the j subscript is the grid index corresponding to the α_j computational coordinate direction and, in the steady equation, p is the Newton iteration index. For the Newton iteration procedure, the $\mathbf{D}$ and $\mathbf{M}$ matrices are evaluated based on the state vector

58

$\mathbf{U}^{p-1}$ at the previous Newton iteration. The $\mathbf{D}$ matrix represents the diagonal elements of the iteration matrix. The $\mathbf{M}^+$ and $\mathbf{M}^-$ matrices represent the off-diagonal elements of the iteration matrix in the negative and positive computational coordinate directions, respectively.

Introducing l as the Gauss-Seidel iteration index the sub-iteration formula is given by

$$\mathbf{D}_j \Delta \mathbf{U}_j^{p,l} - \mathbf{M}_{j-1}^+ \Delta \mathbf{U}_{j-1}^{p,l} + \mathbf{M}_{j+1}^- \Delta \mathbf{U}_{j+1}^{p,l-1} = -\mathbf{L}^{p-1}$$

$$\mathbf{D}_j \Delta \mathbf{U}_j^{p,l+1} + \mathbf{M}_{j+1}^- \Delta \mathbf{U}_{j+1}^{p,l+1} - \mathbf{M}_{j-1}^+ \Delta \mathbf{U}_{j-1}^{p,l} = -\mathbf{L}^{p-1} \qquad (6.64)$$

$$\Delta \mathbf{U}^{p,l+2} = \Delta \mathbf{U}^{p,l+1} - \Delta \mathbf{U}^{p,l}$$

The first sub-iteration is over positive grid indices and the second sub-iteration is over negative grid indices. The sub-iteration procedure is thus an LU decomposition of the Newton iteration or pseudo-time matrix, with forward and backward substitution. Once the Gauss-Seidel sub-iteration converges, equation (6.56) or (6.61) is satisfied.

Once the solutions converge to a steady state, any error introduced by the Newton iteration or the approximate factorization vanishes. Only the error in the residual calculation of equation (6.29) or equation (6.33) remains. These residuals are calculated using flux difference splitting with a corrective flux, as given by (6.45) and (6.49), to obtain second order spatial accuracy.

7. Numerical Results

Unsteady aerodynamic response predictions will be presented for two-dimensional flows through a compressor-type ($M_{+\infty} < M_{-\infty}$) cascade undergoing prescribed blade motions and subjected to various incident aerodynamic excitations to demonstrate the current capabilities of the linearized Euler analysis and code, LINFLUX. The cascade, known as the Tenth Standard Configuration [FS83, FV93] is assumed to be operating at subsonic uniform inlet and exit conditions. We will consider unsteady flows excited by prescribed blade motions for the Tenth Standard Cascade operating at an inlet Mach number $M_{-\infty}$ and flow angle, $\Omega_{-\infty}$, of 0.7 and 55 deg respectively, and at an inlet Mach number and flow angle of 0.8 and 58 deg. In the first case the steady background flow is entirely subsonic; in the second, it is transonic with a normal shock emanating from the suction surface of each blade. For the unsteady flows excited by external aerodynamic excitations, the Tenth Standard Cascade is operating at $M_{-\infty} = 0.5$ and $\Omega_{-\infty} = 55$ deg, and the steady background flow is entirely subsonic.

In addition to the LINFLUX results for the Tenth Standard Cascade, for purposes of comparison, we will also present nonlinear unsteady aerodynamic response predictions for the flows excited by blade vibrations, as determined using the NPHASE code [HSR91], and linear response predictions for blade vibrations and external aerodynamic excitations, as determined using the LINFLO analysis [Ver92, Ver93]. In the latter, the unsteady flow is regarded as a small perturbation of a potential steady background flow. The steady version of the NPHASE analysis is used to provide the steady background flow information for the LINFLUX calculations; the full-potential analysis CASPOF [Cas83] is used to provide this information for the LINFLO calculations. Because appropriate unsteady far field conditions have not yet been incorporated, at present, the NPHASE analysis cannot be applied to predict unsteady flows excited by external aerodynamic excitations.

7.1 Flow Configuration and Computational Meshes

The Tenth Standard Cascade has a stagger angle, Θ, of 45 deg and a gap/chord ratio, G, of unity (see Figure 2). The blades are constructed by superposing the thickness distribution of a modified NACA four-digit series airfoil on a circular-arc camber line. The thickness distribution is given by

$$T(x) = H_T[2.969x^{1/2} - 1.26x - 3.516x^2 + 2.843x^3 - 1.036x^4], \qquad 0 \leq x \leq 1 . \qquad (7.1)$$

where H_T is the nominal blade thickness. The coefficient of the x^4 term in (7.1) differs from that used in the standard NACA definition (i.e., -1.015) so that the blades close at $x = 1$ in wedge-shaped trailing edges. The camber distribution is given by

$$C(x) = H_C - R + [R^2 - (x - 0.5)^2]^{1/2} , \qquad 0 \leq x \leq 1 , \qquad (7.2)$$

where H_C (> 0) is the height of the camberline at mid-chord and $R = (2H_C)^{-1}(H_C^2 + 0.25)$ is the radius of the circular-arc camber line. Thus, the surface coordinates for the reference ($n = 0$) blade are given by

$$[x, y]_{B,\pm} = [x \mp 0.5T(x)\sin\theta, \ C(x) \pm 0.5T(x)\cos\theta] , \qquad 0 \leq x \leq 1 , \qquad (7.3)$$

where $\theta = \tan^{-1}(dC/dx)$. The Tenth Standard Cascade is defined by setting $H_T = 0.06$ and $H_C = 0.05$, and is, therefore, a cascade of modified NACA 5506 airfoils.

Steady and linearized unsteady solutions were determined, using NPHASE and LIN-FLUX, respectively, on H-type meshes. The meshes used in the blade vibration and acoustic excitation studies are shown in Figure 5. These meshes consist of 155 axial lines and 41 lines in the blade-to-blade direction, and extend one axial chord upstream and downstream from the blade row. For the subsonic calculations (Figure 5a) the average normal grid spacing adjacent to a blade was 0.1% of chord, and 55 points were placed on the blade surfaces. For the transonic calculations (Figure 5b) the average normal grid spacing adjacent to a blade was 0.05% of chord, and 75 points were placed on the blade surfaces. A finer H-mesh, i.e., 241×81, with a smoother variation in grid distribution, was needed for the entropic and vortical gust calculations. Nonlinear, unsteady, aerodynamic solutions were also determined using the NPHASE analysis. The nonlinear unsteady subsonic and transonic solutions were determined on 121×41 and 241×81 H-meshes respectively. Since NPHASE does not have fully nonreflecting, unsteady, far-field conditions, the H-meshes were stretched with increasing axial distance from the blade row and extended to five axial chords upstream and downstream from the blade row to dissipate outgoing waves.

The full potential steady (CASPOF) and the linearized unsteady (LINFLO) solutions were determined on composite meshes [Cas83, UV91] consisting of local C-meshes embedded in global H-meshes. The C-meshes are used to accurately resolve the steady and unsteady flows around blade leading edges and through normal shocks, and to permit shock fitting in LINFLO calculations. The H- and C-meshes used in the LINFLO calculations consisted of 155 axial and 41 tangential lines and 101 radial and 11 circumferential lines, respectively. Coarser H- and C-meshes were used in the CASPOF calculations. In both cases, the H-mesh extended one axial chord upstream and downstream from the blade row and, for transonic flows, radial mesh lines were concentrated near shocks.

The computing times, reported herein, pertain to calculations performed on an IBM-370 Workstation. Converged, NPHASE, steady inviscid solutions were obtained after 1,000 pseudo-time iterations. The steady subsonic solutions on a 121×41 mesh required approximately 18 CPU minutes to converge; the steady transonic solutions (241×81 mesh), approximately 75 CPU minutes. The LINFLUX calculations for unsteady subsonic flows excited by blade vibrations or acoustic excitations were performed on a 155×41 H-mesh and required about 5 CPU minutes to converge. Those for transonic flows excited by blade vibrations, also performed on a 155×41 mesh, required approximately 20 CPU minutes. The calculations for unsteady subsonic flows driven by an entropic or vortical gust, which were performed on a 241 by 81 mesh, also required about 20 CPU minutes to converge

The NPHASE nonlinear unsteady calculations were started from the appropriate steady solution, and performed using 1,000 time-steps per cycle of blade motion with 3 Newton iterations per time step and 3 symmetric Gauss-Siedel iterations per Newton iteration. Four cycles of motion were used to converge the nonlinear inviscid solutions to a periodic state. The subsonic inviscid unsteady calculations were performed on a 121×41 H-mesh and required about 40 CPU min per blade passage to converge, and converged transonic inviscid solutions, performed on a 241×81 H-mesh, required approximately 180 CPU min/blade passage. The number of blade passages required for a nonlinear unsteady calculation depends upon the interblade phase angle of the unsteady excitation. For example, if $\sigma = 60$ deg, six

61

passages are needed. Steady full potential solutions were obtained, using CASPOF, within 10 CPU seconds, and LINFLO, linearized, inviscid solutions required about 90 CPU seconds per unsteady case.

7.2 Blade Vibration

First, we consider unsteady flows excited by prescribed single-degree-of-freedom, harmonic, blade motions at small amplitude. The motions considered are pure translations normal to the blade chords (bending) and pure rotations (torsion) about axes at the blade midchords. Blade motions are termed subresonant, if all acoustic response disturbances attenuate with increasing axial distance from the blade row; superresonant (m, n), if m and n such disturbances persist in the far upstream and far downstream regions, respectively, and carry energy away from the blade row; and resonant, if at least one acoustic response disturbance persists in either the far upstream or far downstream regions and carries energy along the blade row [Ver89b].

For the subsonic cascade configuration with $M_{-\infty} = 0.7$ and $\Omega_{-\infty} = 55$ deg and exit flow conditions, as determined by a full-potential calculation, of $M_{-\infty} = 0.446$ and $\Omega_{-\infty} = 40.2$ deg, the resonant interblade phase angles (in degrees) are $\sigma_{-\infty}^{-} = -26.93\omega$, $\sigma_{-\infty}^{+} = 117.12\omega$, $\sigma_{+\infty}^{-} = -31.80\omega$ and $\sigma_{+\infty}^{+} = 59.79\omega$. The subscripts refer to the far upstream $(-\infty)$ or far downstream $(+\infty)$ regions and the superscripts indicate that there are two resonant interblade phase angles associated with each of these regions. For the transonic configuration with $M_{-\infty} = 0.8$, $\Omega_{-\infty} = 58$ deg, $M_{+\infty} = 0.432$ and $\Omega_{+\infty} = 40.3$ deg, the resonant phase angles are $\sigma_{-\infty}^{-} = -28.94\omega$, $\sigma_{-\infty}^{+} = 201.7\omega$, $\sigma_{+\infty}^{-} = -35.92\omega$ and $\sigma_{+\infty}^{+} = 66.22\omega$. In both cases the blade motions at interblade phase angles lying between the lowest $(\sigma_{+\infty}^{-})$ and highest $(\sigma_{-\infty}^{+})$ resonant interblade phase angles are superresonant.

Subsonic Flow ($M_{-\infty} = 0.7, \Omega_{-\infty} = 55$ deg)

The steady Mach number contours and blade-surface Mach number distributions for the subsonic operating condition ($M_{-\infty} = 0.7, \Omega = 55$ deg) as determined by the nonlinear Euler analysis are shown in Figure 6, along with the surface Mach number distributions predicted using the CASPOF analysis. The Euler analysis predicts a mean flow exit Mach number, $M_{+\infty}$, and flow angle, $\Omega_{+\infty}$, of 0.450 and 39.8 deg, respectively, and introduces spurious total pressure losses of approximately 1.5% and 0.01% on the suction and pressure surfaces, respectively, of each blade. The potential analysis predicts a mean flow exit Mach number and flow angle of 0.446 and 40.2 deg, respectively.

Unsteady response predictions for this subsonic NACA 5506 cascade are shown in Figures 7 through 10. Contours of the out-of-phase (with blade displacement) component of the unsteady pressure, i.e., $Im\{p\}$, as predicted using the LINFLO and LINFLUX analyses, for an out-of-phase ($\sigma = 180$ deg) torsional blade vibration at unit frequency are shown in Figure 7. The results of the two linearized analyses are seen to be in very good agreement for this subresonant blade motion.

Pressure displacement function distributions (w_C) and work per cycle (W_C) predictions [Ver89a, Ver93] for in-phase ($\sigma = 0$ deg) and out-of-phase torsional blade vibrations are shown in Figure 8. The results of the nonlinear Euler analysis NPHASE, the linearized Euler

analysis LINFLUX, and the linearized potential analysis LINFLO are seen to be in excellent agreement for the superresonant (1,1), in-phase vibration, and in excellent agreement along the pressure surface for the subresonant, out-of-phase vibration. However, differences exist along the blade suction surface between the results of the two Euler analyses and those of the potential analysis, for the out-of-phase motion.

The blade motions considered in Figure 8 are both stable, i.e., $W_C < 0$. The pressure displacement function curves for the in-phase torsional motion reveal that the local unsteady loads over most of the blade surface tend to suppress this motion, but those along the suction surface from approximately 15% to approximately 45% of chord support the motion. For the out-of-phase torsional motion, the pressure displacement function curves reveal that the local unsteady loads over the entire suction surface and most of the pressure surface tend to suppress the in-phase torsional motion, especially those in the vicinity of the blade leading edge.

Similar results for bending vibrations are shown in Figure 9. The results of the two linearized analyses for the in-phase bending vibration are in good agreement, whereas those of the nonlinear Euler and the linearized potential analysis are in good agreement for the subresonant, out-of-phase motion. For the latter motion, the results of the two linear analyses show significant differences on the suction surface from a blade leading edge to approximately 20% of blade chord. The two bending vibrations are stable, but the local unsteady loads over the aft part of the suction surface are destabilizing for the in-phase motion.

Numerical results are given in Figure 10 indicating the behavior of the aerodynamic work per cycle versus interblade phase angle for the subsonic NACA 5506 cascade undergoing pure torsional (Figure 10a) and pure bending (Figure 10b) vibrations at unit frequency. The work per cycle predictions are given for an interblade phase angle range from −90 deg to 270 deg. The vertical lines above the curves in Figure 10 indicate the resonant interblade phase angles for a unit-frequency excitation. NPHASE, nonlinear, unsteady results are given for $\sigma = 0$ deg, ± 60 deg, ± 90 deg, 120 deg, 180 deg, 240 deg and 270 deg; LINFLUX results, at 15 deg intervals in interblade phase angle, and a sufficient number of LINFLO results have been determined to essentially define W_C as a continuous function of σ. The results determined using the three analyses are in very good agreement, except for those at $\sigma = 120$ deg, which is near the upstream resonance condition $\sigma = \sigma_{-\infty}^+ = 117.12$ deg. Note that resonance phenomena are not accurately modeled by the current version of the nonlinear analysis, because this analysis is applied on a stretched mesh with coarse axial spacings in the far field.

The work per cycle results in Figure 10 indicate that the single-degree-of-freedom torsional and bending blade motions at unit frequency are stable $(W_C < 0)$ and that the torsional vibrations have the lower stability margin. They also indicate the rather complicated nature of the global unsteady aerodynamic response, which is associated with the different acoustic responses (i.e., subresonant, superresonant (1,0), etc.) that occur at different interblade phase angles. Note the abrupt changes in the global unsteady aerodynamic response behaviors, as predicted by the linearized analyses, at the interblade phase angles at which acoustic resonance occurs.

In general, the results of the three analyses, LINFLUX, NPHASE and LINFLO, for the subsonic unsteady flows considered in Figures 8 through 10, are in good agreement. Differences exist, however, and the reasons for these are not clearly understood at the present

time. One possible cause is that different meshes, i.e., an H-mesh, a stretched H-mesh and a composite H/C-mesh, respectively, are used in the three analyses. Another, is the different methods used to model unsteady disturbances in the far-field. Analytic, non-reflecting, far-field conditions are applied in the two linearized calculations, whereas an axially stretched mesh is used in the nonlinear calculation to dissipate outgoing disturbance waves. In future work, analytic far-field conditions should be incorporated into the NPHASE analysis so that the nonlinear and linearized Euler predictions can be determined on the same meshes. Then, if differences between the nonlinear and linear Euler results still persist for small-disturbance, unsteady, subsonic flows, they will indicate that errors have been introduced in deriving the LINFLUX analysis from the nonlinear NPHASE analysis.

Transsonic Flow ($M_{-\infty} = 0.8, \Omega_{-\infty} = 58$ deg)

The steady Mach number contours and blade-surface Mach number distributions, as determined by the nonlinear Euler analysis, NPHASE are shown in Figure 11, along with surface Mach number distributions predicted by the CASPOF analysis. The Euler analysis predicts a mean flow exit Mach number $M_{+\infty}$ and flow angle $\Omega_{+\infty}$ of 0.429 and 39.8 deg, respectively. The Mach numbers at the base of the shock are 1.26 on the upstream side and 0.834 on the downstream side. Spurious total pressure losses of approximately 2.5% on the suction surface and 0.1% on the pressure surface are present in the Euler predictions. The total pressure loss on the suction surface is increased approximately 1.0% by the shock to approximately 3.5% downstream of the shock. The potential flow analysis predicts a mean flow exit Mach number and flow angle of 0.432 and 40.3 deg, respectively. The Mach numbers at the base of the shock are 1.292 and 0.794. The surface Mach numbers predicted by the two analyses are in good agreement, except for those on the suction surface just downstream of the leading edge and in the vicinity of the shock, where small differences exist.

Unsteady aerodynamic response predictions for the transonic NACA 5506 cascade are given in Figures 12 through 15 for blades undergoing pure torsional and pure bending vibrations at unit frequency. Contours of the out-of-phase component of the unsteady pressure response, $Im\{p\}$, as predicted using the LINFLO and LINFLUX analyses, for an in-phase ($\sigma = 0$ deg) torsional blade vibration are shown in Figure 12. The pressure contours predicted by the two analyses for this superresonant (1,1) excitation are in reasonably good agreement, except in the immediate vicinity of the shock. It should be noted that shock fitting is used in the LINFLO analysis leading to discontinuous, first-harmonic, unsteady pressures and impulsive anharmonic pressures that depend on shock displacement. The anharmonic pressures are not depicted in Figure 12. Shocks are captured in both the nonlinear and linearized Euler analyses so that the first-harmonic unsteady pressure responses are continuous, but undergo large changes in the vicinity of a shock.

Pressure-displacement function distributions and work per-cycle predictions for the transonic cascade undergoing in- and out-of-phase torsional blade vibrations at $\omega = 1$ are shown in Figure 13. These superresonant blade motions are stable, and, according to the linearized potential analysis, the impulsive shock loads, indicated by the delta functions in Figures 13, contribute significantly to the stability margins. The shock impulse, predicted by LINFLO, depends upon the product of the steady pressure jump across the shock and the shock displacement. The shock capturing used in the Euler calculations is based on the use of

directionally-dependent flux evaluations. The directional differencing used in the nonlinear unsteady analysis is based on the nonlinear unsteady flow properties, whereas that used in the linear analysis is based upon the underlying steady flow properties. Although the time-accurate, nonlinear analysis predicts a pressure response with a sharply defined shock at each instant of time, shock effects are smeared in the pressure displacement function predictions, because these are based on an integration in time of the local unsteady response over a complete cycle of blade, and therefore shock, motion.

For the torsional motions considered in Figure 13, the results given by the nonlinear Euler analysis, the linearized Euler analysis, and the linearized potential analysis are in good agreement in subsonic regions, i.e., along the blade pressure surface and along the suction surface downstream of the shock. However, the results in the supersonic region upstream of the shock and in the vicinity of the shock show substantial differences, particularly those for the superresonant (1,0), out-of-phase, torsional blade vibration. Differences between the nonlinear and linearized Euler analyses are due in part to the different methods used to prevent disturbance reflections at the inflow and outflow boundaries, i.e, the use of a stretched mesh and the imposition of analytic far-field conditions, respectively, and to the different discrete approximations used in the vicinity of the shock. The differences between the results of the two linearized analyses are due primarily to the different methods (i.e., shock capturing and shock fitting) used in modeling unsteady shock phenomena. The shock capturing method currently used in the linearized Euler analysis is easy to implement, but it does not properly account for shock motion. Therefore, it does not lead to the prediction of a concentrated, anharmonic, pressure load at the shock.

A similar set of results for bending vibrations is shown in Figure 14. These blade motions are also stable, even though the shock impulse, as predicted using LINFLO, is destabilizing for the out-of-phase motion. The results of the three analyses, particularly those of the nonlinear and linearized Euler analyses show significant differences in the vicinity of the shock and, for the in-phase motion, in the vicinity of the blade leading edge. The shock modeling effort in the linearized Euler analysis is continuing with the goals of achieving consistent and good agreement between the nonlinear and linearized Euler predictions in the vicinity of a shock. Also, an effort will be initiated to include analytic far-field conditions in the nonlinear code (NPHASE) so that the nonlinear and linear Euler calculations can be performed on the same mesh. This could eliminate the differences between the nonlinear and linearized Euler solutions at blade leading edges.

Work per cycle versus interblade phase angle predictions are given in Figure 15 for the transonic NACA 5506 cascade undergoing pure torsional and pure bending blade vibrations at unit frequency. The three analyses, NPHASE, LINFLUX and LINFLO, provide results that show similar trends, and indicate that the unit frequency, bending and torsional vibrations of the transonic cascade are stable.

7.3 Aerodynamic Excitation

We proceed to analyze unsteady flows, excited by external aerodynamic disturbances, through the Tenth Standard Cascade operating at $M_{-\infty} = 0.5$ and $\Omega_{-\infty} = 55$ deg. The steady Mach number contours and surface Mach number distributions for the NACA 5506 cascade, as determined by the NPHASE analysis, are shown in Figure 16 along with the

surface Mach number distributions determined using the CASPOF analysis. The nonlinear Euler analyis predicts a mean flow exit Mach number and flow angle of 0.351 and 39.9 deg, respectively. The potential flow analysis predicts a mean flow exit Mach number and flow angle of 0.349 and 40.2 deg, respectively.

Acoustic Excitations

First, we consider unsteady flows excited acoustic disturbances, that carry energy towards the blade row from far upstream $(-\infty)$ or far downstream $(+\infty)$. For subsonic inlet and exit conditions $(M_{\mp\infty} < 1)$ the axial wave number of a propagating acoustic excitation is given by (5.54) with $d_m^2 < 0$, i.e.,

$$\kappa_{\xi,\mp\infty} = i(\mp|d_{\mp\infty}| + M_{\mp\infty}^2 \delta_{\mp\infty} \cos\Omega_{\mp\infty}) . \tag{7.4}$$

The tangential wave number of the disturbance is $\kappa_\eta = \sigma G^{-1}$. Note that for a given temporal frequency, interblade phase angle and mean-flow, operating condition, $|\kappa_{\xi,+\infty}| > |\kappa_{\xi,-\infty}|$, because a disturbance coming from downstream travels against the steady flow direction. This implies that, for the same flow conditions, greater mesh resolution is required to resolve upstream traveling acoustic disturbances.

We will consider acoustic excitations from upstream and downstream at a reduced frequency $\omega = 5$ and interblade phase angle $\sigma = -90$ deg. For the upstream excitation, the wave number magnitude is $|\kappa_{-\infty}| = 1.68$, corresponding to a wavelength of 3.73 blade chords, and the propagation angle of the excitation with respect to the positive axial direction is 69.0 deg. The unsteady pressure fields and surface pressure distributions on the reference blade, as predicted by the linearized Euler analysis and the linearized potential analysis, are presented in Figures 17 and 18. The results of the two analyses are seen to be in excellent agreement.

For the downstream excitation, the wave number magnitude is 2.71, corresponding to a wavelength of 2.32 blade chords, and the excitation propagation angle with respect to the positive axial direction is 144.6 deg. The pressure fields and pressure distributions on the blade as predicted by the linearized Euler analysis and the linearized potential analysis are presented in Figures 19 and 20. The results of the two analyses are again in very good agreement, however the agreement for the downstream excitation is not as good as that for the upstream excitation. The discrepancy may be due to the shorter wavelength of the downstream excitation requiring greater mesh resolution to reduce discretization errors to negligible levels.

Entropic and Vortical Excitations

Small-amplitude entropic and vortical disturbances are convected at the velocity of the steady background flow. A single harmonic component of either one of these disturbances is described by specifying the temporal frequency, ω, interblade phase angle, σ, and the complex amplitude, $s_{-\infty}$ or $\zeta_{-\infty}$ [cf. equations (2.5) and (2.6)]. For a vortical excitation we can prescribe the complex amplitude of the normal component of the rotational velocity, i.e., $\mathbf{v}_{R,-\infty} \cdot \mathbf{e}_N$, where

$$\mathbf{v}_{R,-\infty} = i(\boldsymbol{\kappa}_{-\infty} \times \boldsymbol{\zeta}_{-\infty})/|\boldsymbol{\kappa}_{-\infty}|^2 , \tag{7.5}$$

in lieu of prescribing the vorticity. The component of the gust velocity in the inlet free-stream direction, $\mathbf{v}_{R,-\infty} \cdot \mathbf{e}_T$, is determined by the divergence-free condition, i.e., $i\boldsymbol{\kappa}_{-\infty} \cdot \mathbf{v}_{R,-\infty} \equiv 0$. The wave number $\boldsymbol{\kappa}_{-\infty}$, of a harmonic entropic or vortical excitation has a component $\kappa_{\eta,-\infty} = \sigma G^{-1}$ in the cascade tangential or η-direction and a component $\kappa_T = -\omega V_{-\infty}^{-1} = -\omega$ in the inlet free-stream direction. Therefore,

$$
\begin{aligned}
\boldsymbol{\kappa}_{-\infty} &= -(\omega \sec \Omega_{-\infty} + \sigma G^{-1} \tan \Omega_{-\infty})\mathbf{e}_\xi + \sigma G^{-1}\mathbf{e}_\eta \\
&= -\omega \mathbf{e}_T + (\omega \tan \Omega_{-\infty} + \sigma G^{-1} \sec \Omega_{-\infty})\mathbf{e}_N .
\end{aligned}
\tag{7.6}
$$

To consider a gust that models the first harmonic component, i.e., the component at the blade passing frequency (BPF), of a wake excitation from upstream we would set $\sigma = \kappa_{\eta,-\infty} G = -2\pi G/G_{\text{EXC}}$ and $\omega = -\kappa_{\eta,-\infty} V_{\text{EXC}} = 2\pi V_{\text{EXC}}/G_{\text{EXC}}$. Here G_{EXC} is the blade spacing in the upstream row which moves at constant velocity $V_{\text{EXC}} \mathbf{e}_\eta = V_W \mathbf{e}_\eta$ in the circumferential direction relative to the reference blade row, and $\kappa_{\eta,-\infty} = -2\pi/G_{\text{EXC}}$ is the circumferential wave number of the fundamental or first-harmonic disturbance. In the present study, an interblade phase angle of $\sigma = -180$ deg was chosen to represent the first-harmonic component of a wake excitation from an upstream blade row with one-half the number of blades as in the reference blade row. The temporal frequency was set at $\omega = 5$, which corresponds to an upstream flow coefficient, i.e. ratio of mean flow axial speed to wheel speed, $V_{-\infty} \cos \Omega_{-\infty}/V_W$, of 0.3604. The wave number magnitude, $|\boldsymbol{\kappa}_{-\infty}|$, of this gust excitation is then 5.25, and its direction of travel relative to the axial flow direction, i.e., $\alpha = \tan^{-1}(\kappa_{\eta,-\infty}/\kappa_{\xi,-\infty})$, is 36.5 deg.

Results of the LINFLO and LINFLUX analyses for the convection of entropic [with $s_{-\infty} = (1,0)$] and vortical [with $\mathbf{v}_{R,-\infty} \cdot \mathbf{e}_N = (1,0)$] gusts at BPF, i.e., $\omega = 5$ and $\sigma = -180$ deg, through the NACA 5506 cascade operating at $M_{-\infty} = 0.5$ and $\Omega_{-\infty} = 55$ deg, are given in Figures 21 through 24. It should be noted that the LINFLO predictions for the unsteady entropy and vorticity contours are based on closed form solutions in which these unsteady flow quantities are expressed as explicit functions of the drift and stream functions of the steady background flow (see [Ver93]). The predicted entropy fields for a prescribed entropic excitation at inlet are shown in Figure 21. The two linearized predictions for the in-phase component of the unsteady entropy are in very good agreement. However, the linearized Euler results show spurious distortions in the entropy contours, that are caused by numerical losses, in the vicinities of the blades and along the blade wakes. A spurious production of entropy is also present in the steady background flow predicted with the nonlinear NPHASE analysis, and this is believed to contribute to the distortions in the unsteady entropy contours.

The interaction of vortical gust with the NACA 5506 cascade is depicted in Figures 22 through 24. The predicted vorticity and pressure fields, represented via contour plots of the in-phase components of these flow variables, are shown in Figures 22 and 23, respectively; and the predicted unsteady pressures acting on the surfaces of the reference blade, in Figure 24. The vortical gust predictions in Figure 22 are in good qualitative agreement, but the results of the linearized Euler analysis show severe distortions in the vorticity contours in the vicinity of the blades and their wakes.

The ability to accurately predict the response of real blade cascades to entropic and vortical excitations using LINFLUX is currently impeded by the use of first-order accu-

rate, blade-surface, boundary conditions in both the nonlinear steady and the linearized unsteady Euler analyses. These conditions result in the production of spurious steady and first-harmonic, unsteady entropy and vorticity near blade surfaces. Also, the entropy and vorticity, produced artificially by numerical losses, in the steady background flow are believed to interact with the unsteady entropic and vortical disturbances to further distort the unsteady predictions.

Because of the foregoing limitations, the vorticity contours (Figure 22) predicted by the LINFLUX analysis differ from those predicted by LINFLO. However, this disparity between the predicted vorticity (excitation) fields does not seem to have a strong impact on the resulting unsteady pressure response. The unsteady pressure fields (Figure 23) and surface pressure distributions (Figure 24), predicted by linearized Euler and potential analyses for the vortical gust at $\omega = 5$ and $\sigma = -180$ deg, are in good agreement. Nevertheless, the LINFLUX capabilities for predicting unsteady flows excited by vortical disturbances must be improved to provide a more accurate description of the convection of a vortical gust through a blade row. Also, the present LINFLUX gust solutions are very sensitive to the "smoothness" of the mesh, and they require excessive computing times to converge. These issues should be addressed in future work.

8. Concluding Remarks

Accurate and efficient, three-dimensional, unsteady, fluid-dynamic analyses are needed to enhance our ability to understand and predict the aeroelastic (flutter and forced vibration) and aeroacoustic (noise generation, transmission and reflection) characteristics of turbomachinery blading. Such analyses must account for nonisentropic and rotational inviscid effects to model swirling flows with strong shocks and, eventually, for viscous effects to model separated flows. Motivated by these needs, independent, but coordinated, research programs are being conducted at NASA Lewis Research Center, Mississippi State University and the United Technologies Research Center to develop advanced nonlinear and linearized unsteady aerodynamic analyses for aeroelastic and aeroacoustic design applications. Under the present UTRC program, work has been focused on formulating linearized, inviscid, unsteady aerodynamic and numerical models, based on the Euler equations of fluid motion, for three-dimensional flows through single blade rows operating within cylindrical ducts. These models have been implemented into the two-dimensional, linearized, unsteady, aerodynamic code LINFLUX, and the LINFLUX code has been evaluated via application to benchmark unsteady cascade flows.

In formulating the linearized unsteady aerodynamic model, the unsteady flow is regarded as a small perturbation of a nonlinear background flow that is steady in the blade row frame of reference. This leads to time-independent, nonlinear, governing equations for the steady background flow, and time-independent, linear, variable-coefficient, equations for the first-harmonic, unsteady perturbation. The variable coefficients in the unsteady equations depend upon the steady background flow. This type of linearization accounts for the effects of real blade geometry, mean blade loading, mean swirl and strong shocks and their motions on the unsteady aerodynamic responses to prescribed structural and external aerodynamic excitations.

In the present formulation, both the steady and unsteady equations are expressed in terms of spatial independent variables that describe the reference or steady-state positions of the moving field points that make up the physical solution domain. Thus, both sets of equations are solved on a fixed grid in reference physical space to determine the values of the steady and unsteady flow variables at the mean and instantaneous positions, respectively, of the moving field points. This approach [HC93a, Gil93] in which the time-dependent deformation of the physical domain is represented by source terms in the unsteady field equations, simplifies the imposition of the blade-surface or near-field boundary conditions. Far-field conditions that account for the effects of mean swirl and the radial dependence of the steady and unsteady flow variables must still be developed to complete the formulation of the three-dimensional steady and first-harmonic, unsteady flow problems.

The numerical models developed herein for determining the steady and linearized unsteady flows are based on the nonlinear, time-accurate, Euler analysis developed in [WJS88]. It involves a time-independent transformation from reference physical to computational coordinates and a pseudo-time marching procedure in which the steady and the first-harmonic, unsteady flowss are determined by marching implicitly in pseudo-time, using local time stepping, until converged steady-state solutions are determined. The pseudo-time derivatives are approximated by first-order difference approximations, and, except for this change, the numerical model for the steady flow is essentially identical to the one used in [WJS88] for

nonlinear unsteady flows. The linearized unsteady equations contain source terms, that depend on the blade motion, and the spatial differencing directions used to evaluate the unsteady flux vectors are based on the steady flow solution.

In previous work [HSR91] the time-accurate, nonlinear, numerical model of [WJS88] was implemented into the multi-block, finite-volume code, called NPHASE, to provide a two-dimensional, unsteady aerodynamic analysis for vibrating cascades. The NPHASE code has been used as the basis for implementing the steady and linearized unsteady aerodynamic models, described in this report. In particular, nonlinear steady flows are predicted using a slightly updated version of NPHASE, and linearized unsteady flows are determined using a new code, called LINFLUX, which has been constructed, from the original NPHASE analysis. As part of the present effort, the surface-boundary-condition implementation used in NPHASE has been modified to reduce spurious numerical losses, and one- and approximate, two-dimensional, far-field conditions [Gil90] have been incorporated to allow application to unsteady flows excited by external aerodynamic disturbances. Unfortunately, the latter conditions have been found to result in significant reflections, at the inflow and outflow boundaries, of outgoing unsteady disturbance waves. Consequently, exact, single-frequency, far-field conditions have been constructed and implemented into LINFLUX. These conditions seem to eliminate the non-physical reflections, indicating that similar conditions should be incorporated into the NPHASE analysis in the future.

To evaluate the capabilities of the LINFLUX analysis, we have applied it to benchmark, two-dimensional, unsteady cascade flows. In particular, we have considered subsonic and transonic flows through the Tenth Standard Cascade Configuration in which unsteady aerodynamic responses are excited by prescribed blade vibrations, acoustic disturbances at inlet and exit, and entropic and vortical disturbances at inlet. For each example, LINFLUX predictions have been compared with other analytical predictions; namely, predictions based on the time-accurate, nonlinear, analysis NPHASE, and/or those based on the linearized potential analysis LINFLO [Ver92, Ver93].

The results of this study indicate that LINFLUX gives response information that is in close agreement with the results of the earlier analyses, NPHASE and LINFLO, for unsteady subsonic flows excited by blade vibrations or acoustic disturbances that travel towards the blade row. However, improved LINFLUX capabilities are needed for transonic flows and for flows excited by vortical gusts. In particular, the shock modeling or directional differencing, used in LINFLUX, should be modified so that LINFLUX and NPHASE will provide consistent response information in the vicinities of shocks for unsteady transonic flows. Also, the LINFLUX code should be modified to allow more accurate predictions of the unsteady flows excited by vortical gusts. This will probably involve the implementation of higher-order surface boundary conditions to reduce the amount of spurious numerical entropy and vorticity that is generated at blade surfaces. Future work should also be directed towards implementing accurate far field conditions into NPHASE. This would allow NPHASE to be applied to unsteady flows excited by incident aerodynamic disturbances. It would also allow LINFLUX and NPHASE calculations to be performed on the same mesh, which should help to clarify the discrepancies, cited in this report, between the nonlinear and linear Euler predictions in the vicinities of blade leading edges and in the supersonic regions of unsteady transonic flow fields. Finally, steps will also have to be taken to improve the efficiency of LINFLUX transonic and vortical gust calculations.

The primary reason for developing nonlinear and linearized unsteady Euler analyses for blade rows is the need to predict three-dimensional unsteady flows in which the effects of mean swirl and radial variation are important. Thus, the follow-on to the present research effort will be directed towards implementing the aerodynamic and numerical formulations, outlined in this report, into a three-dimensional version of the LINFLUX code. In addition to the problems associated with the numerical modeling of shocks and vortical gusts, another major difficulty must be overcome. This involves the development and implementation of appropriate far-field conditions for three-dimensional steady and unsteady flow calculations.

Acknowledgements

References

[Ari62]   A. Aris. *Vectors, Tensors and the Basic Equations of Fluid Mechanics*. Prentice-Hall, Englewood Cliffs, New Jersey, 1962.

[ATP84]   D. A. Anderson, J. C. Tannehill, and R. H. Pletcher. *Computational Fluid Mechanics and Heat Transfer*, 1984. Hemisphere, New York, pp. 252–255.

[BH92]   T. A. Beach and G. Hoffman. IGB Grid: User's Manual (A Turbomachinery Grid Generation Code. CR 189104, NASA, January 1992.

[Cas83]   J. R. Caspar. Unconditionally Stable Calculation of Transonic Potential Flow through Cascades using an Adaptive Mesh for Shock Capture. *Transactions of the ASME: Journal of Engineering for Power*, 105(3):504–513, July 1983.

[FS83]   T. H. Fransson and P. Suter. Two-Dimensional and Quasi Three-Dimensional Experimental Standard Configurations for Aeroelastic Investigations in Turbomachine-Cascades. Report LTA-TM-83-2, Ecole Polytechnique Federale de Lausanne, Lausanne, Switzerland, September 1983.

[FV93]   T. H. Fransson and J. M. Verdon. Standard Configurations for Unsteady Flow through Vibrating Axial-Flow Turbomachine Cascades. *Unsteady Aerodynamics, Aeroacoustics and Aeroelasticity of Turbomachines and Propellers*, pages 859–889, 1993. Springer-Verlag, New York, edited by H. M. Atassi.

[Gil90]   M. B. Giles. Nonreflecting Boundary Conditions for Euler Equation Calculations. *AIAA Journal*, 28(12):2050–2058, December 1990.

[Gil93]   M. B. Giles. A Framework for Multi-Stage Unsteady Flow Calculations. In H. M. Atassi, editor, *Unsteady Aerodynamics, Aeroacoustics, and Aeroelasticity of Turbomachines and Propellers*, pages 57–72, 1993. Springer-Verlag, New York, edited by H. M. Atassi.

[Gol76]   M. E. Goldstein. *Aeroacoustics*. McGraw-Hill International Book Company, New York, N.Y., 1976.

[HC93a]   K. C. Hall and W. S. Clark. Linearized Euler Predictions of Unsteady Aerodynamic Loads in Cascades. *AIAA Journal*, 31(3):540–550, March 1993.

[HC93b]   D. G. Holmes and H. A. Chuang. 2D Linearized Harmonic Euler Flow Analysis for Flutter and Forced Response. *Unsteady Aerodynamics, Aeroacoustics, and Aeroelasticity of Turbomachines and Propellers*, pages 213–230, 1993. Springer-Verlag, New York, edited by H. M. Atassi.

[HCL93]   K. C. Hall, W. S. Clark, and C. B. Lorence. A Linearized Euler Analysis of Unsteady Transonic Flows in Turbomachinery. ASME Paper 93-GT-94, 38th International Gas Turbine and Aeroengine Congress and Exposition, Cincinnati, Ohio, May 24–27 1993.

[HL92]   K. C. Hall and C. B. Lorence. Calculation of Three-Dimensional Unsteady Flows in Turbomachinery Using the Linearized Harmonic Euler Equations. ASME Paper 92-GT-736, International Gas Turbine and Aeroengine Congress and Exposition, Cologne, Germany, June 1-4 1992.

[HSR91]   D. L. Huff, T. W. Swafford, and T. S. R. Reddy. Euler Flow Predictions for an Oscillating Cascade Using a High Resolution Wave-Split Scheme. ASME Paper 91-GT-198, International Gas Turbine and Aeroengine Congress and Exposition,. Orlando, Florida, June 3-6 1991.

[Huf87]   D. L. Huff. Numerical Simulations of Unsteady, Viscous, Transonic Flow Over Isolated and Cascaded Airfoils Using a Deforming Grid. Paper 87-1316, AIAA 19th Fluid Dynamics, Plasma Dynamics and Lasers Conference, Honolulu, Hawaii, June 8-10 1987.

[Ker70]   J. L. Kerrebrock. Small Disturbances in Compressor Annuli with Swirl. Report 104, Gas Turbine Laboratory, M.I.T., October 1970.

[KK93]   G. Kahl and A. Klose. Computation of Time Linearized Transonic Flow in Oscillating Cascades. ASME Paper 93-GT-269, 38th International Gas Turbine and Aeroengine Congress and Exposition, Cincinnati, Ohio, May 24-27 1993.

[Mou84]   T. H. Moulden. *Fundamentals of Transonic Flow*. John Wiley and Sons, Inc., New York, 1984.

[Nam87]   M. Namba. Three Dimensional Flows. In M. F. Platzer and F. O. Carta, editors, *AGARD Manual on Aeroelasticity in Axial-Flow Turbomachines*, chapter IV. AGARD, March 1987. Vol. 1, *Unsteady Turbomachinery Aerodynamics*, AGARD-AG-298.

[NS76]   R. H. Ni and F. Sisto. Numerical Computation of Nonstationary Aerodynamic of Flat Plate Cascades in Compressible Flow. *Transactions of the ASME: Journal of Engineering for Power*, 98(2):165-170, April 1976.

[OC84]   S. Osher and S. Chakravarthy. Very High Order Accurate TVD Schemes. Report 84-44, ICASE, September 1984.

[Roe81]   P. L. Roe. Approximate Riemann Solvers, Parameter Vectors and Difference Schemes. *Journal of Computational Physics*, 43:357-372, 1981.

[Roe85]   P. L. Roe. Some Contributions to the Modelling of Discontinuous Flows. In B. Engquist, S. Osher, and R. Somerville, editors, *Large-Scale Computations in Fluid Mechanics*, volume 22 of *Lectures in Applied Mathematics*, pages 163-193. 1985. Part 2.

[SG91]   A. P. Saxer and M. B. Giles. Quasi-3D Nonreflecting Boundary Conditions for Euler Equation Calculations. AIAA Paper 91-1603, 10th Computational Fluid Dynamics Conference, Honolulu, Hawaii, June 24-27 1991. pp. 845-857.

73

[SLH+94] T. W. Swafford, D. H. Loe, D. L. Huff, D. H. Huddleston, and T. S. R. Reddy. The Evolution of NPHASE: Euler/Navier-Stokes Computations of Unsteady Two-Dimensional Cascade Flow Fields. AIAA Paper 94-1834, 12th Applied Aerodynamics Conference, Colorado Springs, Colorado, June 20–23 1994.

[SW81] J. L. Steger and R. F. Warming. Flux Vector Splitting of the Inviscid Gasdynamic Equations with Application to Finite Difference Methods. *Journal of Computational Physics*, 40(2):263–293, April 1981.

[SWH93] K. Sreenivas, D. L. Whitfield, and D. L. Huff. High Resolution Numerical Simulation of the Linearized Euler Equations in Conservation Law Form. AIAA Paper 93-2934, 24th Fluid Dynamics Conference, Orlando, Florida, July 6–9 1993.

[TS62] J. M. Tyler and T. G. Sofrin. Axial Flow Compressor Noise Studies. *SAE Transactions*, 70:309–332, 1962.

[TTM77] J. F. Thompson, F. C. Thames, and W. Mastin. A Code for Numerical Generation of Boundary-Fitted Curvilinear Coordinate Systems on Fields Containing any Number of Arbitrary Two-Dimensional Bodies. *Journal of Computational Physics*, 24(3):274–302, 1977.

[UV91] W. J. Usab, Jr. and J. M. Verdon. Advances in the Numerical Analysis of Linearized Unsteady Cascade Flows. *Transactions of the ASME: Journal of Turbomachinery*, 113(4):633–643, October 1991.

[Ver89a] J. M. Verdon. The Unsteady Aerodynamic Response to Arbitrary Modes of Blade Motion. *Journal of Fluids and Structures*, 3(3):255–274, May 1989.

[Ver89b] J. M. Verdon. The Unsteady Flow in the Far Field of an Isolated Blade Row. *Journal of Fluids and Structures*, 3(2):123–149, March 1989.

[Ver92] J. M. Verdon. Linearized Unsteady Aerodynamics for Turbomachinery Aeroelastic Applications. *Journal de Physique III*, 2(4):481–506, April 1992. Also presented as Paper 90-2355, AIAA/SAE/ASME/ASEE 26th Joint Propulsion Conference, Orlando, Florida, July 16–18, 1990.

[Ver93] J. M. Verdon. Unsteady Aerodynamic Methods for Turbomachinery Aeroelastic and Aeroacoustic Applications. *AIAA Journal*, 31(2):235–250, February 1993.

[VL74] B. Van Leer. Towards the Ultimate Conservative Differencing Scheme, Part II. *Journal of Computational Physics*, 14(4):361–370, March 1974.

[VTM82] C. S. Ventres, M. A. Theobald, and W. D. Mark. Turbofan Noise Generation, Volume 1: Analysis. CR 167952, NASA, July 1982.

[VW93] K. J. Vanden and D. L. Whitfield. Direct and Iterative Algorithms for the Three-Dimensional Euler Equations. AIAA Paper 93-3378-CP, 11th AIAA Computational Fluid Dynamics Conference, Orlando, FL, June 1993.

[WB77]   R. F. Warming and R. M. Beam. On the Construction and Application of Implicit Factored Schemes for Conservation Laws. In *SIAM-AMS Proceedings*, 1977. Symposium on Computational Fluid Dynamics, New York, April 16–17, 1977, Vol. 11.

[Whi87] D. S. Whitehead. Classical Two-Dimensional Methods. In M. F. Platzer and F. O. Carta, editors, *AGARD Manual on Aeroelasticity in Axial-Flow Turbomachines*, chapter III. AGARD, March 1987. Vol. 1, *Unsteady Turbomachinery Aerodynamics*, AGARD-AG-298.

[WJS88] D.L. Whitfield, J.M. Janus, and L.B. Simpson. Implicit Finite Volume High Resolution Wave Split Scheme for Solving the Unsteady Three-Dimensional Euler and Navier-Stokes Equations on Stationary or Dynamic Grids. Report MSSU-EIRS-ASE-88-2, Mississippi State Engineering and Industrial Research Station, 1988.

[WT91]   D. L. Whitfield and L. Taylor. Discretized Newton-Relaxation Solution of High Resolution Flux-Difference Split Schemes. Paper 91-1539, AIAA 10th Computational Fluid Dynamics Conference, Honolulu, Hawaii, June 24–26 1991.

List of Figures

Figure 13. Pressure-displacement function distributions and work per cycle predictions for the transonic ($M_{-\infty} = 0.8$, $\Omega_{-\infty} = 58$ deg) NACA 5506 cascade undergoing torsional blade vibrations about midchord at $\alpha = 2$ deg and $\omega = 1$: (a) in-phase ($\sigma = 0$ deg) torsional blade motion; (b) out-of-phase ($\sigma = 180$ deg) motion.

Figure 14. Pressure-displacement function distributions and work per cycle predictions for the transonic ($M_{-\infty} = 0.8$, $\Omega_{-\infty} = 58$ deg) NACA 5506 cascade undergoing bending vibrations at $h_y = 0.01$ and $\omega = 1$: (a) in-phase ($\sigma = 0$ deg) bending vibration; (b) out-of-phase ($\sigma = 180$ deg) bending vibration.

Figure 15. Work per cycle vs. interblade phase angle for the transonic ($M_{-\infty} = 0.8$, $\Omega_{-\infty} = 58$ deg) NACA 5506 cascade undergoing blade vibrations at $\omega = 1$: (a) torsional vibrations about midchord with $\alpha = 2$ deg; (b) bending vibrations with $h_y = 0.01$.

Figure 16. Mach number contours and blade surface Mach number distributions for steady subsonic flow at $M_{-\infty} = 0.5$, and $\Omega_{-\infty} = 55$ deg through the NACA 5506 cascade.

Figure 17. Contours of the in-phase component of the unsteady pressure due to the interaction of an acoustic excitation from upstream ($p_{I,-\infty} = (1,0)$, $\omega = 5$, $\sigma = -90$ deg) with the subsonic ($M_{-\infty} = 0.5$, $\Omega_{-\infty} = 55$ deg) NACA 5506 cascade: (a) LINFLO calculation; (b) LINFLUX calculation.

Figure 18. Unsteady surface pressure distributions due to the interaction of an acoustic excitation from upstream ($p_{I,-\infty} = (1,0)$, $\omega = 5$, $\sigma = -90$ deg) with the subsonic ($M_{-\infty} = 0.5$, $\Omega_{-\infty} = 55$ deg) NACA 5506 cascade.

Figure 19. Contours of the in-phase component of the unsteady pressure due to the interaction of an acoustic excitation from downstream ($p_{I,+\infty} = (1,0)$, $\omega = 5$, $\sigma = -90$ deg) with the subsonic ($M_{-\infty} = 0.5$, $\Omega_{-\infty} = 55$ deg) NACA 5506 cascade: (a) LINFLO calculation; (b) LINFLUX calculation.

Figure 20. Unsteady surface pressure distributions due to the interaction of an acoustic excitation from downstream ($p_{I,+\infty} = (1,0)$, $\omega = 5$, $\sigma = -90$ deg) with the subsonic ($M_{-\infty} = 0.5$, $\Omega_{-\infty} = 55$ deg) NACA 5506 cascade.

Figure 21. Contours of the in-phase component of the unsteady entropy for an entropic gust ($s_{-\infty} = (1,0)$, $\omega = 5$, $\sigma = -\pi$) interacting with the subsonic ($M_{-\infty} = 0.5$, $\Omega_{-\infty} = 55$ deg) NACA 5506 cascade: (a) LINFLO calculation; (b) LINFLUX calculation.

Figure 22. Contours of the in-phase component of the unsteady vorticity for a vortical gust ($\mathbf{v}_{R,-\infty} \cdot \mathbf{e}_N = (1,0)$, $\omega = 5$, $\sigma = -\pi$) interacting with the subsonic ($M_{-\infty} = 0.5$, $\Omega_{-\infty} = 55$ deg) NACA 5506 cascade: (a) LINFLO calculation; (b) LINFLUX calculation.

Figure 23. Contours of the in-phase component of the unsteady pressure response for a vortical gust ($\mathbf{v}_{R,-\infty} \cdot \mathbf{e}_N = (1,0)$, $\omega = 5$, $\sigma = -\pi$) interacting with a subsonic ($M_{-\infty} = 0.5$, $\Omega_{-\infty} = 55$ deg) NACA 5506 cascade: (a) LINFLO calculation; (b) LINFLUX calculation.

Figure 24. Unsteady surface pressure distributions due to the interaction of a vortical gust $(\mathbf{v}_{R,-\infty} \cdot \mathbf{e}_N = (1,0), \; \omega = 5, \; \sigma = -\pi)$ and the subsonic $(M_{-\infty} = 0.5, \; \Omega_{-\infty} = 55 \; \text{deg})$ NACA 5506 cascade.
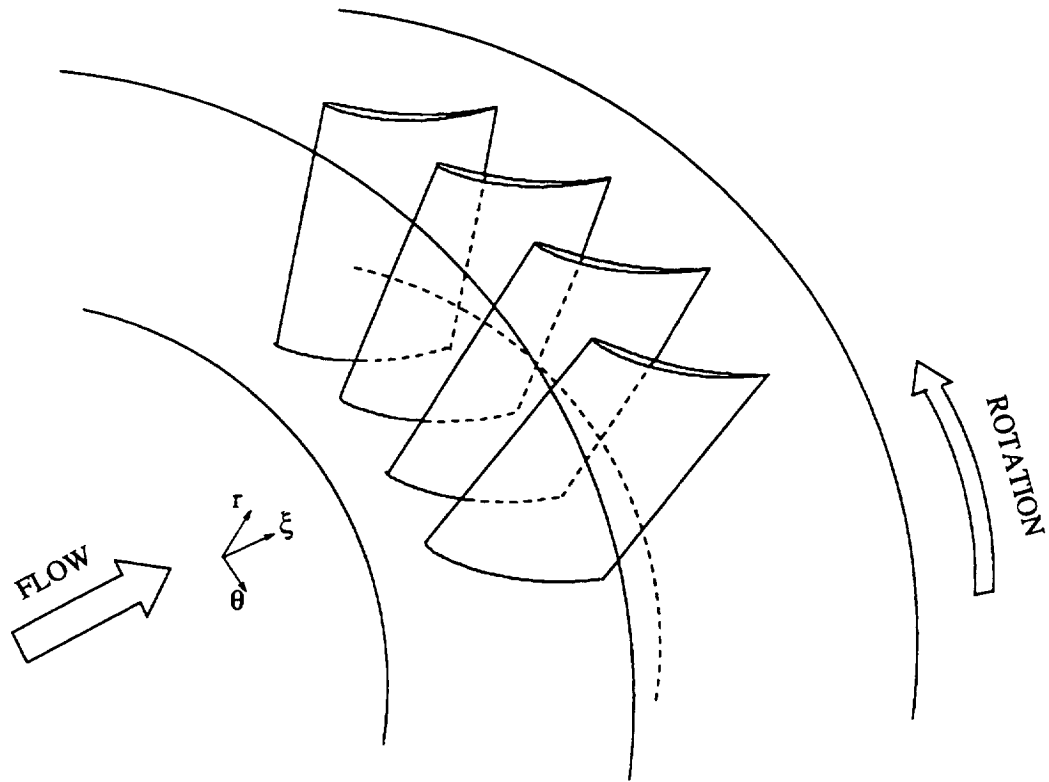
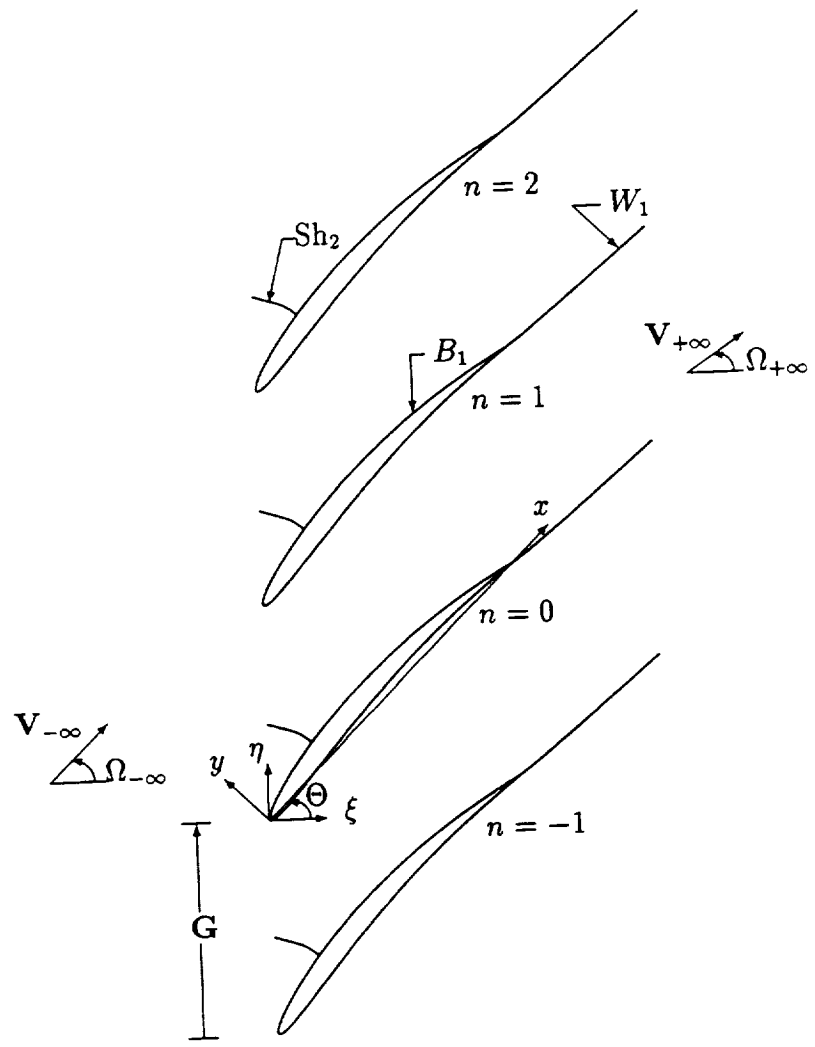Figure 1: Rotating axial compressor blade row operating within a cylindrical duct.

Figure 2: Two-dimensional section of a transonic compressor blade row viewed (from hub to tip) in rotating frame. A normal shock (Sh_n) impinges on the suction surface of the nth blade, and a vortex sheet wake (W_n) extends downstream from the trailing edge of the nth blade.
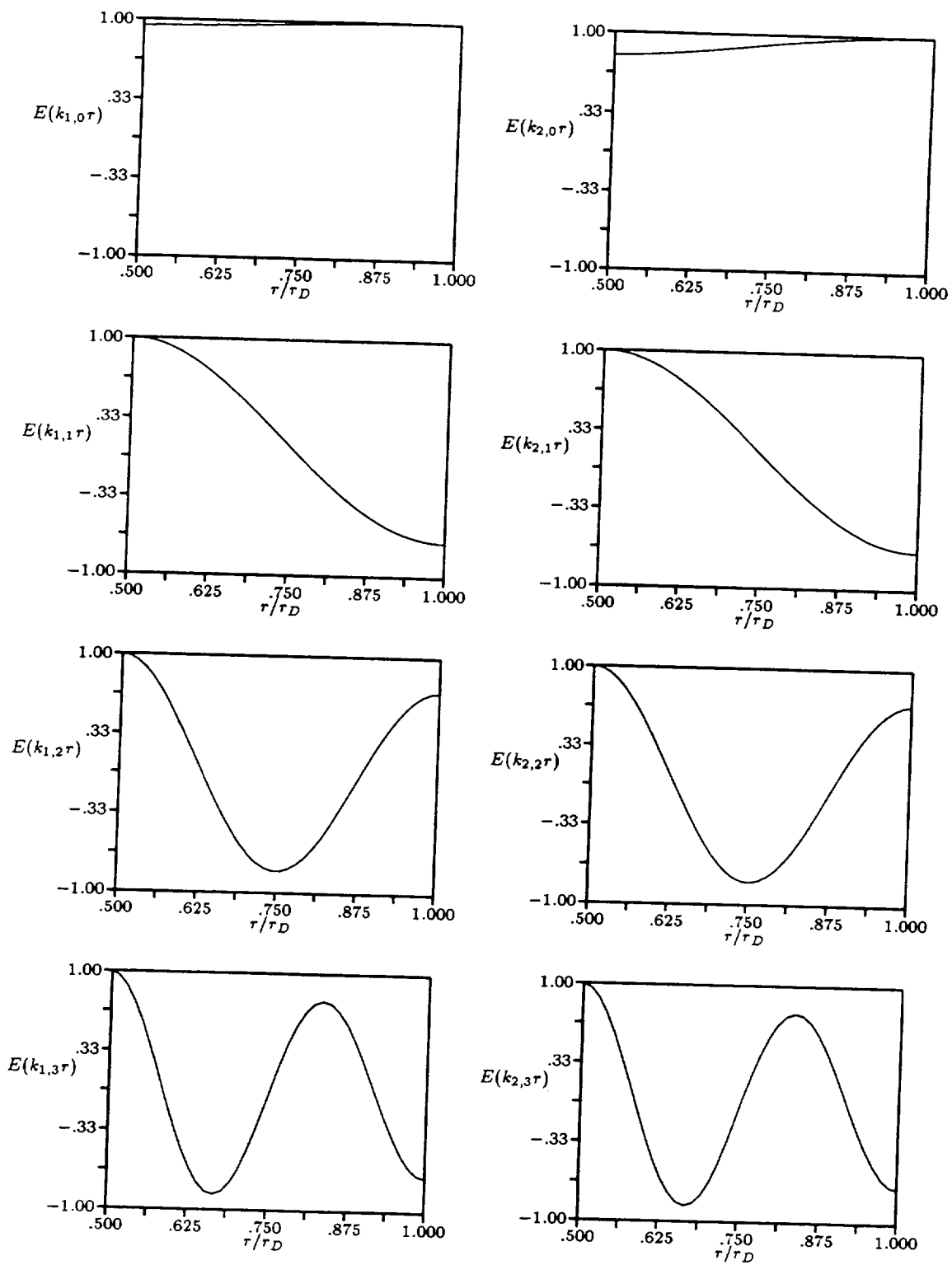
Figure 3: Characteristic E-functions for acoustic perturbations of a uniform axial mean flow.

(a)

(b)

(c)
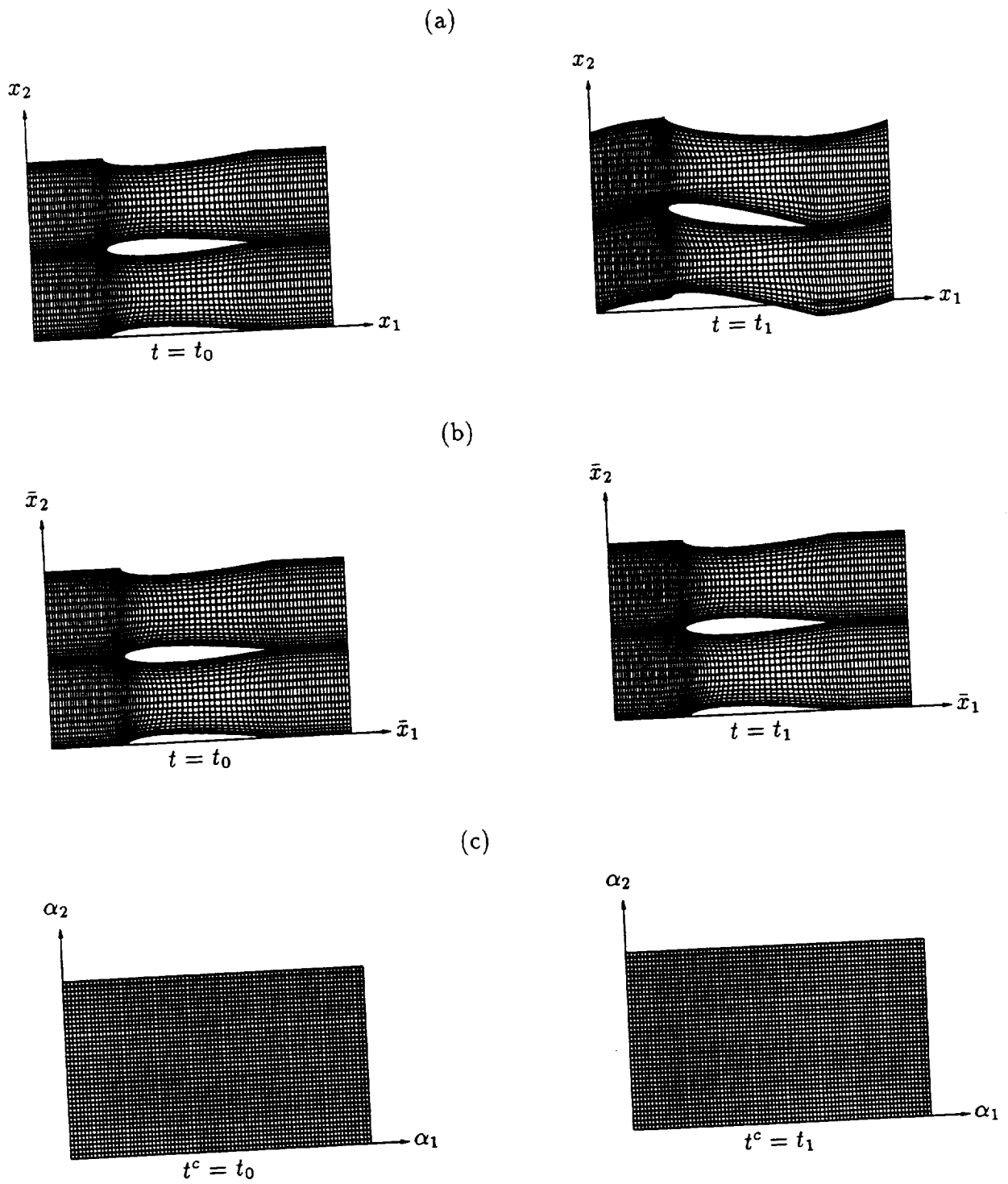
Figure 4: Computational grids: (a) deforming grid in physical space; (b) reference or steady-state grid in physical space; and (c) uniform orthogonal grid in computational space.
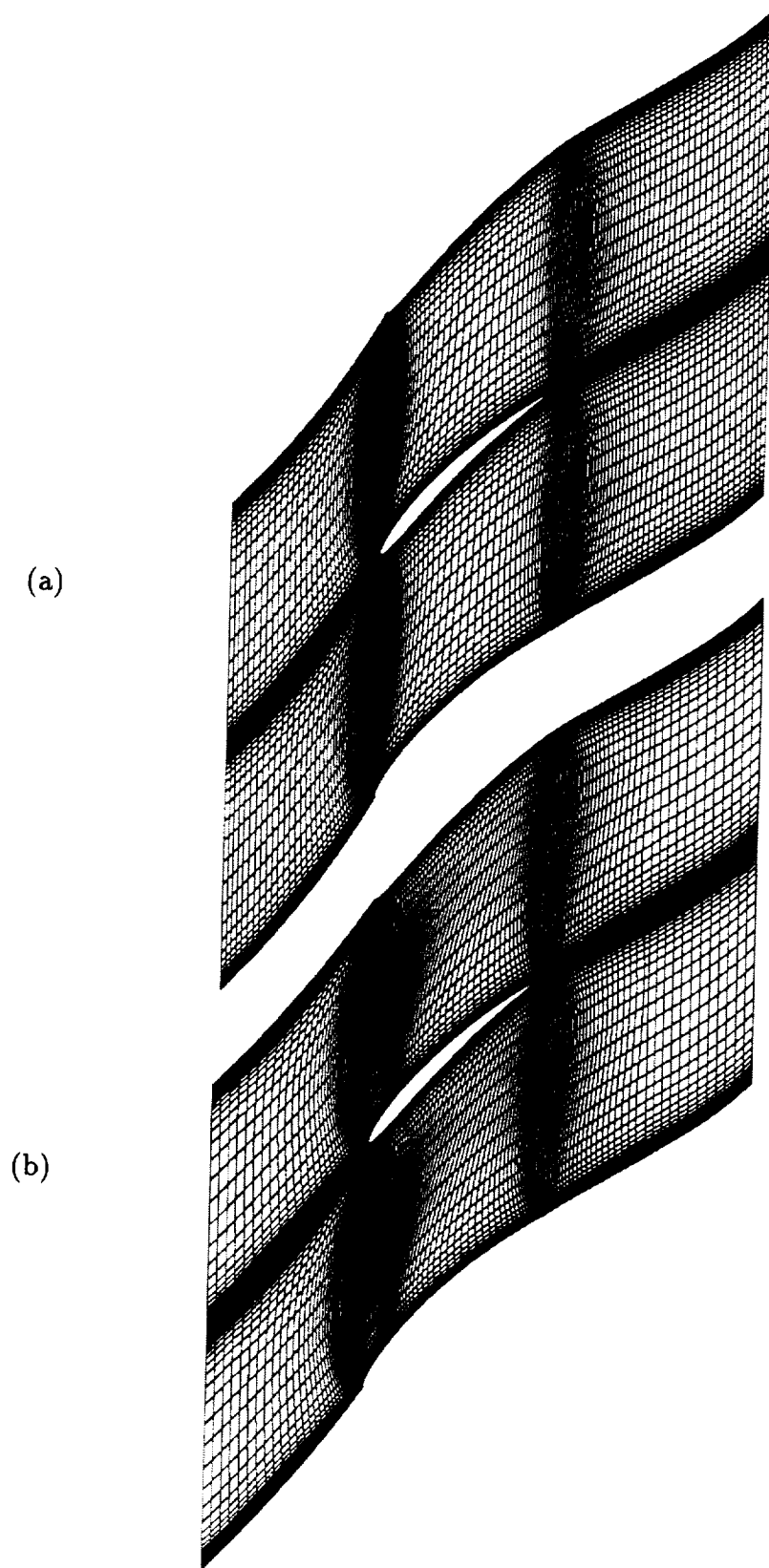
Figure 5: H-meshes used for steady (NPHASE) and linearized unsteady (LINFLUX) Euler calculations: (a) subsonic flow; (b) transonic flow.
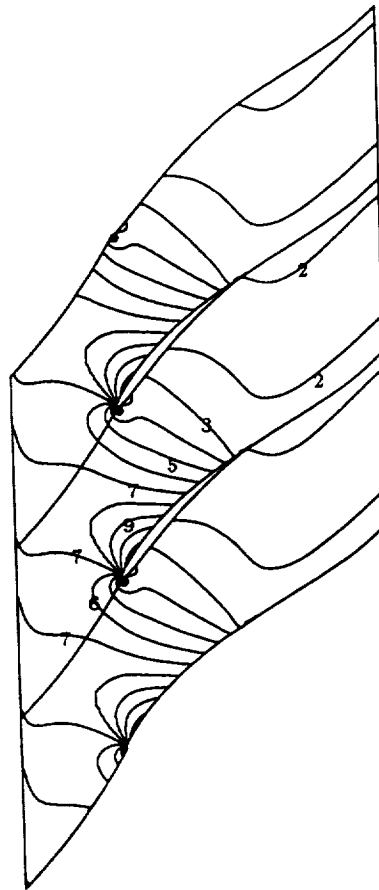
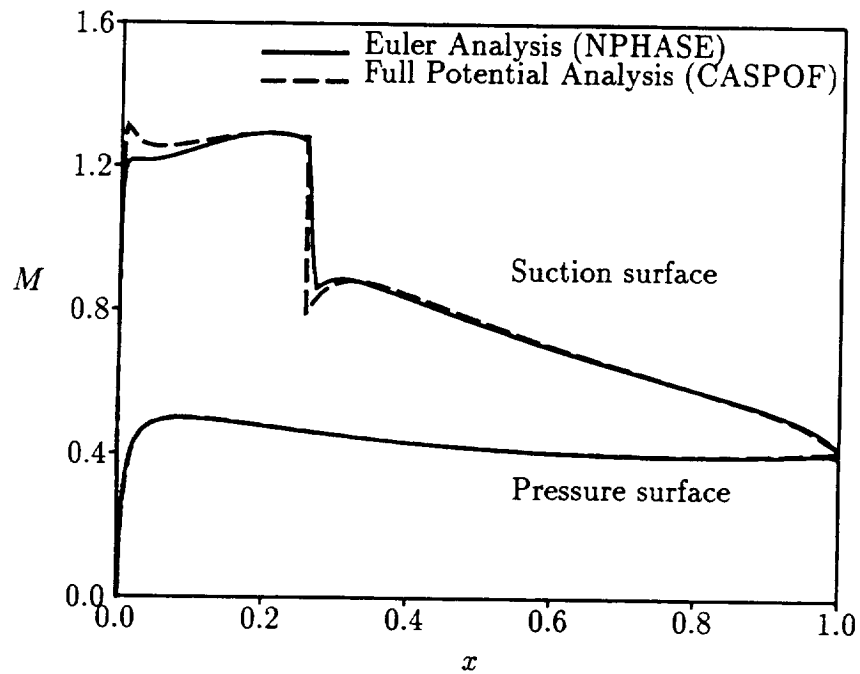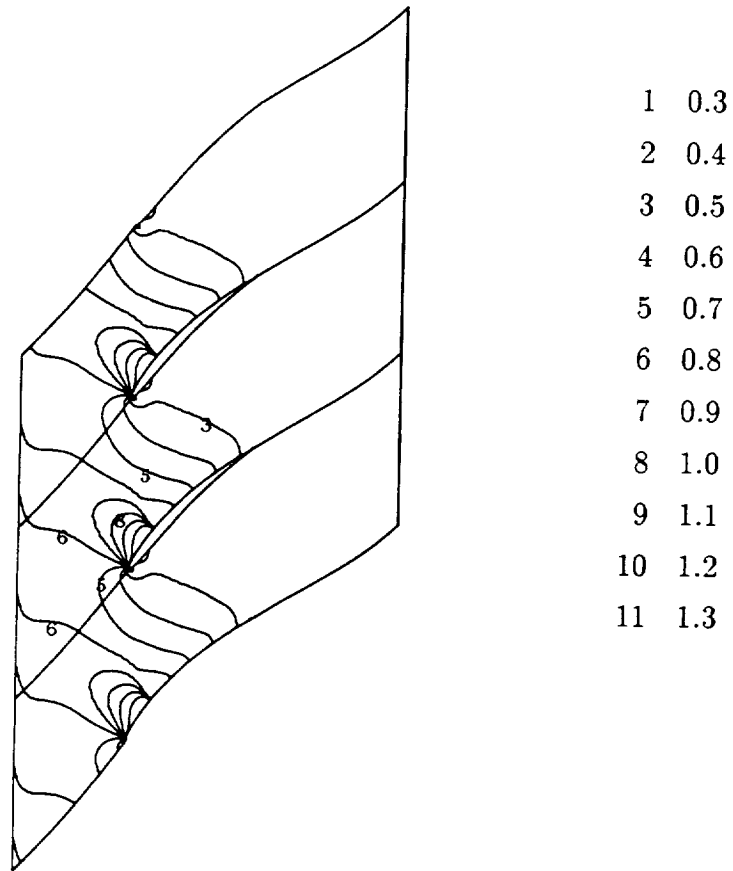|	
1	0.40
2	0.45
3	0.50
4	0.55
5	0.60
6	0.65
7	0.70
8	0.75
9	0.80
10	0.85
11	0.90
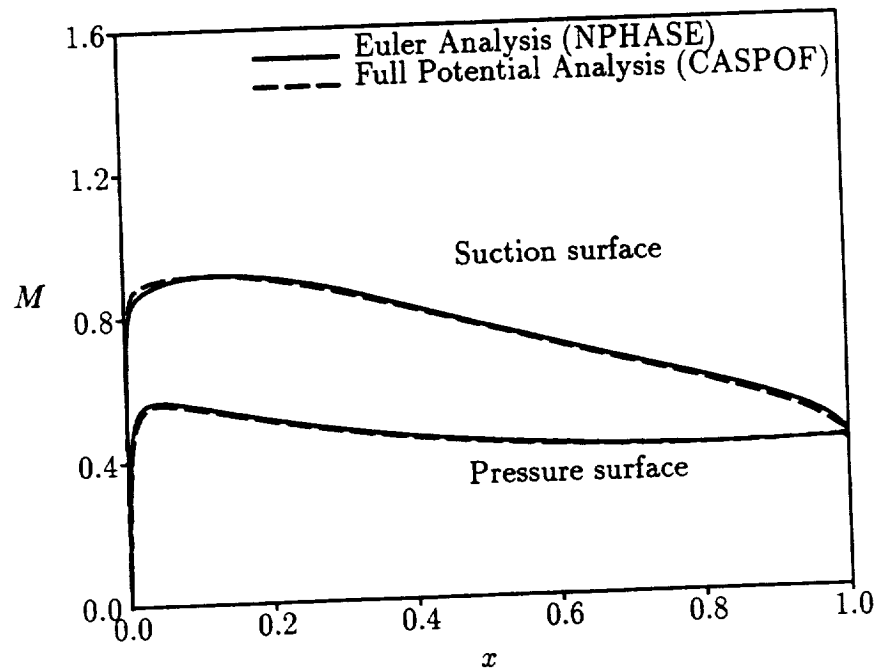
Figure 6: Mach number contours and blade surface Mach number distributions for steady subsonic flow at $M_{-\infty} = 0.7$ and $\Omega_{-\infty} = 55$ deg through the NACA 5506 (10th Standard) cascade.

1	-2.5
2	-2.0
3	-1.5
4	-1.0
5	-0.5
6	0.0
7	0.5
8	1.0
9	1.5
10	2.0
11	2.5
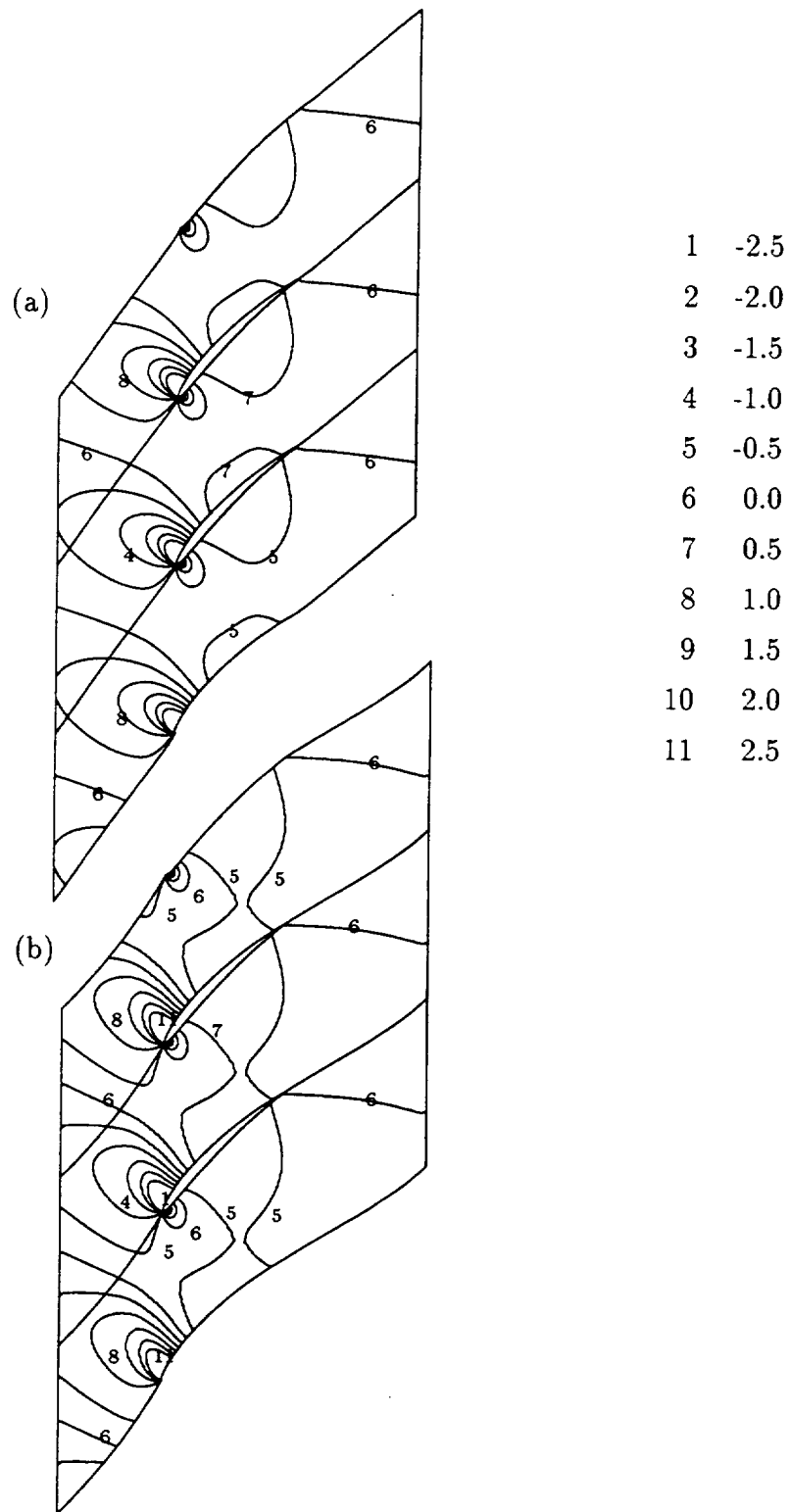
Figure 7: Contours of the out-of-phase component of the unsteady pressure, i.e., $Im\{p\}$, for the subsonic ($M_{-\infty} = 0.7$, $\Omega_{-\infty} = 55$ deg) NACA 5506 cascade undergoing an out-of-phase torsional blade vibration about midchord ($\alpha = 2$ deg, $\omega = 1$, $\sigma = 180$ deg): (a) linearized potential analysis (LINFLO); (b) linearized Euler analysis (LINFLUX).
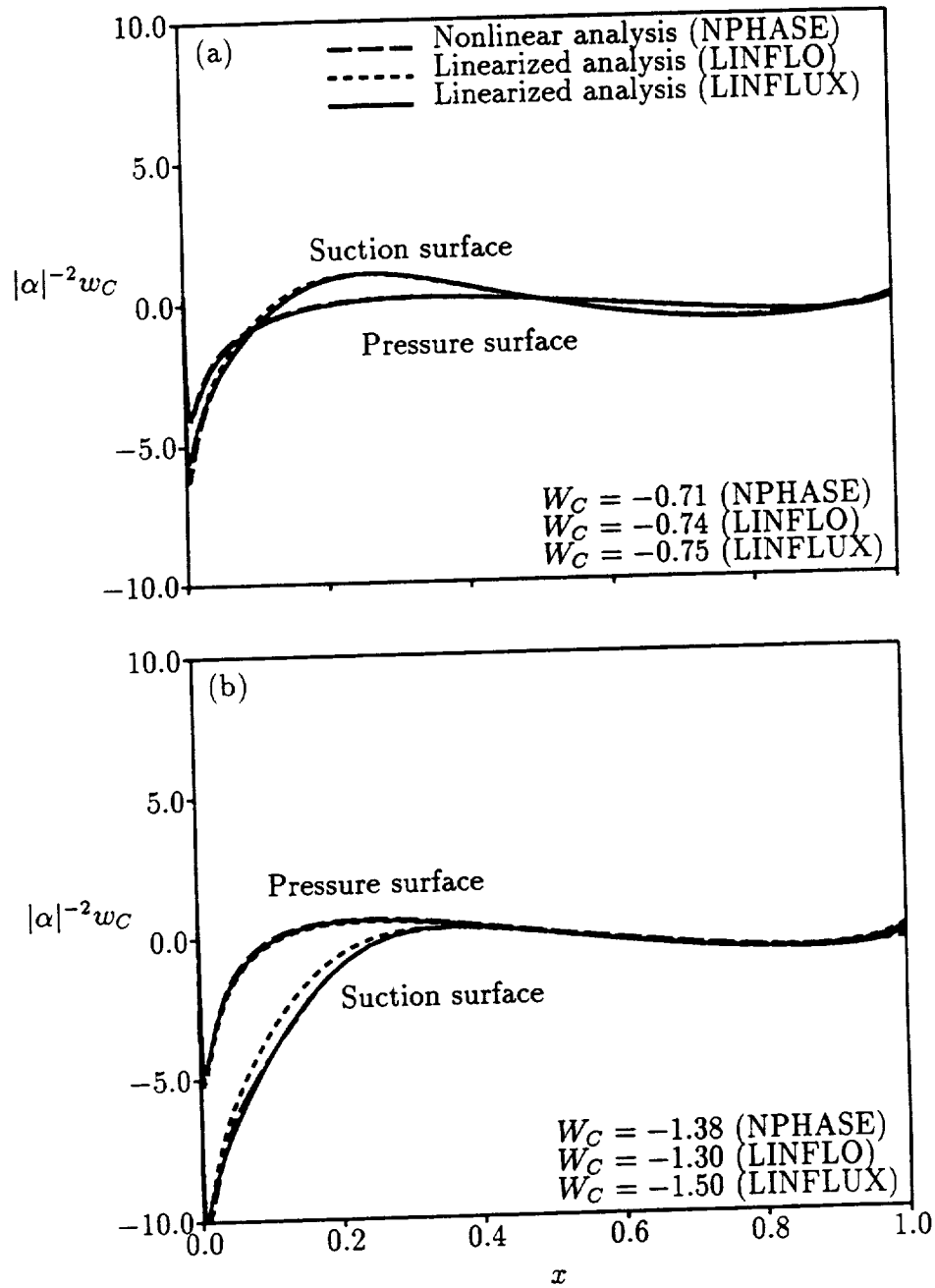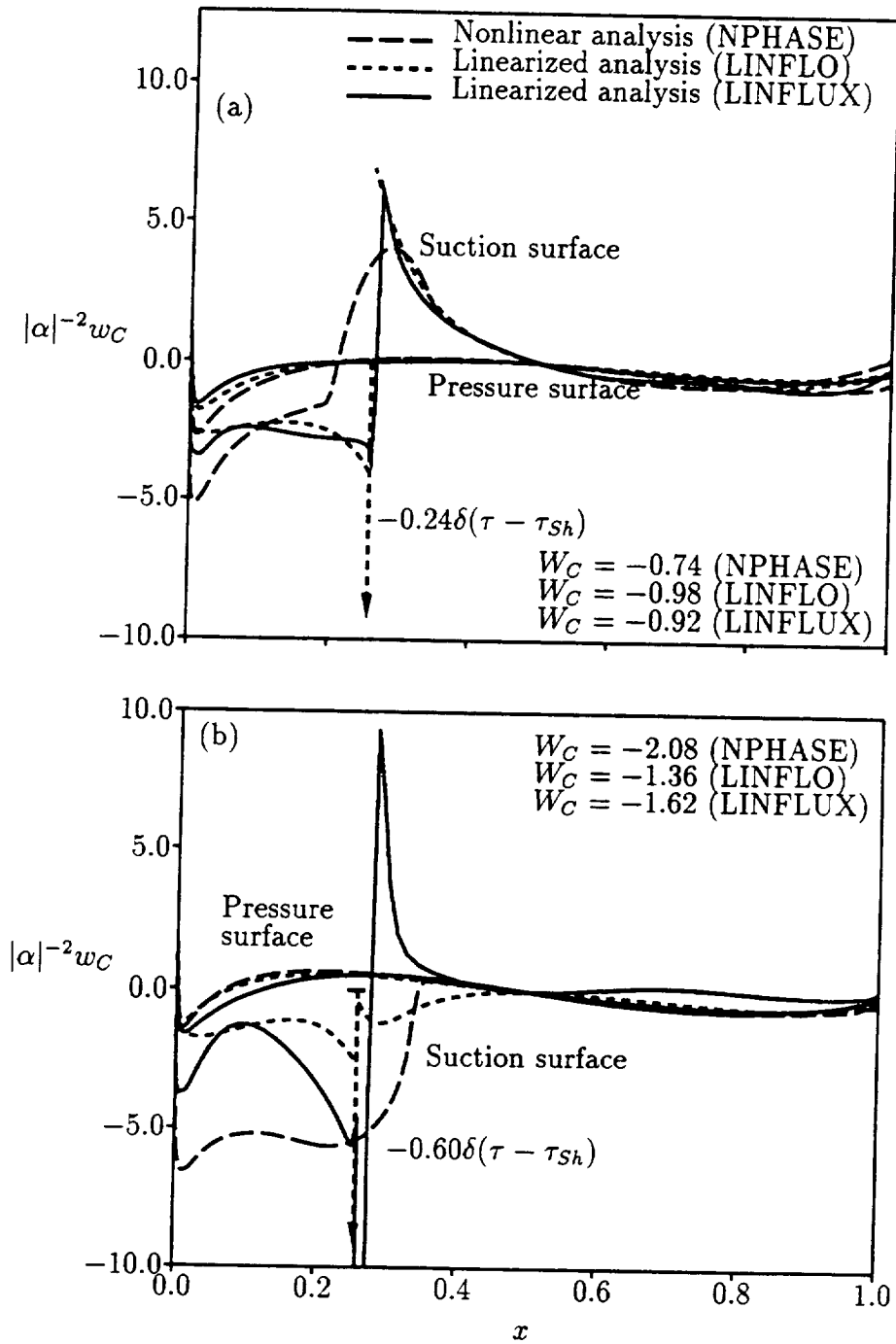
Figure 8: Pressure-displacement function distributions and work per cycle predictions for the subsonic ($M_{-\infty} = 0.7$, $\Omega_{-\infty} = 55$ deg) NACA 5506 cascade undergoing torsional blade vibrations about midchord at $\alpha = 2$ deg and $\omega = 1$: (a) in-phase ($\sigma = 0$ deg) torsional blade motions; (b) out-of-phase ($\sigma = 180$ deg) motions.
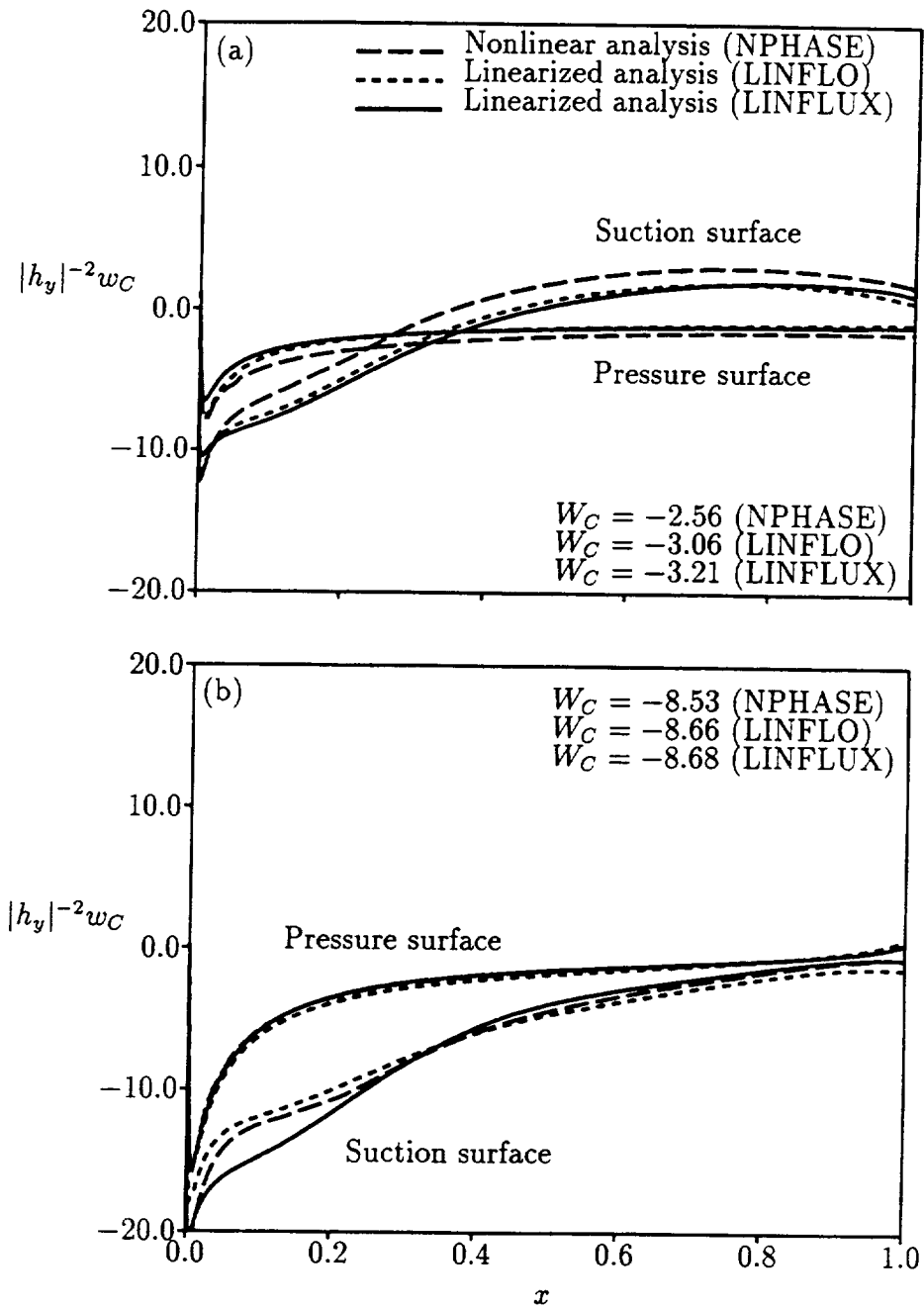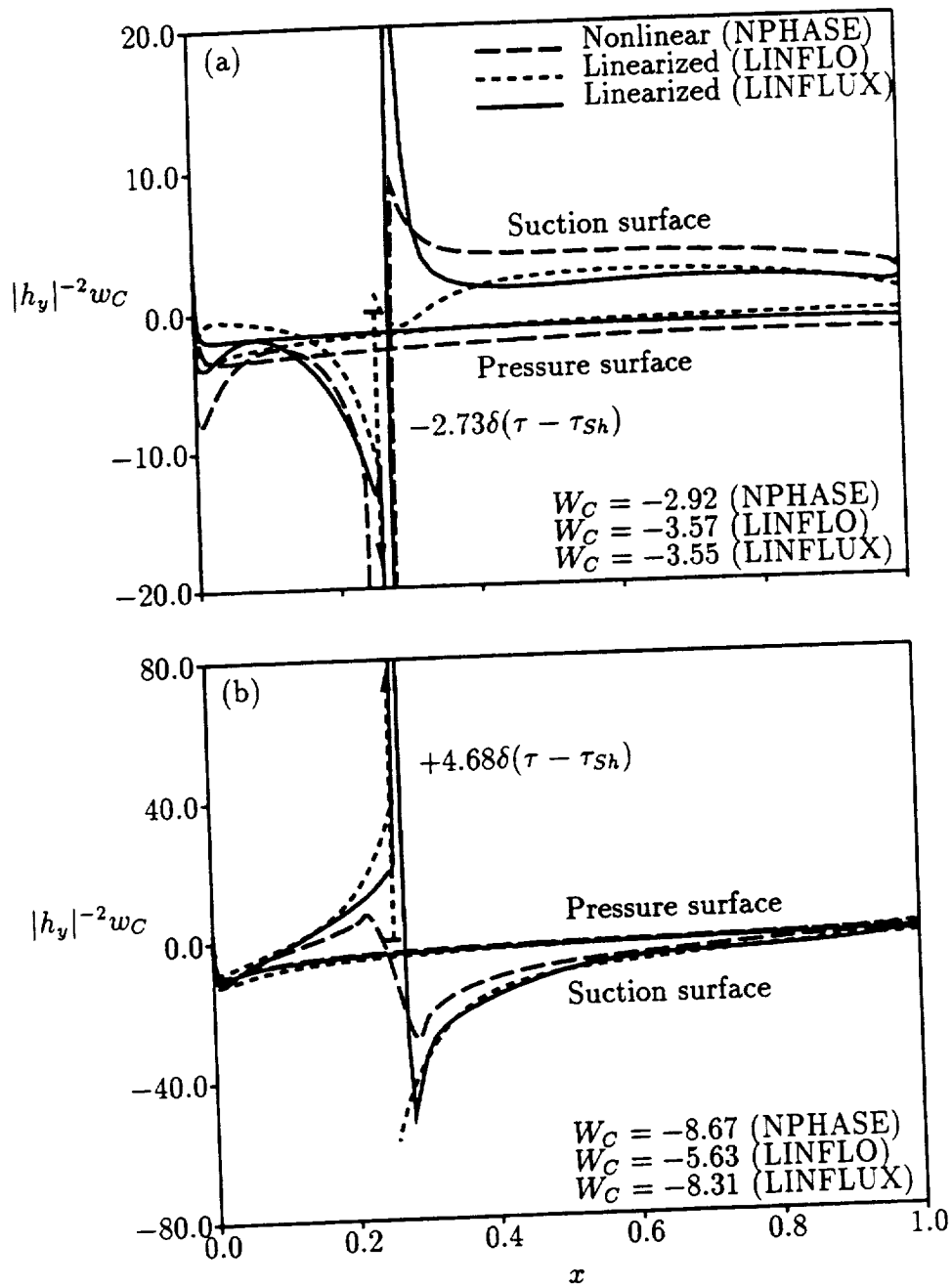
Figure 9: Pressure-displacement function distributions and work per cycle predictions for the subsonic ($M_{-\infty} = 0.7$, $\Omega_{-\infty} = 55$ deg) NACA 5506 cascade undergoing bending vibrations at $h_y = 0.01$ and $\omega = 1$: (a) in-phase ($\sigma = 0$ deg) bending motions; (b) out-of-phase ($\sigma = 180$ deg) motions.
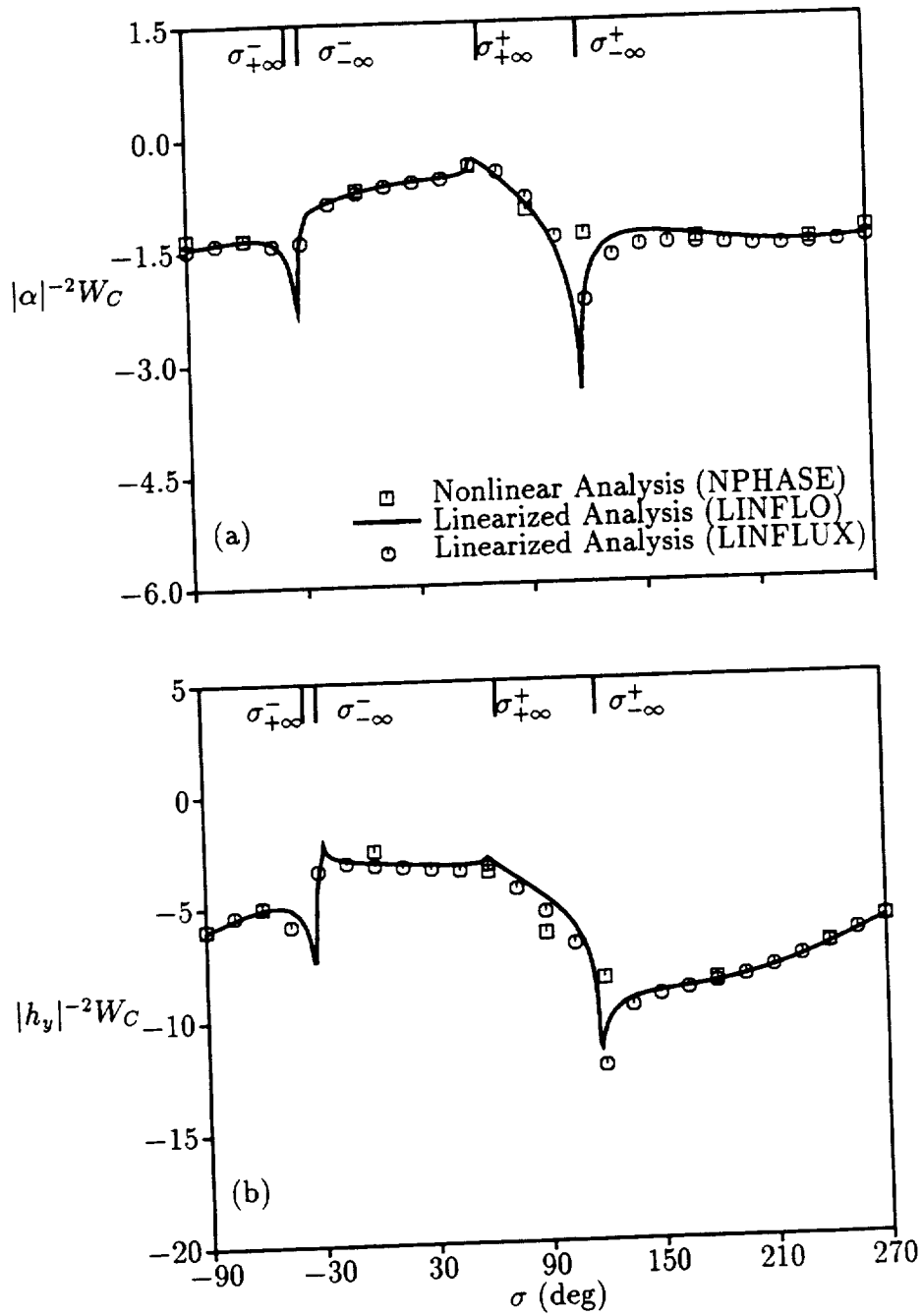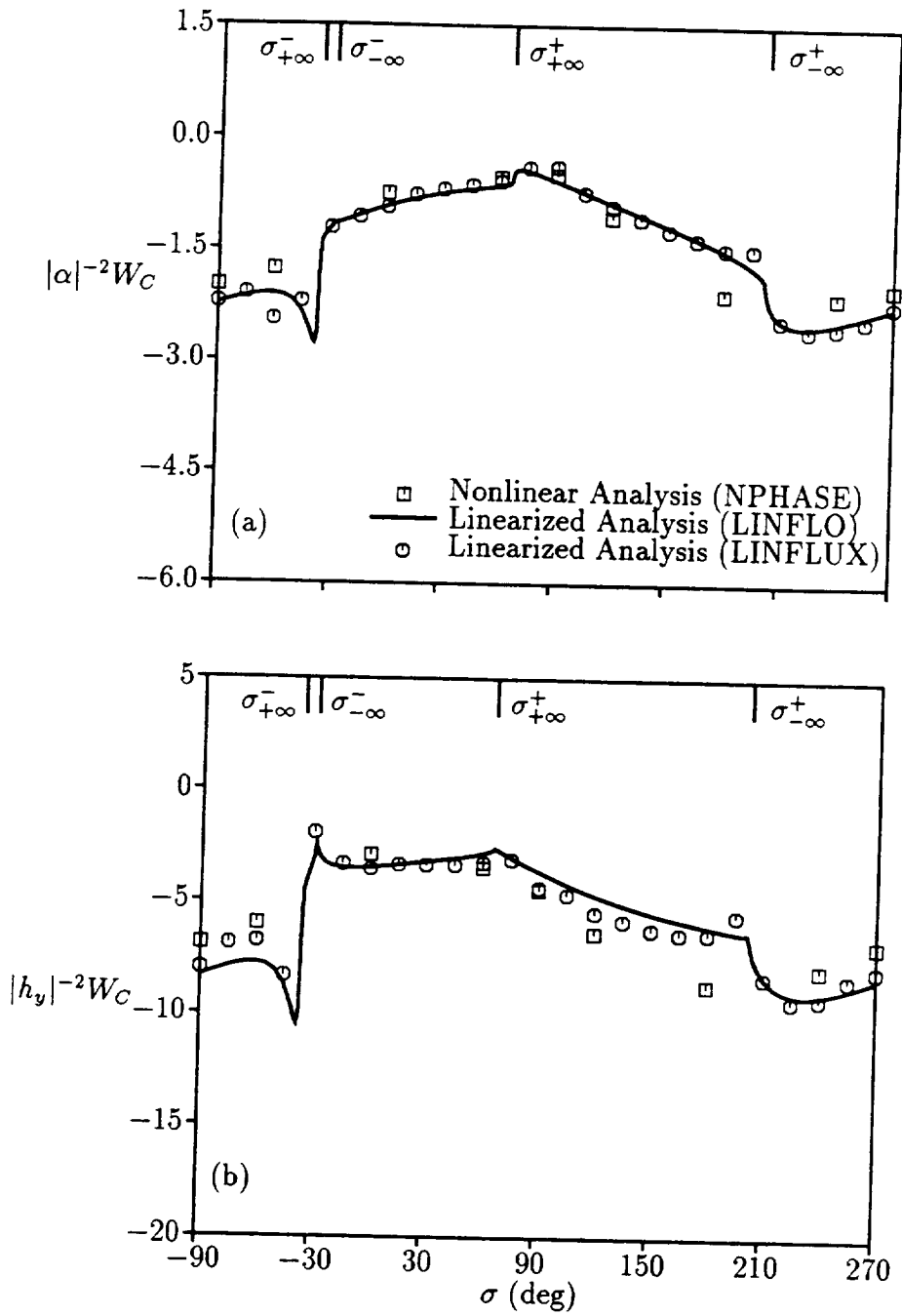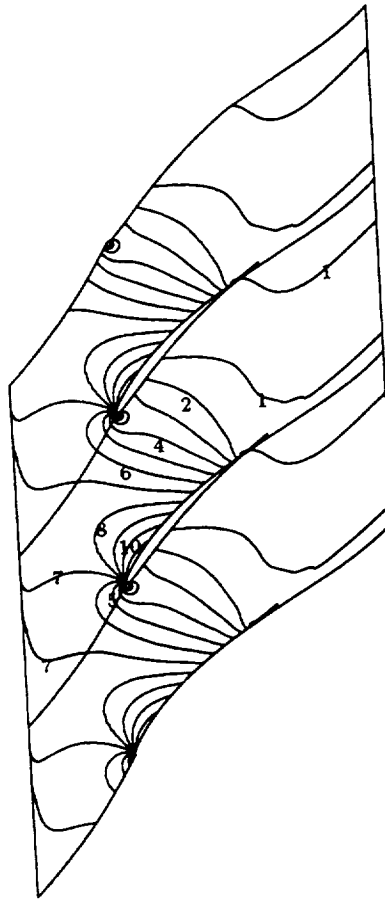
Figure 10: Work per cycle vs. interblade phase angle for the subsonic ($M_{-\infty} = 0.7$, $\Omega_{-\infty} = 55$ deg) NACA 5506 cascade undergoing blade vibrations at $\omega = 1$: (a) torsional vibrations about midchord with $\alpha = 2$ deg; (b) bending vibrations with $h_y = 0.01$.

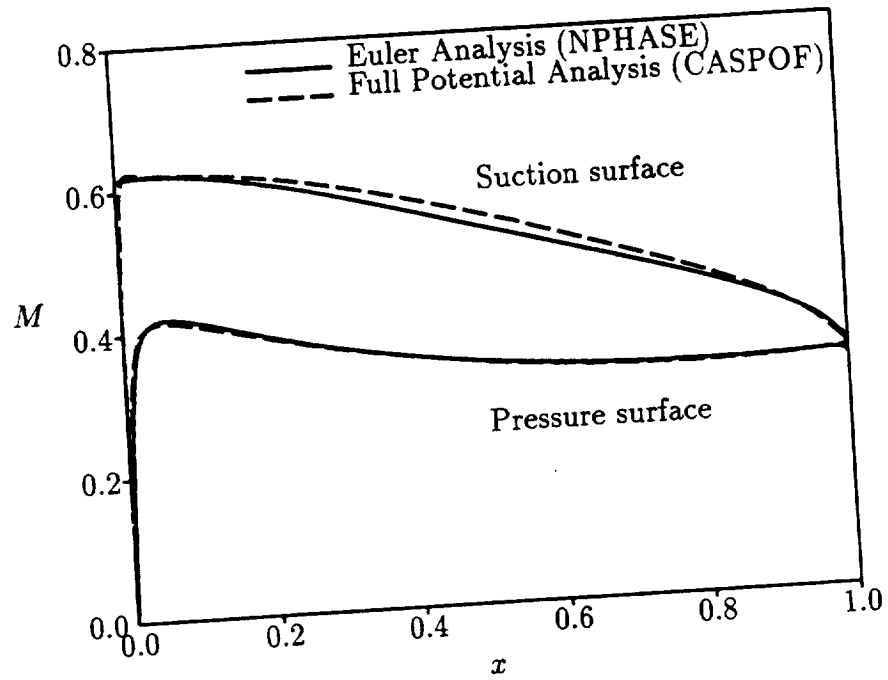| 1 | 0.3 |
2	0.4
3	0.5
4	0.6
5	0.7
6	0.8
7	0.9
8	1.0
9	1.1
10	1.2
11	1.3

Figure 11: Mach number contours and blade surface Mach number distributions for steady transonic flow at $M_{-\infty} = 0.8$, and $\Omega_{-\infty} = 58$ deg through the NACA 5506 (10th Standard) cascade.

(a)

(b)

1	-5.0
2	-4.0
3	-3.0
4	-2.0
5	-1.0
6	0.0
7	1.0
8	2.0
9	3.0
10	4.0
11	5.0
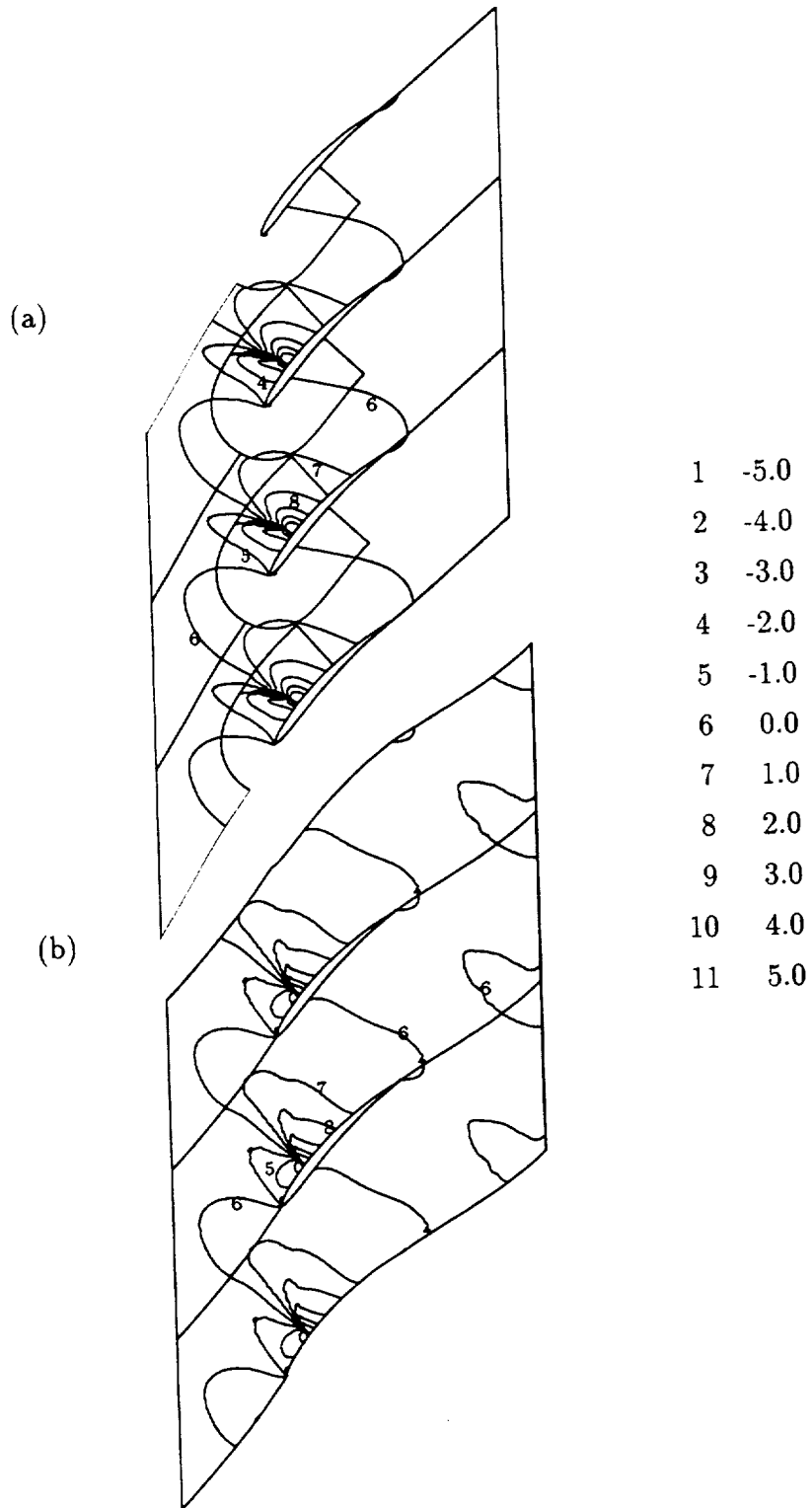
Figure 12: Contours of the out-of-phase component of the unsteady pressure, $Im\{p\}$, for the transonic ($M_{-\infty} = 0.8$, $\Omega_{-\infty} = 58$ deg) NACA 5506 cascade undergoing an in-phase torsional blade vibration about midchord ($\alpha = 2$ deg, $\omega = 1$, $\sigma = 180$ deg): (a) linearized potential analysis (LINFLO); (b) linearized Euler analysis (LINFLUX).

Figure 13: Pressure-displacement function distributions and work per cycle predictions for the transonic ($M_{-\infty} = 0.8$, $\Omega_{-\infty} = 58$ deg) NACA 5506 cascade undergoing torsional blade vibrations about midchord at $\alpha = 2$ deg and $\omega = 1$: (a) in-phase ($\sigma = 0$ deg) torsional blade motion; (b) out-of-phase ($\sigma = 180$ deg) motion.

Figure 14: Pressure-displacement function distributions and work per cycle predictions for the transonic ($M_{-\infty} = 0.8$, $\Omega_{-\infty} = 58$ deg) NACA 5506 cascade undergoing bending vibrations at $h_y = 0.01$ and $\omega = 1$: (a) in-phase ($\sigma = 0$ deg) bending vibration; (b) out-of-phase ($\sigma = 180$ deg) bending vibration.

Figure 15: Work per cycle vs. interblade phase angle for the transonic ($M_{-\infty} = 0.8$, $\Omega_{-\infty} = 58$ deg) NACA 5506 cascade undergoing blade vibrations at $\omega = 1$: (a) torsional vibrations about midchord with $\alpha = 2$ deg; (b) bending vibrations with $h_y = 0.01$.

C-2

1	0.350
2	0.375
3	0.400
4	0.425
5	0.450
6	0.475
7	0.500
8	0.525
9	0.550
10	0.575
11	0.600

Figure 16: Mach number contours and blade surface Mach number distributions for steady subsonic flow at $M_{-\infty} = 0.5$, and $\Omega_{-\infty} = 55$ deg through the NACA 5506 cascade.

1	-1.0
2	-0.8
3	-0.6
4	-0.4
5	-0.2
6	0.0
7	0.2
8	0.4
9	0.6
10	0.8
11	1.0

Figure 17: Contours of the in-phase component of the unsteady pressure due to the interaction of an acoustic excitation from upstream ($p_{I,-\infty} = (1,0)$, $\omega = 5$, $\sigma = -90$ deg) with the subsonic ($M_{-\infty} = 0.5$, $\Omega_{-\infty} = 55$ deg) NACA 5506 cascade: (a) LINFLO calculation; (b) LINFLUX calculation.
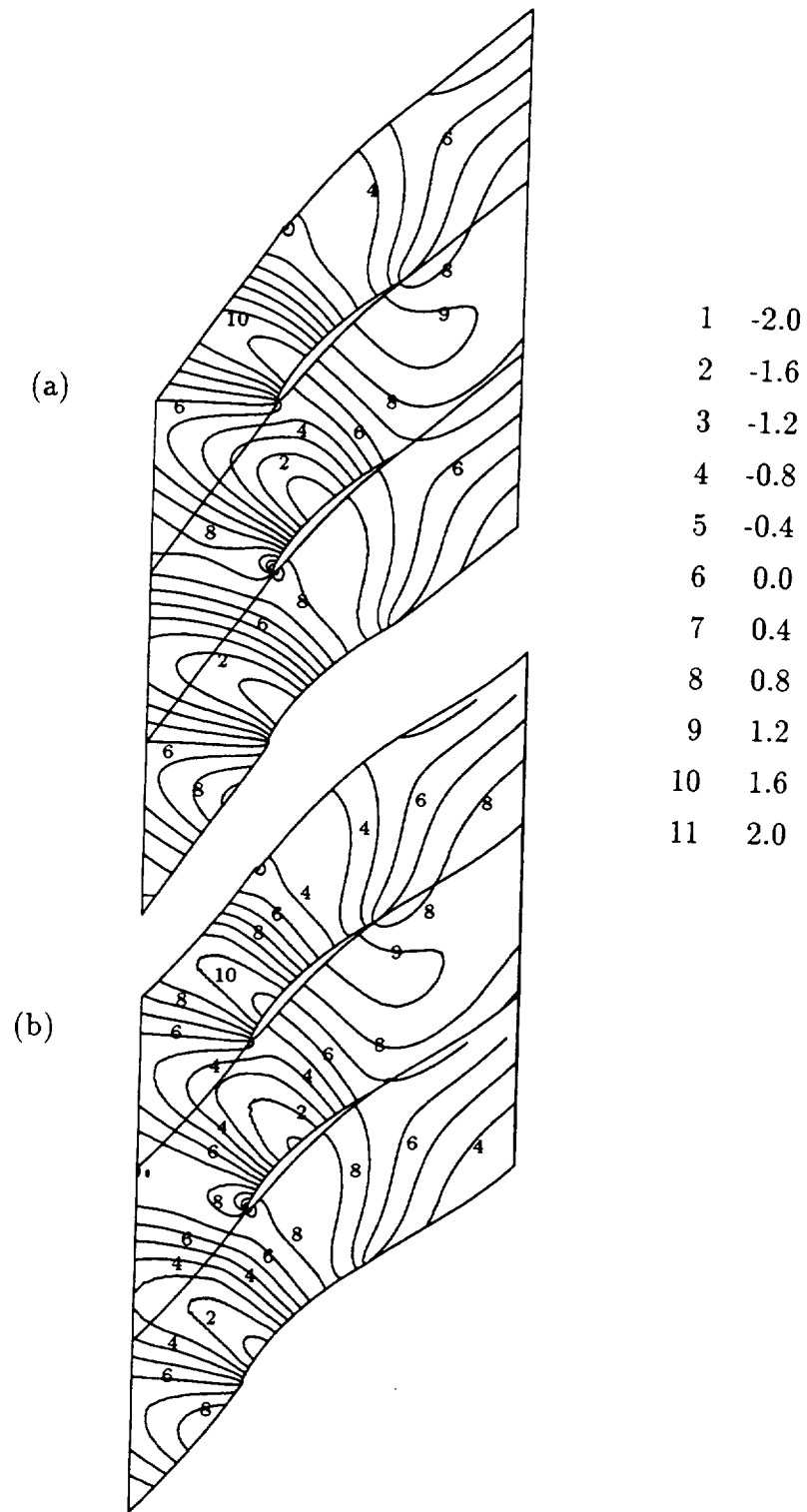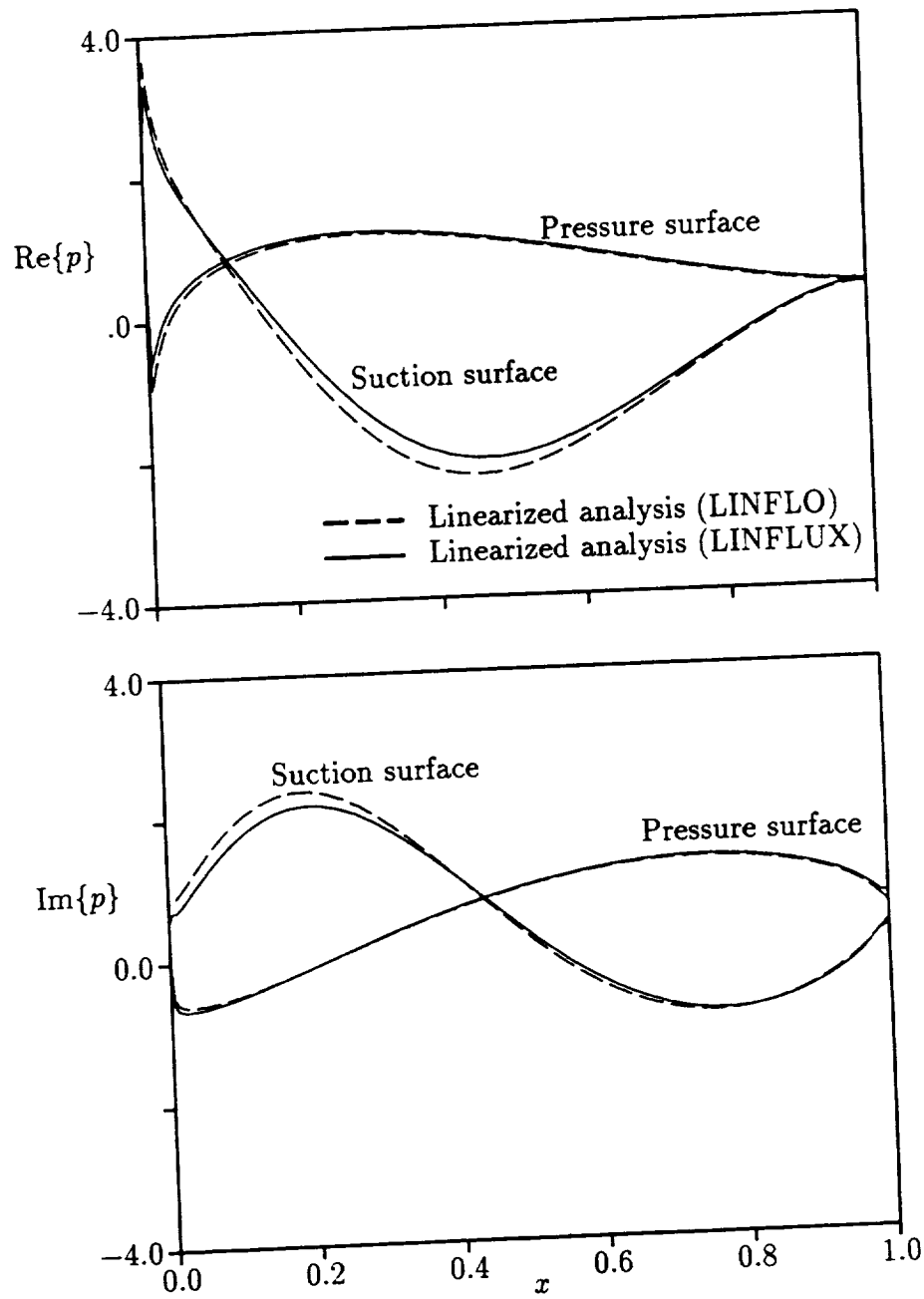
95

Figure 18: Unsteady surface pressure distributions due to the interaction of an acoustic excitation from upstream ($p_{I,-\infty} = (1,0)$, $\omega = 5$, $\sigma = -90$ deg) with the subsonic ($M_{-\infty} = 0.5$, $\Omega_{-\infty} = 55$ deg) NACA 5506 cascade.

(a)

(b)

1	-2.0
2	-1.6
3	-1.2
4	-0.8
5	-0.4
6	0.0
7	0.4
8	0.8
9	1.2
10	1.6
11	2.0

Figure 19: Contours of the in-phase component of the unsteady pressure due to the interaction of an acoustic excitation from downstream ($p_{I,+\infty} = (1,0)$, $\omega = 5$, $\sigma = -90$ deg) with the subsonic ($M_{-\infty} = 0.5$, $\Omega_{-\infty} = 55$ deg) NACA 5506 cascade: (a) LINFLO calculation; (b) LINFLUX calculation.
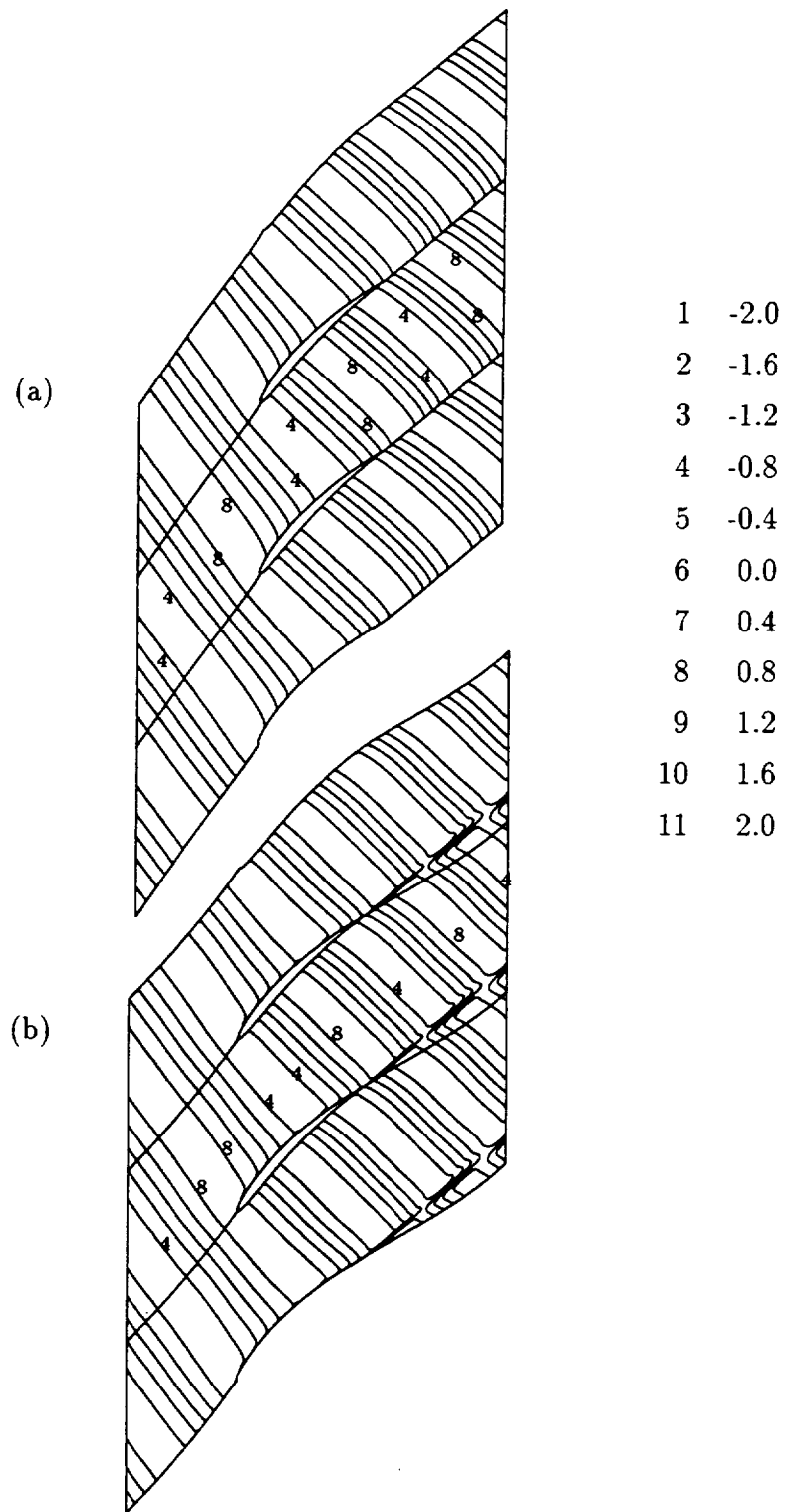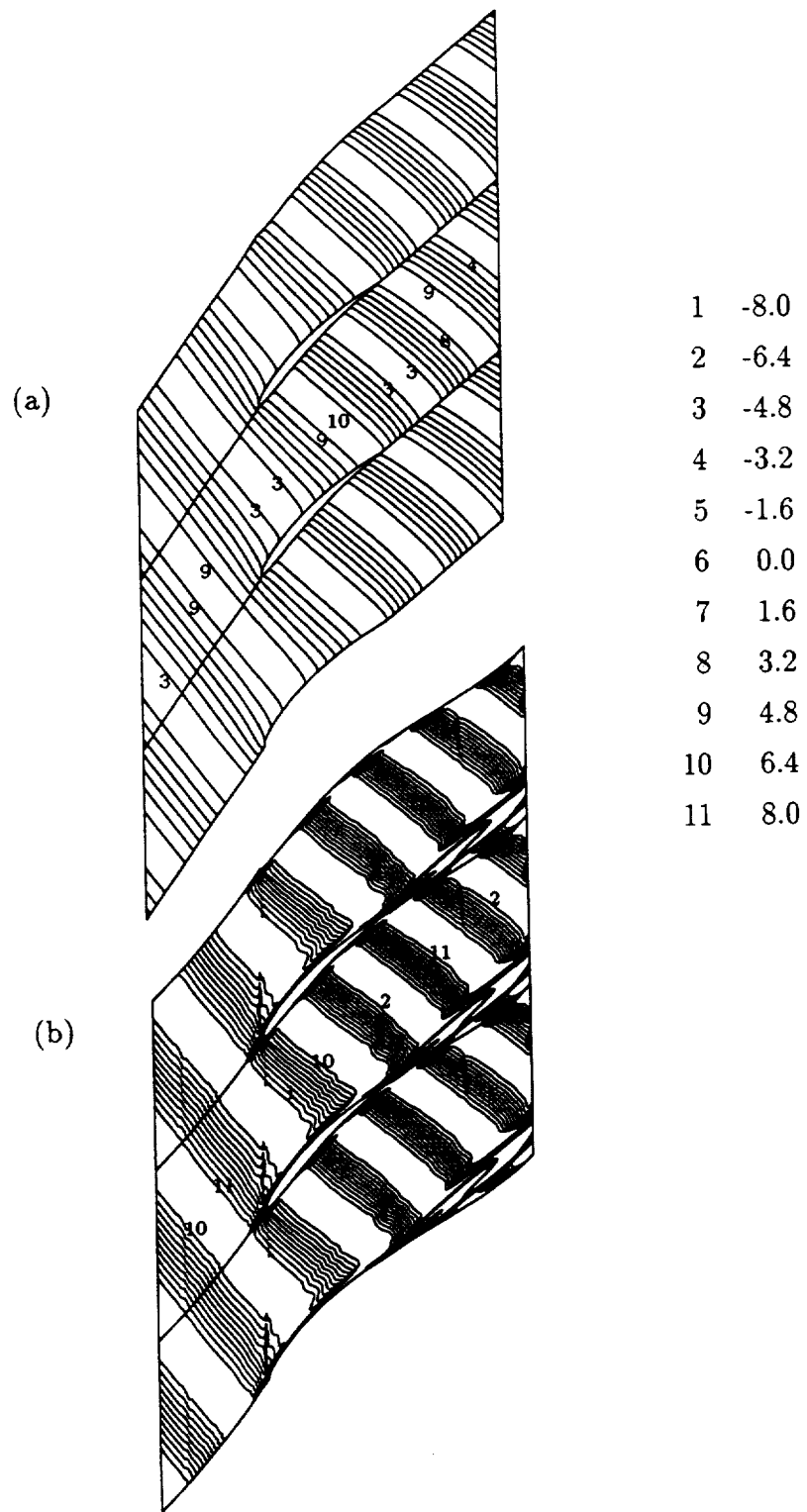
97

Figure 20: Unsteady surface pressure distributions due to the interaction of an acoustic excitation from downstream ($p_{I,+\infty} = (1,0)$, $\omega = 5$, $\sigma = -90$ deg) with the subsonic ($M_{-\infty} = 0.5$, $\Omega_{-\infty} = 55$ deg) NACA 5506 cascade.

1	-2.0
2	-1.6
3	-1.2
4	-0.8
5	-0.4
6	0.0
7	0.4
8	0.8
9	1.2
10	1.6
11	2.0

Figure 21: Contours of the in-phase component of the unsteady entropy for an entropic gust $(s_{-\infty} = (1,0)$, $\omega = 5$, $\sigma = -\pi)$ interacting with the subsonic $(M_{-\infty} = 0.5$, $\Omega_{-\infty} = 55$ deg) NACA 5506 cascade: (a) LINFLO calculation; (b) LINFLUX calculation.
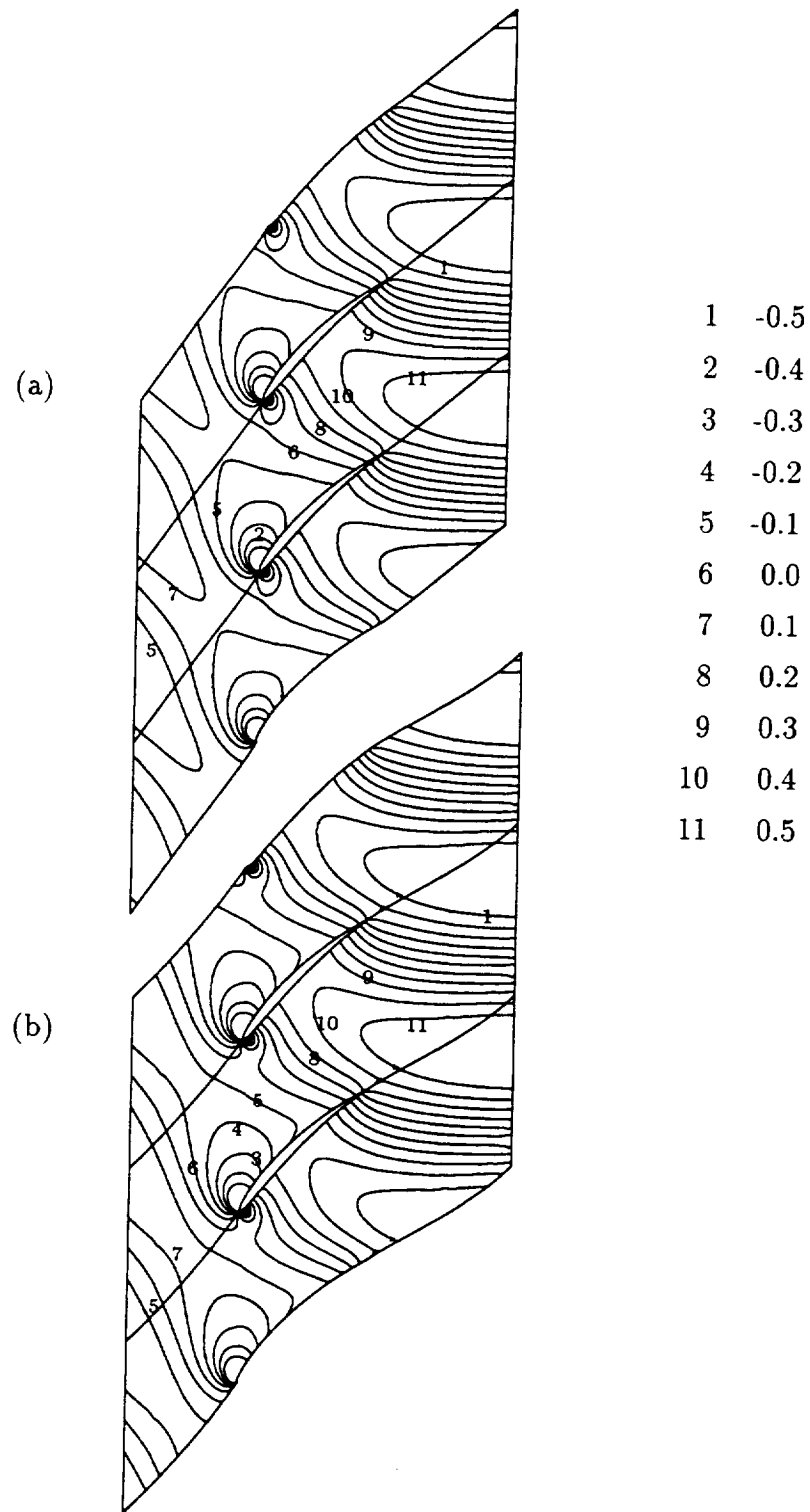
(a)

1	-8.0
2	-6.4
3	-4.8
4	-3.2
5	-1.6
6	0.0
7	1.6
8	3.2
9	4.8
10	6.4
11	8.0

(b)

Figure 22: Contours of the in-phase component of the unsteady vorticity for a vortical gust $(\mathbf{v}_{R,-\infty} \cdot \mathbf{e}_N = (1,0)$, $\omega = 5$, $\sigma = -\pi)$ interacting with the subsonic ($M_{-\infty} = 0.5$, $\Omega_{-\infty} = 55$ deg) NACA 5506 cascade: (a) LINFLO calculation; (b) LINFLUX calculation.
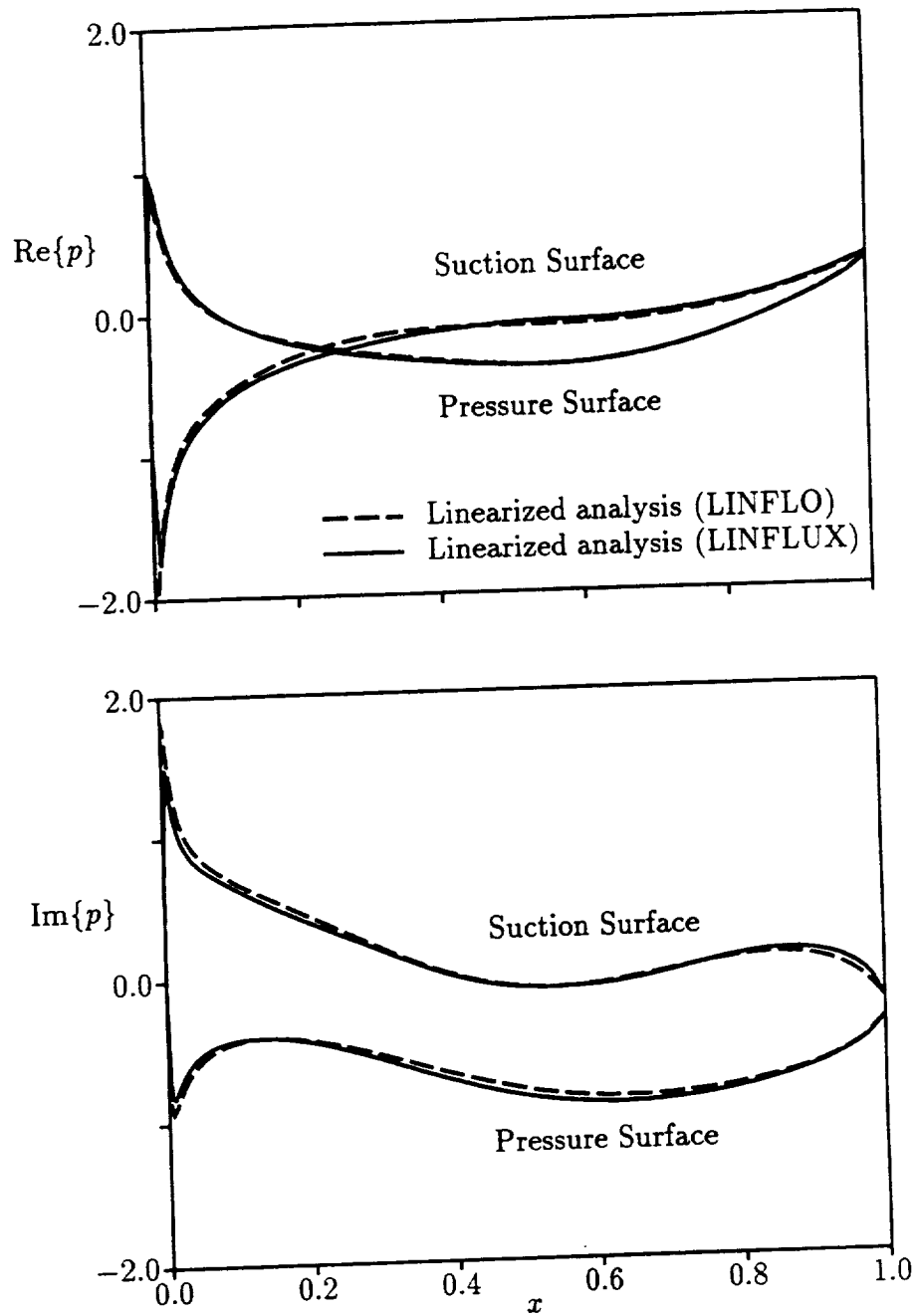
1	-0.5
2	-0.4
3	-0.3
4	-0.2
5	-0.1
6	0.0
7	0.1
8	0.2
9	0.3
10	0.4
11	0.5

Figure 23: Contours of the in-phase component of the unsteady pressure response for a vortical gust ($\mathbf{v}_{R,-\infty} \cdot \mathbf{e}_N = (1,0)$, $\omega = 5$, $\sigma = -\pi$) interacting with a subsonic ($M_{-\infty} = 0.5$, $\Omega_{-\infty} = 55$ deg) NACA 5506 cascade: (a) LINFLO calculation; (b) LINFLUX calculation.

Figure 24: Unsteady surface pressure distributions due to the interaction of a vortical gust $(\mathbf{v}_{R,-\infty} \cdot \mathbf{e}_N = (1,0),\ \omega = 5,\ \sigma = -\pi)$ and the subsonic $(M_{-\infty} = 0.5,\ \Omega_{-\infty} = 55$ deg) NACA 5506 cascade.

REPORT DOCUMENTATION PAGE

Form Approved
OMB No. 0704-0188

1. AGENCY USE ONLY (*Leave blank*)	2. REPORT DATE	3. REPORT TYPE AND DATES COVERED
	June 1995	Final Contractor Report

4. TITLE AND SUBTITLE

Development of a Linearized Unsteady Euler Analysis for Turbomachinery Blade Rows

5. FUNDING NUMBERS

WU–505–62–10
C–NAS3–25425

6. AUTHOR(S)

Joseph M. Verdon, Matthew D. Montgomery, and Kenneth A. Kousen

7. PERFORMING ORGANIZATION NAME(S) AND ADDRESS(ES)

United Technologies Research Center
411 Silver Lane
East Hartford, Connecticut 06108–1049

8. PERFORMING ORGANIZATION REPORT NUMBER

E–9575

9. SPONSORING/MONITORING AGENCY NAME(S) AND ADDRESS(ES)

National Aeronautics and Space Administration
Lewis Research Center
Cleveland, Ohio 44135–3191

10. SPONSORING/MONITORING AGENCY REPORT NUMBER

NASA CR–4677
R95–970293

11. SUPPLEMENTARY NOTES

12a. DISTRIBUTION/AVAILABILITY STATEMENT

Unclassified - Unlimited
Subject Category 02

This publication is available from the NASA Center for Aerospace Information, (301) 621–0390.

12b. DISTRIBUTION CODE

13. ABSTRACT (*Maximum 200 words*)

A linearized unsteady aerodynamic analysis for axial-flow turbomachinery blading is described in this report. The linearization is based on the Euler equations of fluid motion and is motivated by the need for an efficient aerodynamic analysis that can be used in predicting the aeroelastic and aeroacoustic responses of blade rows. The field equations and surface conditions required for inviscid, nonlinear and linearized, unsteady aerodynamic analyses of three-dimensional flow through a single, blade row operating within a cylindrical duct, are derived. An existing numerical algorithm for determining time-accurate solutions of the nonlinear unsteady flow problem is described, and a numerical model, based upon this nonlinear flow solver, is formulated for the first-harmonic linear unsteady problem. The linearized aerodynamic and numerical models have been implemented into a first-harmonic unsteady flow code, called LINFLUX. At present this code applies only to two-dimensional flows, but an extension to three-dimensions is planned as future work. The three-dimensional aerodynamic and numerical formulations are described in this report. Numerical results for two-dimensional unsteady cascade flows, excited by prescribed blade motions and prescribed aerodynamic disturbances at inlet and exit, are also provided to illustrate the present capabilities of the LINFLUX analysis.

14. SUBJECT TERMS

Axial flow turbomachinery blading; Three-dimensional flow; Euler equations; Nonlinear analysis; NPHASE; Unsteady perturbations; Linear analysis; LINFLUX; Blade vibration; Aerodynamic excitation; Aeroelastic and aeroacoustic responses

15. NUMBER OF PAGES

107

16. PRICE CODE

A06

17. SECURITY CLASSIFICATION OF REPORT	18. SECURITY CLASSIFICATION OF THIS PAGE	19. SECURITY CLASSIFICATION OF ABSTRACT	20. LIMITATION OF ABSTRACT
Unclassified	Unclassified	Unclassified	